New observational constraints on the temperature dependence of O_3 production and loss

Laura E. R. Barry
Anchorage, Alaska

B.A., Pomona College, 2014

A Dissertation presented to the Graduate Faculty of the University of Virginia in Candidacy for the Degree of Doctor of Philosophy

Department of Environmental Sciences

University of Virginia
April, 2023

Committee Members:
Dr. Sally E. Pusede (advisor)
Dr. Manuel T. Lerdau
Dr. Todd M. Scanlon
Dr. Xi Yang
Dr. John V. Pepper

Abstract

Ozone (O_3) air pollution is sensitive to climate change. O_3 is a secondary pollutant, and its abundance and impacts are controlled by production and loss processes, both of which vary with temperature. Controls on O_3 precursors, especially nitrogen oxides ($NO_x \equiv NO + NO_2$), are potentially an effective O_3-related climate adaptation strategy when and where O_3 variability is driven by O_3 production (PO_3) chemistry. In locations where O_3 loss (LO_3) controls O_3 concentrations, the response of O_3 dry deposition to climate change will determine future O_3 concentrations. In this dissertation, I provide new insight into the temperature dependence of PO_3 and LO_3 and discuss the implications of these relationships for O_3 variability in a changing climate. In Chapter 2, I present O_3-temperature relationships in 1999–2001 and 2017–2019 on weekdays and weekends in climate regions and cities across the contiguous U.S. and explore their trends with NO_2. In Chapter 3, I present eddy covariance measurements of O_3 flux (F_{O3}) and deposition (v_d) velocity in a Central Virginia forest. In Chapter 4, I present stomatal and nonstomatal O_3 deposition velocity relationships with temperature. I show that since 1999–2001, O_3 climate penalties ($m_{O3\text{-}T}$), defined as the slope of the O_3-temperature correlation, decreased and weakened in most, but not all, climate regions (by 0.4–1.2 ppb $^oC^{-1}$ when decreases occurred) and in many urban areas (by 0.2–2.1 ppb $^oC^{-1}$ when decreases occurred). I demonstrate that when $m_{O3\text{-}T}$ are driven by PO_3, they are responsive to NO_x emissions reductions under higher NO_2 conditions than O_3 mixing ratios. Additional NO_x controls will further lower $m_{O3\text{-}T}$ in many major cities with O_3 nonattainment designations, even where PO_3 chemistry continues to be NO_x suppressed. I discuss the instrumentation, calibrations, and spectral and uncertainty analyses required to measure F_{O3} and O_3 v_d on a forest research tower. I measure the highest O_3 mixing ratios in Central Virginia in the spring and the highest O_3 v_d in the summer, with half-hourly O_3 v_d frequently ranging from 1–

1.5 cm s^{-1}. I show that inverse relationships between daytime stomatal conductance and temperature on hot days (≥32ºC) suppress O_3 v_d and increases the O_3 mixing ratios and that on warm nights (≥24ºC), an increase LO_3 to within-canopy chemistry lowers O_3 mixing ratios, offsetting daytime increases. This work can inform O_3 pollution reduction and climate adaptation strategies in polluted urban areas and provides a modeling constraint for LO_3 in the Southeast U.S.

Table of Contents

List of tables **7**

List of figures **8**

Acknowledgements **12**

CHAPTER 1: INTRODUCTION **14**

1.1 O_3 production (PO_3) 15

1.2 O_3 loss (LO_3) 17

1.2.1 Stomatal O_3 loss 18

1.2.2 Nonstomatal O_3 loss 22

1.3 Dissertation contents 25

References 28

CHAPTER 2: ON THE OBSERVED NO_2 DEPENDENCE OF THE OZONE CLIMATE PENALTY ACROSS THE CONTIGUOUS UNITED STATES **40**

2.1 Introduction 40

2.2 Methods 42

2.3 Results and Discussion 45

2.3.1 Trends in $m_{O3\text{-}T}$, $r_{O3\text{-}T}$, and MDA8 O_3 across Variability in NO_2 45

2.3.2 The NO_2 Dependence of $m_{O3\text{-}T}$ and MDA8 O_3 50

2.3.3 Continued O_3 Climate Adaptation through NO_x Control in Cities 58

2.4 Summary and Implications 62

2.5 Appendix 64

References 70

CHAPTER 3: MEASURING OZONE FLUX AND DEPOSITION VELOCITIES IN A CENTRAL VIRGINIA FOREST **79**

3.1 Introduction 79

3.2 Methods 85

3.2.1 Virginia Forest Laboratory, Pace Tower 85

3.2.2 Instrumentation 86

3.2.2.1 Eddy covariance F_{O3} 86

3.2.2.2 O_3 mixing ratio observations 89

3.2.2.3 Three-dimensional winds 90

3.2.2.4 Water vapor 90

3.2.3 Data Processing 90

3.2.3.1 O_3 mixing ratio 90

3.2.3.2 Eddy covariance F_{O3} and O_3 v_d 92

3.2.3.3 Cospectral analysis and systematic errors 94

3.3 Results and Discussion 100

3.3.1 Eddy covariance random errors 100

3.3.2 O_3 mixing ratios 102
3.3.3 F_{O3} and O_3 v_d measurements 105
3.4 Conclusions 107
References 109
CHAPTER 4: ON THE TEMPERATURE DEPENDENCE OF OZONE DRY DEPOSITION IN A CENTRAL VIRGINIA FOREST 117
4.1 Introduction 117
4.2 Methods 120
4.2.1 Instrumentation 120
4.2.1.1 Ozone 120
4.2.1.2 Water flux 121
4.2.1.3 Air temperature and relative humidity 122
4.2.1.4 Solar-induced fluorescence (SIF) 122
4.2.1.5 Biogenic volatile organic compounds (BVOCs) 123
4.2.2 Stomatal and nonstomatal O_3 v_d 123
4.3 Results and Discussion 127
4.3.1 Impact of LO_3 on O_3 variability 129
4.3.2 Daytime O_3 v_d- and g_{O3}-temperature and SIF relationships 130
4.3.3 Nighttime O_3 v_d-, nonstomatal conductance (g_{ns}), and O_3-temperature relationships 133
4.3.4 LO_3 and rising temperatures 136
4.4 Conclusions 137
References 139
CHAPTER 5: SUMMARY 148
References 152

List of tables

Table 2.1. O_3-season mean $m_{O3\text{-}T}$ (ppb °C^{-1}) with mean slope errors, $r_{O3\text{-}T}$, and MDA8 O_3 (ppb) at *N* monitoring stations with measurements in both 1999–2001 and 2017–2019 in nine climate regions and 32 MSAs. Variability as 1 standard deviation is represented parenthetically. Statistical significance for differences in 1999–2001 and 2017–2019 is based on the Wilcoxon signed-rank test (regions; $p < 0.01$) and 1999–2001 and 2017–2019 mean errors added in quadrature (MSAs) and indicated as * in 2017–2019…….49

Table 2.S1. O_3-season percent difference in weekday–weekend NO_2 TVCD (%) and normalized mean average and mean maximum weekday–weekend decrease in $m_{O3\text{-}T}$ (ppb °C^{-1} per unit 10^{15} molecules NO_2 cm^{-2}) in 19 MSAs. Variability as 1 standard deviation is represented parenthetically……...…….69

Table 4.1. Seasonal mean O_3 v_d (cm s^{-1}) and g_{O3} (cm s^{-1}) daytime (10 am–3 pm) and nighttime (11 pm–5 am). Variability as 1 standard deviation is represented parenthetically……129

List of figures

Figure 2.1. NOAA U.S. climate regions across the contiguous U.S.: Northeast (yellow), Southeast (blue), Ohio Valley (lilac), South (green), Upper Midwest (gray), Northern Rockies and Plains (pale orange), Southwest (peach), West (cyan), and Northwest (light red). MSAs are labeled numerically, corresponding to Table 2.1. ……..……....44

Figure 2.2. Mean O_3-season (May–September) $m_{O3\text{-}T}$ (top), MDA8 O_3 (middle), and $r_{O3\text{-}T}$ (bottom) at each O_3 monitoring station with measurements in both 1999–2001 (dark green, orange, and blue, respectively) and 2017–2017 (light green, gold, and cyan, respectively) in the nine NOAA climate regions: Northeast (a), Southeast (b), Ohio Valley (c), South (d), Upper Midwest (e), Northern Rockies and Plains (f), Southwest (g), West (h), and Northwest (i)……48

Figure 2.3. Differences between PO_3 curves as function of NO_x at five VOC reactivity levels (a). PO_3 as a function of NO_x under five VOC reactivity levels that increase exponentially: lowest (black), low (blue), intermediate (light blue), high (green), and highest (yellow-green). For example, the green curve in panel a is the difference between the green and light blue PO_3 curves in panel b. Circles are the peak change in PO_3 and PO_3, with the difference based on the increase in PO_3 from the lower VOC level (same color circle)…….52

Figure 2.4. Weekday (circles) and weekend (diamonds) $m_{O3\text{-}T}$ (ppb $^oC^{-1}$) (top) and MDA8 O_3 (ppb) (bottom) versus NO_2 TVCDs (molecules cm^{-2}) colored by $r_{O3\text{-}T}$ and 8-h average daily temperature, respectively, in nine NOAA climate regions: Northeast (a), Southeast (b), Ohio Valley (c), South (d), Upper Midwest (e), Northern Rockies and Plains (f), Southwest (g), West (h), and Northwest (i). Weekday observations are binned every 0.3 x 10^{15} molecules cm^{-2} NO_2 and tethered to their corresponding means on weekends. Data in 1999–2001 are outlined in black and data in 2017–2019 are outlined in green. To support visualization only, NO_2 TVCDs in 1999–2001 are estimated by scaling 2018–2019 NO_2 TVCDs according to surface NO_2* mixing ratios in both periods……..…….55

Figure 2.5. Weekday (circles) and weekend (diamonds) $m_{O3\text{-}T}$ (ppb $^oC^{-1}$) (top) and MDA8 O_3 (ppb) (bottom) versus NO_2 TVCD (molecules cm^{-2}), where NO_2 is lower on weekends than weekdays by at least 0.1 x 10^{15} molecules cm^{-2}, colored by $r_{O3\text{-}T}$ and 8-h average daily temperature, respectively, in six MSAs: New York-Newark (a), Philadelphia-Camden-Wilmington (b), Washington-Arlington-Alexandria (c), Atlanta (d), Houston-The Woodlands-Sugar Land (e), Detroit-Warren-Dearborn (f), Los Angeles-Long Beach-Anaheim and Riverside-San Bernadino-Ontario (g), Phoenix-Mesa-Scottsdale (h), and Denver-Aurora-Lakewood (i). Weekday observations are binned every 0.3 x 10^{15} molecules cm^{-2} NO_2 and tethered to the corresponding mean values on weekends. Data in 1999–2001 are outlined in black and data in 2017–2019 are outlined in green. To support visualization only, NO_2 TVCDs in 1999–2001 are estimated by scaling 2018–2019 NO_2 TVCDs according to surface NO_2* mixing ratios in both periods……61

Figure 2.S1. $m_{O3\text{-}T}$ (ppb $^oC^{-1}$) versus $r_{O3\text{-}T}$ (top row) and MDA8 O_3 (ppb) (bottom row) in 1999–2001 (black outline) and 2017–2019 (green outline) in the nine climate regions (panels a, d, g, and j), 32 MSAs (panels b, e, h, and k), and at all O_3 monitors in the contiguous U.S. (panels c, f, i,

and l). Lines of best fit (dashed), Pearson correlation coefficients (*r*), and fit *p*-values are shown. ……65

Figure 2.S2. Correlations between changes in $m_{O3\text{-}T}$ (ppb ºC^{-1}) versus changes in $r_{O3\text{-}T}$ and changes in MDA8 O_3 (ppb) between 1999–2001 and 2017–2019 in the nine climate regions (panels a and d), 32 MSAs (panels b and e), and at all O_3 monitors in the contiguous U.S. (panels c and f)……..66

Figure 2.S3. Weekday (circles) and weekend (diamonds) $m_{O3\text{-}T}$ (ppb ºC^{-1}) (top) and MDA8 O_3 (ppb) (bottom) versus NO_2 TVCDs (molecules cm^{-2}) colored by $r_{O3\text{-}T}$ and 8-h average daily temperature, respectively, in the West excluding the Los Angeles and Riverside MSAs. Weekday observations are binned every 0.3 x 10^{15} molecules cm^{-2} NO_2 and tethered to the corresponding means on weekends. Data in 1999–2001 are outlined in black and data in 2017–2019 are outlined in green. To support the visualization only, NO_2 TCVDs in 1999–2001 are estimated by scaling 2018–2019 NO_2 TVCDs according to surface NO_2* mixing ratios in both periods as described in the Methods……67

Figure 2.S4. Weekday (circles) and weekend (diamonds) $m_{O3\text{-}T}$ (ppb ºC^{-1}) (top) and MDA8 O_3 (ppb) (bottom) versus NO_2 TVCD (molecules cm^{-2}), where NO_2 is lower on weekends than weekdays by at least 0.1 x 10^{15} molecules cm^{-2}, colored by $r_{O3\text{-}T}$ and 8-h average daily temperature, respectively, in 10 MSAs: Baltimore-Columbia-Towson (a), Dallas-Fort Worth-Arlington (b), Chicago-Naperville-Elgin (c), Cincinnati (d), Louisville-Jefferson County (e), Bakersfield (f), Sacramento-Roseville-Arden-Arcade (g), San Francisco-Oakland-Hayward (h), San Diego-Carlsbad (i), and Las Vegas (j). Weekday observations are binned every 0.3 x 10^{15} molecules cm^{-2} NO_2 and tethered to the corresponding means on weekends. Data in 1999–2001 are outlined in black and data in 2017–2019 are outlined in green. To support visualization only, NO_2 TCVDs in 1999–2001 are estimated by scaling 2018–2019 NO_2 TVCDs according to surface NO_2* mixing ratios in both periods……..……...68

Figure 3.1. Schematic of O_3 flux and gradient inlets and instrumentation. Arrows indicate the direction of the flow. All instrumentation is inside the on-site laboratory (not shown)……86

Figure 3.2. Modified LOZ-3F O_3 flux instrument with the supply reservoir, main reservoir, HSD, and air inlet labeled……...……...……...…87

Figure 3.3. 3D sonic anemometer and O_3 flux inlet (a) and 30 m O_3 gradient inlet (b)……..…89

Figure 3.4. Sample lag time from 8 August 2020 at 2:30 pm LT for *w* with O_3 (blue solid line) and T_s (red dashed line). The maximum covariance of *w*'O_3' occurs at a –7.6 s lag. The maximum covariance of *w*'T_s' occurs at a lag of 0 s……...……..…94

Figure 3.5. Average ogive for half-hour measurement periods from 1–3:30 pm LT June–August 2020 for *w*'O_3' (blue solid line) and *w*'T_s' (red dashed line). Cospectra are averaged into 100 equally spaced bins across the logarithmic frequency axis..……...……...96

Figure 3.6. Averaged cospectral density function for *w*'O_3' (blue solid line) and *w*'T_s' (red dashed line) from 1–3:30 pm LT June–August 2020 when conditions are unstable. Cospectra are averaged

into 100 equally spaced bins across the logarithmic frequency axis. The –4/3 line (black dashed line) represents the expected slope for the inertial subrange……..……..97

Figure 3.7. Averaged frequency weighted normalized cospectra for w'O_3' (blue solid line) and w'T_s' (red dashed line). Averaged across 1–3:30 pm LT June–August 2020 when conditions are unstable. Cospectra are averaged into 100 equally spaced bins across the logarithmic frequency axis……..……...……98

Figure 3.8. July 2019–July 2021 hourly mean 40-m O_3 mixing ratios (ppb)……102

Figure 3.9. Seasonal diurnal 40 m O_3 mixing ratios at the Virginia Forest Laboratory from July 2019–July 2021 for (a) winter, (b) spring, (c) summer, and (d) fall. Shading represents one standard deviation and error bars represent standard error of the mean…….……...…….103

Figure 3.10. Seasonal vertical O_3 gradients (ppb) at the Virginia Forest Laboratory from July 2019–July 2021 for winter (a), spring (b), summer (c), and fall (d). Dashed lines with diamonds morning gradients (8–11 am LT averages), solid lines with squares are mid-day gradients (12–4 pm LT averages), dash-dotted lines with circles are evening gradients (5–11 pm LT averages), and dotted lines with triangles are overnight (12–7 am LT averages)……104

Figure 3.11. July 2019 – July 2021 F_{O3} (ppb m s^{-1}) (black) and O_3 v_d (cm s^{-1}) (blue)…….105

Figure 3.12. Monthly diurnal F_{O3} (ppb m s^{-1}) (black with purple shading) and O_3 v_d (cm s^{-1}) (blue with light blue shading) at the Pace tower from July 2019–July 2021. Shading represents one standard deviation and error bars represent standard error of the mean……106

Figure 4.1. Daytime (purple circles) and nighttime (yellow diamonds) monthly average O_3 v_d (cm s^{-1}). Daytime is defined as 10 am–3 pm LT and nighttime is defined as 11 pm–5 am LT. Error bars represent standard error of the mean…….……..…….128

Figure 4.2. Seasonal diurnal pattern of O_3 v_d (cm s^{-1}) (solid lines) and g_{O3} (cm s^{-1}) (dashed lines) in the winter (a), spring (b), summer (c), and fall (d)……...…….129

Figure 4.3. Correlations between daytime average (10 am–3 pm LT) O_3 v_d (cm s^{-1}) (a–c), g_{O3} (cm s^{-1}) (d–f), and O_3 mixing ratio (ppb) (g–i) with temperature (ºC) (a, d, g), vapor pressure deficit (Pa) (b, e, h), and SIF (W m^{-2} sr^{-2} μm^{-1}) (c, f, i) in the spring (purple circles), summer (green squares), and fall (orange triangles). Dashed lines are lines of best fit. Seasonal Pearson correlation coefficients (r) are indicated on each panel. Significant correlations (p-value < 0.05) are indicated with an *…….……..131

Figure 4.4. May–September daytime (10 am–3 pm LT) O_3 v_d (cm s^{-1}) (green, solid line) and O_3 mixing ratio (ppb) (blue, dashed line) binned by temperature (ºC). Error bars represent standard error of the mean……...…132

Figure 4.5. May–September diurnal patterns of g_{ns} (cm s^{-1}) (black squares, solid line) and the O_3 reactivity to α-pinene (s^{-1}) (pink circles, dashed line). Error bars represent standard error of the mean……..…….……..135

Figure 4.6. May–September nighttime average (11 pm–5 am LT) temperature (ºC) dependence of g_{ns} (cm s^{-1}) (black squares) and α-pinene O_3 reactivity (s^{-1}) (pink circles) (a) and O_3 (ppb) (b)……...……...…135

Figure 4.7. June–September O_3 (ppb) diurnal pattern on high temperature days (10 am–3 pm LT mean temperature ≥32ºC). Low temperature nights (11 pm–5 am LT mean temperature <24ºC) are shown in blue and high temperature nights (11 pm–5 am LT mean temperature ≥24ºC) are shown in red. Error bars represent standard error of the mean…….…….137

Acknowledgements

First, I would like to thank Sally Pusede, without her mentorship and guidance this dissertation would not have been possible. Second, to my committee members, Manuel Lerdau, Todd Scanlon, Xi Yang, and John Pepper, thank you for your insight and contributions to this dissertation.

Thank you to those who assisted me in the field. This work would not have been possible without Madeline Miles, Andrew Davies, Angelique Demetillo, and Chris So, who spent many days at the tower with me.

Thank you to my collaborators. Solar-induced fluorescence data were provided by Xi Yang, Rong Li, and Koong Yi. Water vapor fluxes were provided by Todd Scanlon and Elizabeth Tatham. Biogenic volatile organic compound data were provided by Gabriel Isaacman-VanWertz and Deborah McGlynn of Virginia Tech.

And finally, thank you to the wonderful friends I've made in the Environmental Sciences department and my family. Your friendship, love, and support has been invaluable to me.

This research was funded by an NSF Division of Atmospheric and Geospace Sciences grant (NSF AGS 1837891). I received additional support from the Virginia Space Grant Consortium Graduate Research Awards Program. MDA8 O_3 and NO_2* mixing ratios are provided by the U.S. EPA Air Quality System (epa.gov/outdoor-air-quality-data), temperature measurements are from the Automated Surface Observing System and Automated Weather Observing System via Iowa State University Iowa Environmental Mesonet (mesonet.agron.iastate.edu/ASOS), and TROPOMI NO_2 and HCHO TVCDs and MODIS LAI can be downloaded at search.earthdata.nasa.gov. The 2018

Core Based Statistical Areas are provided by the U.S. Census Bureau (census.gov/geographies/mapping-files/time-series/geo/carto-boundary-file.html)

CHAPTER 1: INTRODUCTION

Ozone (O_3) in the troposphere is a detrimental trace gas to humans and vegetation. Exposure to O_3 pollution is associated with chronic respiratory diseases and increased risk of mortality in humans (Jerrett et al., 2009; Zhang et al., 2019). O_3 exposure limits plant productivity and can reduce crop yield (Ashmore, 2005; Ainsworth et al., 2012; Lombardozzi et al., 2013; Reich, 1987). O_3 is a secondary air pollutant, as it is not directly emitted; instead, it is created by photochemical reactions. Its lifetime in the troposphere ranges from hours to weeks based on whether it is in the surface boundary layer or free troposphere (Szopa, 2021). As a secondary pollutant, the amount of O_3 is a function of O_3 production (PO_3) and, therefore, the absolute and relative abundance of its precursors, O_3 loss (LO_3) to deposition and chemistry, and atmospheric mixing and transport.

O_3 contributes to climate change directly as a greenhouse gas, indirectly as an oxidant leading to the production of light-scattering secondary organic aerosol, and indirectly by damaging vegetation and reducing the carbon sink (Sitch et al., 2007; Szopa, 2021; von Schneidemesser et al., 2015). At the same time, higher temperatures typically increase O_3 (Jacob and Winner, 2009; Pusede et al., 2015), and climate change-driven O_3 increases will worsen adverse outcomes, both for human and environmental health (Jay et al., 2018). Open questions remain in how PO_3, LO_3, and O_3 transport will respond to climate change-driven increasing temperatures and how to mitigate these outcomes. In this dissertation, I improve our understanding of (1) how the temperature dependence of O_3 (the O_3 climate penalty) has changed across the contiguous U.S. over the past 20 years and its dependence on the O_3 precursor nitrogen dioxide (NO_2) and (2) how temperatures impact LO_3 in a Southeastern U.S. forest.

1.1 O_3 production (PO_3)

The O_3 precursors, nitrogen oxides ($NO_x \equiv NO + NO_2$) and volatile organic compounds (VOCs), are emitted biogenically and anthropogenically. PO_3 is driven by radical cycling of NO_x and HO_x ($HO_x \equiv OH + HO_2 + RO_2$). PO_3 varies nonlinearly with NO_x and VOCs. When NO_x is low, PO_3 and NO_x are positively correlated (chemistry is *NO_x-limited*), while when NO_x is high, PO_3 and NO_x are inversely correlated (chemistry is *NO_x-suppressed*). Increasing the abundance of VOCs reactive with the hydroxyl radical (OH) shifts the transition point between NO_x-limited and NO_x-suppressed regimes to higher NO_x. Understanding the local PO_3 regime is important for predicting future O_3 concentrations and developing pollution control strategies, particularly in urban areas with high precursor emissions.

PO_3 has a well-established temperature dependence due to temperature dependent precursors, with rising temperatures predicted increase O_3 pollution (Fiore et al., 2012; Jacob and Winner, 2009; Pusede et al., 2015; Sillman and Samson, 1995). While detailed in the Pusede et al. (2015) review, in brief, PO_3 is dependent on organic reactivity, HO_x, NO_x, peroxy nitrates, and alkyl nitrates, each of which vary with temperature. The temperature dependence of organic reactivity is caused by temperature-driven emissions of organic compounds and faster bimolecular reaction rates at higher temperatures (Guenther et al., 1993). Similar to O_3, temperature-dependent HO_x production depends on temperature-dependent precursors and photolysis rates, the latter co-varying with, but not driven by higher temperatures. Temperature-driven HO_x production increases PO_3 (Perdigones et al., 2022; Romer et al., 2018). While not inherently temperature dependent, anthropogenic NO_x emissions may increase under high temperature conditions from an increased demand for energy in the Eastern U.S. (He et al., 2013). Soil NO_x emissions are strongly temperature dependent and

have the ability to increase $P\mathrm{O_3}$ (Romer et al., 2018). Peroxy nitrates ($\mathrm{RO_2NO_2}$) act as a temperature-dependent reservoir for $\mathrm{NO_2}$ and $\mathrm{RO_2}$. Peroxy nitrates can transport $\mathrm{NO_x}$ downwind of sources before thermally decomposing. Acting as a $\mathrm{NO_x}$ source, the $\mathrm{NO_2}$ goes on to contribute to $P\mathrm{O_3}$ where chemistry is $\mathrm{NO_x}$-limited downwind of cities (Sillman and Samson, 1995; Steiner et al., 2010). The formation of alkyl nitrates reduces $P\mathrm{O_3}$, and individual alkyl nitrate formation is inversely correlated with temperature; however, the sum of alkyl nitrates may increase or decrease with temperature, depending on the organic mixture (Lee et al., 2014; Pusede et al., 2015).

The $\mathrm{O_3}$-temperature sensitivity is frequently referred to as the $\mathrm{O_3}$ climate penalty, a term coined by Wu et al. (2008). Most frequently, the climate penalty is defined as the slope of the $\mathrm{O_3}$-temperature correlation, thus measuring the change in $\mathrm{O_3}$ mixing ratio for every degree change in temperature (Bloomer et al., 2009). Conceptually, the climate penalty is thought of as the additional reduction in precursor emissions necessary to counteract predicted warming (Bloomer et al., 2009; Fiore et al., 2015; Pusede et al., 2015; Rasmussen et al., 2013; Wu et al., 2008). Across the contiguous U.S., climate penalties in the past two decades have ranged from 0–8 ppb $^{\circ}\mathrm{C}^{-1}$, though $\mathrm{NO_x}$ emissions reductions have led to declines (Avise et al., 2012; Bloomer et al., 2009; Brown-Steiner et al., 2015; Ninneman and Jaffe, 2021; Nolte et al., 2021; Pusede et al., 2015; Rasmussen et al., 2012; Rasmussen et al., 2013; Steiner et al., 2006; Steiner et al., 2010; Zhao et al., 2013). The effectiveness of precursor reductions depends on chemical production conditions and the contribution of $P\mathrm{O_3}$ to the local $\mathrm{O_3}$ mass balance. Under low $\mathrm{NO_x}$ conditions ($\mathrm{NO_x}$-limited $P\mathrm{O_3}$ chemistry), $P\mathrm{O_3}$ is sensitive to increases in $\mathrm{NO_x}$ while under high $\mathrm{NO_x}$ conditions ($\mathrm{NO_x}$-suppressed $P\mathrm{O_3}$ chemistry), $P\mathrm{O_3}$ responds proportionally to changes in VOCs and $\mathrm{HO_x}$ radical production. Due to the differences in the temperature-sensitivity of the reactant source terms, $\mathrm{NO_x}$-suppressed $P\mathrm{O_3}$ chemistry typically elicits a stronger temperature-dependent response than $\mathrm{NO_x}$-

limited PO_3 chemistry (Bloomer et al., 2009; Ito et al., 2009; Nussbaumer and Cohen, 2020; Pusede and Cohen, 2012; Pusede et al., 2014; Pusede et al., 2015; Rasmussen et al., 2012; Rasmussen et al., 2013). Warming temperatures due to climate change have the potential to increase O_3 pollution, particularly in places where O_3 variability is driven by PO_3. Jacob and Winner (2009) predict O_3 increases of 1–10 ppb, with the largest increases in the most polluted areas. Precursor emissions reductions, particularly in locations with high NO_x pollution, may limit increases in temperature dependent PO_3 (Coates et al., 2016; Li, 2018; Rieder et al., 2018).

1.2 O_3 loss (LO_3)

O_3 is removed from the surface boundary layer in a variety of ways, but a dominant loss process is dry deposition (Ainsworth et al., 2012; Fowler et al., 2009). In regions where LO_3 is important to the local O_3 mass balance, LO_3 can control significant variability in O_3 concentrations (Garland and Derwent, 1979; Kavassalis and Murphy, 2017; Monks et al., 2015). Changes to dry deposition can be as important to surface O_3 concentrations as changes in precursor emission (Andersson and Engardt, 2010; Baublitz et al., 2020). Dry deposition is split into a stomatal pathway and a nonstomatal pathway. Along the stomatal pathway, plants open their stomata to take in carbon dioxide (CO_2) to photosynthesize. They balance their stomatal aperture to maximize carbon uptake while limiting water loss (Ball et al., 1987). Here, atmospheric O_3 also enters the stomata and goes on to damage plant cellular components (Fiscus et al., 2005). The nonstomatal pathway is used to describe all uptake methods that do not occur via the stomata. These include uptake onto leaf cuticles, soil, snow, water, and built surfaces, as well as chemical destruction occurring below the level of a sensor inlet, especially when researchers are focused on O_3 flux measurements (Clifton

et al., 2020). Both stomatal and nonstomatal deposition vary with environmental factors (Fowler et al., 2009; Monks et al., 2015). Temperature, increasing due to climate change, may alter stomatal deposition, nonstomatal deposition, or both, the extent to which will be locally specific.

1.2.1 Stomatal O_3 loss

Stomatal O_3 uptake is controlled by stomatal conductance (g_s). Jarvis (1976) first developed a leaf stomatal resistance model ($r_s = g_s^{-1}$) dependent on light intensity, CO_2 concentration, vapor pressure deficit (VPD), temperature, and leaf water potential. Changes to g_s lead to changes in stomatal LO_3. With regard to temperature, Jarvis (1976) proposed an increase in g_s until an optimal leaf temperature was reached. Above this temperature, g_s decreases. However, Urban et al. (2017) found a continual increase in g_s with temperature as long as VPD conditions were maintained. Under high VPD conditions, stomatal conductance and stomatal aperture are reduced to minimize water loss (Grossiord et al., 2020; Jarvis, 1976). Relationships of temperature and VPD with g_s are typically entangled (Buckley and Mott, 2013; Grossiord et al., 2020), as high temperature and high VPD frequently co-occur, and it is difficult to isolate their individual effects on O_3 deposition (Tuovinen et al., 2009).

Stomatal deposition is a dominant dry deposition pathway, particularly in forested environments (Clifton et al., 2020), yet direct stomatal deposition-temperature relationships are infrequently reported and vary from location to location. In places where O_3 concentrations are strongly temperature dependent, it can be difficult to identify specific processes and pathways affecting deposition-temperature relationships (Clifton et al., 2019). Fares et al. (2012) reported decreases in stomatal deposition as air temperature and VPD increase in a citrus orchard, relationships that were stronger in the summer than the flowering period. Similarly, in a subalpine forest (Turnipseed

et al., 2009) and a potato field (Coyle et al., 2009), decreases in stomatal deposition with temperature and VPD were observed. Wong et al. (2022) found decreases in stomatal deposition on hot days and days with high VPD at three forested sites, and Fares et al. (2014) found drought stress and high temperatures drove stomata to close, decreasing O_3 uptake. However, Liu et al. (2021) found a positive correlation between total deposition and temperature and attributed this relationship to increasing g_s. Fares et al. (2010) found in a ponderosa pine forest that stomatal O_3 flux (negative indicates downward direction) decreases as temperature increases. The dependence of O_3 flux on O_3 concentration, which has a strong temperature dependence at this site, may influence this relationship. Following the Jarvis model of increasing and then decreasing g_s with temperature, these opposing reports may be influenced by the temperature range during the measurement period, as well as the optimal temperature to promote the maximum g_s over each land cover type. As global temperatures and VPD rise, it is predicted that g_s will decrease (Damour et al., 2010; Grossiord et al., 2020).

A growing body of literature has tied drought and heatwaves to O_3 pollution episodes, primarily due to a decrease in dry deposition. Under drought stress, deposition negatively correlates with VPD (and co-occurring high temperatures) due to stomatal closure (Bauer et al., 2000; Cieslik, 2004; Fares et al., 2014). Lin et al. (2019) found that drought can reduce O_3 deposition by up to 50%. The reduction in deposition during heatwaves and droughts increases O_3 concentrations and is strong enough to counteract benefits of precursor emissions reductions (Huang et al., 2016; Lin et al., 2020). While stomatal deposition decreases under drought conditions, increases in nonstomatal deposition can lead to an overall increase in deposition (Agyei et al., 2020). Drought conditions also alter PO_3, which contributes to changes in O_3 concentration. Lei et al. (2022) attributed drought-driven O_3 increases to increased photochemistry, however in the eastern U.S.

and western Europe, reduced stomatal conductance limiting LO_3 was as important as the increase in PO_3. Changing isoprene emissions during droughts alter PO_3, yet these emissions vary spatially (Demetillo et al., 2019; W. Li et al., 2022). Demetillo et al. (2019) and W. Li et al. (2022) found that drought-decreased isoprene emissions in California reduced PO_3, while in the southeast U.S., W. Li et al. (2022) report increases in isoprene emissions lead to increased PO_3, enhancing O_3 concentrations. While drought-driven changes to PO_3 do not directly affect LO_3, increasing O_3 concentrations can worsen O_3-induced plant damage, limiting future O_3 uptake. If drought and high CO_2 conditions co-occur, the detrimental effects of O_3 uptake may be dampened (Wittig 2007).

Negative consequences of high O_3 abundance and O_3 uptake are measurable as damage to stomatal conductance and photosynthesis, with reported 11% and 13–21% reductions, respectively (Lombardozzi et al., 2013; Wittig et al., 2007). Lombardozzi et al. (2013) found effects of O_3 on stomatal conductance and photosynthesis can decouple. High O_3 impairs stomatal function by reducing plant stomatal control, thus limiting their drought response (Mills et al., 2009) and increases stomatal sluggishness, where O_3 exposure slows stomatal response to light (Paoletti and Grulke, 2010). Ultimately, impaired g_s and photosynthesis due to high O_3 can alter both the terrestrial carbon and O_3 sinks (Sadiq et al., 2017; Wittig et al., 2007; Wittig et al., 2009).

High O_3 conditions can maintain or increase stomatal O_3 uptake, even as reduced g_s limits carbon assimilation (Fares et al., 2013). Zapletal et al. (2011) correlated overall and stomatal deposition with decreased productivity in a Norway spruce forest. Fiscus et al. (2005) assessed the impacts of O_3 on crops, finding that enhanced O_3 inhibits photosynthesis, plant growth, and crop yield. O_3 decreased Rubisco in leaves, reducing carboxylation efficiency, and impaired the function of

photosynthetic electron transport, leading to overall reductions in carbon assimilation. Further, O_3 may attack the guard cells that control stomatal conductance. This may alter conductance but does not inherently reduce carbon assimilation. Both acute and chronic exposure leads to these damages. In addition, the timing of enhanced O_3 and plant phenological stage can affect crop yield (Soja et al., 2000; Younglove et al., 1994). Wittig et al. (2009) report that elevated O_3 reduces tree biomass, root-to-shoot ratio, leaf area, Rubisco content, chlorophyll content, transpiration, tree height, and diameter. Depending on the elevated O_3 concentration, an 11–17% reduction in tree biomass was observed. As global temperatures rise, an earlier onset of the growing season will increase cumulative O_3 uptake, increasing seasonal damage to vegetation (Karlsson et al., 2007).

Damage caused by O_3 uptake extends to the energy budget and water use. VanLoocke et al. (2012) observed reduced latent heat fluxes, increased sensible heat fluxes, increased canopy temperature, reduced seasonal evapotranspiration, and reduced water use efficiency due to high O_3 exposure. O_3 uptake-induced alterations to the energy budget may alter regional hydrology and climate. Elevated O_3 has been found to increase water use in an eastern U.S forest (McLaughlin et al., 2007). Selecting crop varieties that have a high water use efficiency will not only protect them from increasing drought, but also future high O_3 pollution.

Future climate scenarios predict reductions in LO_3 with resultant increases in O_3 pollution (Zapletal et al., 2012). Reduced LO_3 and elevated O_3 directly and indirectly contribute to climate change, not only as a O_3 is a greenhouse gas, but by limiting carbon uptake and altering global hydrological cycling (Arnold et al., 2018; Sitch et al., 2007). By limiting the terrestrial carbon sink, O_3 uptake indirectly contributes to radiative forcing (Sitch et al., 2007). Additionally, while high

temperatures and high VPD decrease g_s (Bunce, 2000; Emberson et al., 2000; Lombardozzi et al., 2013; Sanderson et al., 2007; Wittig et al., 2007), enhanced CO_2 further reduces g_s (Bunce, 2000).

Stomatal deposition can account for <10% to >90% of total dry deposition (Clifton et al., 2020), making understanding the response of stomatal O_3 deposition to climate change critical to predict the multifaceted effects of temperature on LO_3 and resulting effects to plants and carbon, energy, and water cycling, particularly in locations where stomatal loss is the dominant pathway. While both O_3 concentration and O_3 deposition measurements are used, direct measures of O_3 uptake are better at predicting O_3-induced damage than measurements of O_3 exposure (Massman, 2004; Musselman et al., 2006), thus more measurements of LO_3, in more locations, and of longer duration are needed.

1.2.2 Nonstomatal O_3 loss

As with stomatal deposition, the importance of the sensitivity of nonstomatal O_3 deposition to temperature depends on the fraction of LO_3 that occurs via a nonstomatal pathway. Nonstomatal loss can be a minor fraction or a dominant fraction of total loss, depending on location, season, and time of day (Clifton et al., 2020; and references therein). The temperature dependence of nonstomatal loss was first reported by Rondón et al. (1993), and it has since been established that the temperature dependence of nonstomatal loss depends on the specific pathway, as deposition to leaf surfaces, bare soil, and loss to chemistry occur via different mechanisms. Nonstomatal deposition-micrometeorological relationships vary site-to-site due to the importance of specific nonstomatal pathways. These relationships, or lack-thereof, are frequently used to determine the form of nonstomatal loss.

Nonstomatal loss to leaf surfaces can be separated into wet and dry components. Nonstomatal conductance frequently correlates with relative humidity (RH) (Altimir et al., 2006; Clifton et al., 2019; Coyle et al., 2009; Gerosa et al., 2009; Lamaud et al., 2002; Lamaud et al., 2009; Neirynck and Verstraeten, 2018; Rannik et al., 2012; Zhang et al., 2002). Water films on surfaces promote aqueous chemistry, but a threshold of approximately 70% RH is needed to achieve this (Altimir et al., 2006; Coyle et al., 2009). Coyle et al. (2009) found RH between 50% and 70% is insufficient, as the water creates a thin film that blocks the depositional processes. High humidity-driven nonstomatal conductance is frequently reported for overnight or early morning hours while temperatures are low and dew wets the surface (Lamaud et al., 2002; Neirynck and Verstraeten, 2018; Visser et al., 2021). While wet conditions promote surface deposition, the water films may block leaf stomata, reducing stomatal conductance (Zhang et al., 2002).

Evidence suggests that at low humidity, cuticular deposition has a temperature dependence due to thermal decomposition (Cape et al., 2009; Coyle et al., 2009; Fowler et al., 2001), though the cuticular pathway cannot always be distinguished from chemical loss. Coyle et al. (2009) report that on dry surfaces nonstomatal conductance exhibits a temperature dependence that is not present when wet, arguing that thermal decomposition on the leaf surface accounts for this. Fowler et al. (2001) and Cape et al. (2009) find activation energies required for surface uptake, promoting the idea of thermal decomposition. However, Hogg et al. (2007) sees nonstomatal deposition increase with temperature before reaching some optimal temperature, above which it decreases, conflicting with the thermal decomposition theory.

The temperature dependence of LO_3 due to chemistry is well established. Biogenic volatile organic compounds (BVOCs) and nitric oxide (NO) react with O_3, near the soil surface or within canopies.

BVOCs and NO have temperature dependent emissions (Guenther et al., 1991; Pilegaard, 2013). Reactions with BVOCs can account for large fractions of total deposition (Fares et al., 2010; Fares et al., 2012; Goldstein et al., 2004; Kurpius and Goldstein, 2003; Neirynck et al., 2012; Wong et al., 2022). If nonstomatal deposition is temperature dependent, it is frequently attributed to reactions with BVOCs driven by increased emissions (Fares et al., 2010; Fares et al., 2012; Kurpius and Goldstein, 2003; Q. Li et al., 2018; Mikkelsen et al., 2004; Mikkelsen et al., 2000; Neirynck et al., 2012; Neirynck and Verstraeten, 2018; Wong et al., 2022). Kurpius and Goldstein (2003) use the exponential temperature dependence of monoterpene emissions and the chemical fraction of the O_3 flux to determine the nonstomatal pathway. Goldstein et al. (2004) confirmed this chemical pathway by conducting an experiment with forest thinning. Following thinning, enhancements of monoterpene emissions led to enhanced O_3 uptake, exhibiting the same temperature dependence described in Kurpius and Goldstein (2003). Measurements of O_3-BVOC oxidation products above canopies have further identified this nonstomatal loss pathway (Fares et al., 2010; Holzinger et al., 2005; Vermeuel et al., 2021). Neirynck and Verstraeten (2018) find that drought conditions (i.e., high temperatures and high VPD), expected to increase with climate change, can trigger increases in BVOC emissions leading to enhanced O_3 uptake. As global temperatures rise, this uptake pathway may become more prominent. However, detrimental effects of this loss pathway include products of reactions between O_3 and BVOCs that go on to form secondary organic aerosol, a climate forcer, and hydroxyl radicals, which promote PO_3 (Cao et al., 2022; Holzinger et al., 2005).

Chemical loss to NO, particularly via soil emissions, is less dominant and less frequently reported. NO can act as a temporary or permanent sink of O_3. The reaction between O_3 and NO produces NO_2. This NO_2 can be taken up by plant stomata, via the same mechanism as O_3 stomatal uptake,

or oxidized to higher nitrogen oxides (Clifton et al., 2020; and references therein). Both NO_2 removal pathways are permanent O_3 sinks. However, in the presence of sunlight, NO_2 may photolyze back to O_3 and NO. The possibility of O_3 loss via reaction with NO is frequently included by assessing the temperature dependence of the nonstomatal deposition, particularly when there is high nighttime loss (Mikkelsen et al., 2004; Mikkelsen et al., 2000; Neirynck et al., 2012). The contribution of NO to LO_3 has been described both as minor (Rannik et al., 2009; Wong et al., 2022) and significant (Finco et al., 2018; Lamaud et al., 2009; Neirynck and Verstraeten, 2018). However, loss to NO observed by Lamaud et al. (2009) is attributed to anthropogenic sources, not soil emissions, so this loss does not scale with temperature in the same was as loss to soil NO. The drivers of soil NO emissions are complex, based on microbial activity and chemical reactions, and there is significant variability in model-predicted emissions (Pilegaard, 2013). Increased soil NO emissions driven by warming temperatures may increase nonstomatal deposition. To understand how nonstomatal LO_3 will change in terms of climate, continued and new measurement sites with O_3 fluxes, micrometeorological measurements, carbon fluxes, water fluxes, and nitrogen oxide fluxes are needed to determine the fraction of LO_3 that is nonstomatal and the specific nonstomatal pathway.

1.3 Dissertation contents

Improved understanding of the controls on surface PO_3 and LO_3 are needed to accurately predict future O_3 budgets and assess human and environmental health risks. As the climate warms, both PO_3 and LO_3 are expected to change. A warmer climate is predicted to increase O_3 pollution in regions that have abundant precursors, both biogenic and anthropogenic (Szopa, 2021). Regionally

specific understandings of the PO_3 response to warmer temperatures with varying precursor emissions are needed for policymakers to target climate adaptation strategies, particularly in places where PO_3 acts as a dominant control over O_3. Changes to CO_2, temperature, VPD, and precipitation will alter stomatal conductance, and thus stomatal uptake of O_3, as well as plant sensitivity to O_3 (Ainsworth et al., 2012). Complex local and regional changes to LO_3 may alter biogeochemical and biogeophysical cycling (Sadiq et al., 2017; Sitch et al., 2007). Presently, a limited number of long-term LO_3 measurements exist (field campaigns frequently last days to weeks) to validate modeled outcomes (Clifton et al., 2020). More measurements are needed to improve models and constrain individual loss pathways, as different dry deposition parameterizations perform best over different land cover types (Silva and Heald, 2018; Wong et al., 2019).

This dissertation addresses both PO_3 and LO_3 to provide further insights into relationships between O_3 and temperature. Chapter 2 describes trends in O_3 climate penalties ($m_{O3\text{-}T}$) from 1999–2019, demonstrating that PO_3 drives $m_{O3\text{-}T}$ in seven of nine climate regions, and that $m_{O3\text{-}T}$ are responsive to reductions in NO_x emissions at higher NO_2 than PO_3. Chapters 3 and 4 address LO_3. Chapter 3 presents two years of eddy covariance O_3 flux and deposition velocity measurements. Measurements were made in a Central Virginia mixed coniferous and deciduous forest. Chapter 3 describes the instrumentation, setup, and data processing methods used to obtain fluxes and deposition velocities. Chapter 4 presents O_3 fluxes and deposition velocities from Chapter 3 partitioned into the stomatal and nonstomatal components. I assess how stomatal and nonstomatal LO_3 vary with temperature to provide insight into how LO_3 will change with a changing climate. Chapter 5 summarizes the conclusions and the implications of the findings in each of these chapters. Present work can inform O_3 pollution reduction strategies in polluted locations, provide

a modeling constraint for O_3 deposition in the Southeast U.S., and aid in predicting the response of O_3 deposition to climate change.

References

Agyei, T., Juran, S., Ofori-Amanfo, K. K., Sigut, L., Urban, O., and Marek, M. V.: The impact of drought on total ozone flux in a mountain Norway spruce forest, Journal of Forest Science, 66, 280-287, 10.17221/129/2019-jfs, 2020.

Ainsworth, E. A., Yendrek, C. R., Sitch, S., Collins, W. J., and Emberson, L. D.: The effects of tropospheric ozone on net primary productivity and implications for climate change, Annu Rev Plant Biol, 63, 637-661, 10.1146/annurev-arplant-042110-103829, 2012.

Altimir, N., Kolari, P., Touovinen, J.-P., Vesala, T., Bäck, J., Suni, T., Kulmala, M., and Hari, P.: Foliage surface ozone deposition: a role for surface moisture?, Biogeosciences, 3, 209-228, 2006.

Andersson, C., and Engardt, M.: European ozone in a future climate: Importance of changes in dry deposition and isoprene emissions, Journal of Geophysical Research-Atmospheres, 115, 10.1029/2008jd011690, 2010.

Arnold, S. R., Lombardozzi, D., Lamarque, J. F., Richardson, T., Emmons, L. K., Tilmes, S., Sitch, S. A., Folberth, G., Hollaway, M. J., and Martin, M. V.: Simulated Global Climate Response to Tropospheric Ozone-Induced Changes in Plant Transpiration, Geophysical Research Letters, 45, 13070-13079, 10.1029/2018gl079938, 2018.

Ashmore, M. R.: Assessing the future global impacts of ozone on vegetation, Plant, Cell and Environment 28, 949-964, 2005.

Avise, J., Abraham, R. G., Chung, S. H., Chen, J., Lamb, B., Salathe, E. P., Zhang, Y. X., Nolte, C. G., Loughlin, D. H., Guenther, A., Wiedinmyer, C., and Duhl, T.: Evaluating the effects of climate change on summertime ozone using a relative response factor approach for policymakers, Journal of the Air & Waste Management Association, 62, 10.1080/10962247.2012.696531, 2012.

Ball, J. T., Woodrow, I. E., and Berry, J. A.: A Model Predicting Stomatal Conductance and Its Contribution to the Control of Photosynthesis Under Different Environmental Conditions, in: Progress in Photosynthesis Research, edited by: Biggins, J., Nijhoff, Dordrecht, The Netherlands, 221-224, 1987.

Baublitz, C. B., Fiore, A. M., Clifton, O. E., Correa, G., Westervelt, D. M., Horowitz, L. W., and Williams, A. P.: Sensitivity of Tropospheric Ozone Over the Southeast USA to Dry Deposition, Geophysical Research Letters, 47, e2020GL087158, https://doi.org/10.1029/2020GL087158, 2020.

Bauer, M. R., Hultman, N. E., Panek, J. A., and Goldstein, A. H.: Ozone deposition to a ponderosa pine plantation in the Sierra Nevada Mountains (CA): A comparison of two different climatic years, Journal of Geophysical Research, 105, 22123-22136, 2000.

Bloomer, B. J., Stehr, J. W., Piety, C. A., Salawitch, R. J., and Dickerson, R. R.: Observed relationships of ozone air pollution with temperature and emissions, Geophysical Research Letters, 36, L09803, doi:10.1029/2009GL037308, 2009.

Brown-Steiner, B., Hess, P. G., and Lin, M. Y.: On the capabilities and limitations of GCCM simulations of summertime regional air quality: A diagnostic analysis of ozone and temperature simulations in the US using CESM CAM-Chem, Atmospheric Environment, 101, 134-148, 10.1016/j.atmosenv.2014.11.001, 2015.

Buckley, T. N., and Mott, K. A.: Modelling stomatal conductance in response to environmental factors, Plant Cell and Environment, 36, 1691-1699, 10.1111/pce.12140, 2013.

Bunce, J. A.: Responses of stomatal conductance to light, humidity and temperature in winter wheat and barley grown at three concentrations of carbon dioxide in the field, Global Change Biology, 6, 371-382, 2000.

Cao, J., Situ, S., Hao, Y. F., Xie, S. D., and Li, L. Y.: Enhanced summertime ozone and SOA from biogenic volatile organic compound (BVOC) emissions due to vegetation biomass variability during 1981-2018 in China, Atmospheric Chemistry and Physics, 22, 2351-2364, 10.5194/acp-22-2351-2022, 2022.

Cape, J. N., Hamilton, R., and Heal, M. R.: Reactive uptake of ozone at simulated leaf surfaces: Implications for 'non-stomatal' ozone flux, Atmospheric Environment, 43, 1116-1123, 10.1016/j.atmosenv.2008.11.007, 2009.

Cieslik, S. A.: Ozone uptake by various surface types: a comparison between dose and exposure, Atmospheric Environment, 38, 2409-2420, 10.1016/j.atmosenv.2003.10.063, 2004.

Clifton, O. E., Fiore, A. M., Munger, J. W., and Wehr, R.: Spatiotemporal Controls on Observed Daytime Ozone Deposition Velocity Over Northeastern US Forests During Summer, Journal of Geophysical Research-Atmospheres, 124, 5612-5628, 10.1029/2018jd029073, 2019.

Clifton, O. E., Fiore, A. M., Massman, W. J., Baublitz, C. B., Coyle, M., Emberson, L., Fares, S., Farmer, D. K., Gentine, P., Gerosa, G., Guenther, A. B., Helmig, D., Lombardozzi, D. L., Munger, J. W., Patton, E. G., Pusede, S. E., Schwede, D. B., Silva, S. J., Sörgel, M., Steiner, A. L., and Tai, A. P. K.: Dry Deposition of Ozone over Land: Processes, Measurement, and Modeling, Reviews of Geophysics, 58, 10.1029/2019RG000670, 2020.

Coates, J., Mar, K. A., Ojha, N., and Butler, T. M.: The influence of temperature on ozone production under varying NOx conditions – a modelling study, Atmospheric Chemistry and Physics, 16, 11601-11615, 10.5194/acp-16-11601-2016, 2016.

Coyle, M., Nemitz, E., Storeton-West, R., Fowler, D., and Cape, J. N.: Measurements of ozone deposition to a potato canopy, Agricultural and Forest Meteorology, 149, 655-666, 10.1016/j.agrformet.2008.10.020, 2009.

Damour, G., Simonneau, T., Cochard, H., and Urban, L.: An overview of models of stomatal conductance at the leaf level, Plant Cell and Environment, 33, 1419-1438, 10.1111/j.1365-3040.2010.02181.x, 2010.

Demetillo, M. A. G., Anderson, J. F., Geddes, J. A., Yang, X., Najacht, E. Y., Herrera, S. A., Kabasares, K. M., Kotsakis, A. E., Lerdau, M. T., and Pusede, S. E.: Observing Severe Drought Influences on Ozone Air Pollution in California, Environmental Science & Technology, 53, 4695-4706, 10.1021/acs.est.8b04852, 2019.

Emberson, L. D., Wieser, G., and Ashmore, M. R.: Modelling of stomatal conductance and ozone flux of Norway spruce: comparison with field data, Environmental Pollution, 109, 393-402, 10.1016/s0269-7491(00)00042-7, 2000.

Fares, S., McKay, M., Holzinger, R., and Goldstein, A. H.: Ozone fluxes in a Pinus ponderosa ecosystem are dominated by non-stomatal processes: Evidence from long-term continuous measurements, Agricultural and Forest Meteorology, 150, 420-431, 10.1016/j.agrformet.2010.01.007, 2010.

Fares, S., Weber, R., Park, J. H., Gentner, D., Karlik, J., and Goldstein, A. H.: Ozone deposition to an orange orchard: Partitioning between stomatal and non-stomatal sinks, Environ Pollut, 169, 258-266, 10.1016/j.envpol.2012.01.030, 2012.

Fares, S., Vargas, R., Detto, M., Goldstein, A. H., Karlik, J., Paoletti, E., and Vitale, M.: Tropospheric ozone reduces carbon assimilation in trees: estimates from analysis of continuous flux measurements, Glob Chang Biol, 19, 2427-2443, 10.1111/gcb.12222, 2013.

Fares, S., Savi, F., Muller, J., Matteucci, G., and Paoletti, E.: Simultaneous measurements of above and below canopy ozone fluxes help partitioning ozone deposition between its various sinks in a Mediterranean Oak Forest, Agricultural and Forest Meteorology, 198-199, 181-191, 10.1016/j.agrformet.2014.08.014, 2014.

Finco, A., Coyle, M., Nemitz, E., Marzuoli, R., Chiesa, M., Loubet, B., Fares, S., Diaz-Pines, E., Gasche, R., and Gerosa, G.: Characterization of ozone deposition to a mixed oak-hornbeam forest - flux measurements at five levels above and inside the canopy and their interactions with nitric oxide, Atmospheric Chemistry and Physics, 18, 17945-17961, 10.5194/acp-18-17945-2018, 2018.

Fiore, A. M., Naik, V., Spracklen, D. V., Steiner, A., Unger, N., Prather, M., Bergmann, D., Cameron-Smith, P. J., Cionni, I., Collins, W. J., Dalsoren, S., Eyring, V., Folberth, G. A., Ginoux, P., Horowitz, L. W., Josse, B., Lamarque, J. F., MacKenzie, I. A., Nagashima, T., O'Connor, F. M., Righi, M., Rumbold, S. T., Shindell, D. T., Skeie, R. B., Sudo, K., Szopa, S., Takemura, T., and Zeng, G.: Global air quality and climate, Chemical Society Reviews, 41, 6663-6683, 10.1039/c2cs35095e, 2012.

Fiscus, E. L., Booker, F. L., and Burkey, K. O.: Crop responses to ozone: uptake, modes of action, carbon assimilation and partitioning, Plant, Cell and Environment, 28, 997-1011, 2005.

Fowler, D., Flechard, C., Cape, J. N., Storeton-West, R., and Coyle, M.: Measurements of ozone deposition to vegetation quantifying the flux, the stomatal and non-stomatal components, Water, Air and Soil Pollution, 130, 63-74, 2001.

Fowler, D., Pilegaard, K., Sutton, M. A., Ambus, P., Raivonen, M., Duyzer, J., Simpson, D., Fagerli, H., Fuzzi, S., Schjoerring, J. K., Granier, C., Neftel, A., Isaksen, I. S. A., Laj, P., Maione, M., Monks, P. S., Burkhardt, J., Daemmgen, U., Neirynck, J., Personne, E., Wichink-Kruit, R., Butterbach-Bahl, K., Flechard, C., Tuovinen, J. P., Coyle, M., Gerosa, G., Loubet, B., Altimir, N., Gruenhage, L., Ammann, C., Cieslik, S., Paoletti, E., Mikkelsen, T. N., Ro-Poulsen, H., Cellier, P., Cape, J. N., Horváth, L., Loreto, F., Niinemets, Ü., Palmer, P. I., Rinne, J., Misztal, P., Nemitz, E., Nilsson, D., Pryor, S., Gallagher, M. W., Vesala, T., Skiba, U., Brüggemann, N., Zechmeister-Boltenstern, S., Williams, J., O'Dowd, C., Facchini, M. C., de Leeuw, G., Flossman, A., Chaumerliac, N., and Erisman, J. W.: Atmospheric composition change: Ecosystems–Atmosphere interactions, Atmospheric Environment, 43, 5193-5267, 10.1016/j.atmosenv.2009.07.068, 2009.

Garland, J. A., and Derwent, R. G.: Destruction at the ground and the diurnal cycle of concentration of ozone and other gases, Quarterly Journal of the Royal Meteorological Society, 105, 169-183, 10.1002/qj.49710544311, 1979.

Gerosa, G., Finco, A., Mereu, S., Marzuoli, R., and Ballarin-Denti, A.: Interactions among vegetation and ozone, water and nitrogen fluxes in a coastal Mediterranean maquis ecosystem, Biogeosciences, 6, 1783-1798, 10.5194/bg-6-1783-2009, 2009.

Goldstein, A. H., McKay, M., Kurpius, M. R., Schade, W., Lee, A., Holzinger, R., and Rasmussen, R. A.: Forest thinning experiment confirms ozone deposition to forest canopy is dominated by reaction with biogenic VOCs, Geophysical Research Letters, 31, L22106, 10.1029/2004GL021259, 2004.

Grossiord, C., Buckley, T. N., Cernusak, L. A., Novick, K. A., Poulter, B., Siegwolf, R. T. W., Sperry, J. S., and McDowell, N. G.: Plant responses to rising vapor pressure deficit, New Phytologist, 226, 1550-1566, 2020.

Guenther, A. B., Monson, R. K., and Fall, R.: Isoprene and monoterpene emission rate variability: Observations with eucalyptus and emission rate algorithm development, Journal of Geophysical Research-Atmospheres, 96, 10799-10808, 10.1029/91jd00960, 1991.

Guenther, A. B., Zimmerman, P. R., Harley, P. C., Monson, R. K., and Fall, R.: Isoprene and Monoterpene Emission Rate Variability: Model Evaluations and Sensitivity Analysis, Journal of Geophysical Research-Atmospheres, 98, 12609-12617, 10.1029/93jd00527, 1993.

He, H., Hembeck, L., Hosley, K. M., Canty, T. P., Salawitch, R. J., and Dickerson, R. R.: High ozone concentrations on hot days: The role of electric power demand and NO_x emissions, Geophysical Research Letters, 40, 5291-5294, 10.1002/grl.50967, 2013.

Hogg, A., Uddling, J., Ellsworth, D., Carroll, M. A., Pressley, S., Lamb, B., and Vogel, C.: Stomatal and non-stomatal fluxes of ozone to a northern mixed hardwood forest, Tellus B: Chemical and Physical Meteorology, 59, 514-525, 10.1111/j.1600-0889.2007.00269.x, 2007.

Holzinger, R., Lee, A., Paw, K. T., and Goldstein, A. H.: Observations of oxidation products above a forest imply biogenic emissions of very reactive compounds, Atmospheric Chemistry and Physics, 5, 67-75, https://doi.org/10.5194/acp-5-67-2005, 2005.

Huang, L., McDonald-Buller, E. C., McGaughey, G., Kimura, Y., and Allen, D. T.: The impact of drought on ozone dry deposition over eastern Texas, Atmospheric Environment, 127, 176-186, http://dx.doi.org/10.1016/j.atmosenv.2015.12.022, 2016.

Ito, A., Sillman, S., and Penner, J. E.: Global chemical transport model study of ozone response to changes in chemical kinetics and biogenic volatile organic compounds emissions due to increasing temperatures: Sensitivities to isoprene nitrate chemistry and grid resolution, Journal of Geophysical Research-Atmospheres, 114, 10.1029/2008jd011254, 2009.

Jacob, D. J., and Winner, D. A.: Effect of climate change on air quality, Atmospheric Environment, 43, 51-63, 10.1016/j.atmosenv.2008.09.051, 2009.

Jarvis, P. G.: Interpretation of variation in leaf water potential and stomatal conductance found in canopies in field, Philosophical Transactions of the Royal Society of London Series B-Biological Sciences, 273, 593-610, 10.1098/rstb.1976.0035, 1976.

Jay, A., Reidmiller, D. R., Avery, C. W., Barrie, D., DeAngelo, B. J., Dave, A., Dzaugis, M., Kolian, M., Lewis, K. L. M., Reeves, K., and Winner, D.: Overview, Impacts, Risks, and Adaptation in the United States: Fourth National Climate Assessment, Volume II, U.S. Global Change Research Program, Washington, D.C., 33-71, 2018.

Jerrett, M., Burnett, R. T., Pope III, C. A., Ito, K., Thurston, G., Krewski, D., Shi, Y., Calle, E., and Thun, M.: Long-Term Ozone Exposure and Mortality, The New England Journal of Medicine, 360, 1085-1095, 2009.

Karlsson, P. E., Tang, L., Sundberg, J., Chen, D., Lindskog, A., and Pleijel, H.: Increasing risk for negative ozone impacts on vegetation in northern Sweden, Environmental Pollution, 150, 96-106, 10.1016/j.envpol.2007.06.016, 2007.

Kavassalis, S. C., and Murphy, J. G.: Understanding ozone-meteorology correlations: A role for dry deposition, Geophysical Research Letters, 44, 2922-2931, 10.1002/2016gl071791, 2017.

Kurpius, M. R., and Goldstein, A. H.: Gas-phase chemistry dominates O_3 loss to a forest, implying a source of aerosols and hydroxyl radicals to the atmosphere, Geophysical Research Letters, 30, 10.1029/2002gl016785, 2003.

Lamaud, E., Carrara, A., Brunet, Y., Lopez, A., and Druilhet, A.: Ozone fluxes above and within a pine forest canopy in dry and wet conditions, Atmospheric Environment, 36, 77-88, 2002.

Lamaud, E., Loubet, B., Irvine, M., Stella, P., Personne, E., and Cellier, P.: Partitioning of ozone deposition over a developed maize crop between stomatal and non-stomatal uptakes, using eddy-covariance flux measurements and modelling, Agricultural and Forest Meteorology, 149, 1385-1396, 10.1016/j.agrformet.2009.03.017, 2009.

Lee, L., Wooldridge, P. J., Gilman, J. B., Warneke, C., de Gouw, J., and Cohen, R. C.: Low temperatures enhance organic nitrate formation: evidence from observations in the 2012 Uintah Basin Winter Ozone Study, Atmospheric Chemistry and Physics, 14, 12441-12454, 10.5194/acp-14-12441-2014, 2014.

Lei, Y. D., Yue, X., Liao, H., Zhang, L., Zhou, H., Tian, C. G., Gong, C., Ma, Y. M., Cao, Y., Seco, R., Karl, T., and Potosnak, M.: Global Perspective of Drought Impacts on Ozone Pollution Episodes, Environmental Science & Technology, 56, 3932-3940, 10.1021/acs.est.1c07260, 2022.

Li, J., Mao, J., Fiore, A. M., Cohen, R. C., Crounse, J. D., Teng, A. P., Wennberg, P. O., Lee, B. H., Lopez-Hilfiker, F. D., Thornton, J. A., Peischl, J., Pollack, I. B., Ryerson, T. B., Veres, P., Roberts, J. M., Neuman, J. A., Nowak, J. B., Wolfe, G. M., Hanisco, T. F., Fried, A., Singh, H. B., Dibb, J., Paulot, F., and Horowitz, L. W.: Decadal changes in summertime reactive oxidized nitrogen and surface ozone over the Southeast United States, Atmospheric Chemistry and Physics, 18, 2341-2361, https://doi.org/10.5194/acp-18-2341-2018, 2018.

Li, Q., Gabay, M., Rubin, Y., Fredj, E., and Tas, E.: Measurement-based investigation of ozone deposition to vegetation under the effects of coastal and photochemical air pollution in the Eastern Mediterranean, Sci. Total Environ., 645, 1579-1597, 10.1016/j.scitotenv.2018.07.037, 2018.

Li, W., Wang, Y. X., Flynn, J., Griffin, R. J., Guo, F. Z., and Schnell, J. L.: Spatial Variation of Surface O_3 Responses to Drought Over the Contiguous United States During Summertime: Role of Precursor Emissions and Ozone Chemistry, Journal of Geophysical Research-Atmospheres, 127, 10.1029/2021jd035607, 2022.

Lin, M., Malyshev, S., Shevliakova, E., Paulot, F., Horowitz, L. W., Fares, S., Mikkelsen, T. N., and Zhang, L.: Sensitivity of ozone dry deposition to ecosystem-atmosphere interactions: A critical appraisal of observations and simulations, Global Biogeochemical Cycles, 33, 1264-1288, https://doi.org/10.1029/2018GB006157, 2019.

Lin, M., Horowitz, L. W., Xie, Y., Paulot, F., Malyshev, S., Shevliakova, E., Finco, A., Gerosa, G., Kubistin, D., and Pilegaard, K.: Vegetation feedbacks during drought exacerbate ozone air pollution extremes in Europe, Nature Climate Change, 10, 444-451, https://doi.org/10.1038/s41558-020-0743-y, 2020.

Liu, Z., Pan, Y. P., Song, T., Hu, B., Wang, L. L., and Wang, Y. S.: Eddy covariance measurements of ozone flux above and below a southern subtropical forest canopy, Sci. Total Environ., 791, 10.1016/j.scitotenv.2021.148338, 2021.

Lombardozzi, D., Sparks, J. P., and Bonan, G.: Integrating O_3 influences on terrestrial processes: photosynthetic and stomatal response data available for regional and global modeling, Biogeosciences, 10, 6815-6831, 10.5194/bg-10-6815-2013, 2013.

Massman, W. J.: Toward an ozone standard to protect vegetation based on effective dose: a review of deposition resistances and a possible metric, Atmospheric Environment, 38, 2323-2337, 10.1016/j.atmosenv.2003.09.079, 2004.

McLaughlin, S. B., Wullschleger, S. D., Sun, G., and Nosal, M.: Interactive effects of ozone and climate on water use, soil moisture content and streamflow in a southern Appalachian forest in the USA, New Phytologist, 174, 125-136, 10.1111/j.1469-8137.2007.01970.x, 2007.

Mikkelsen, T. N., Ro-Poulsen, H., Pilegaard, K., Hovmand, M. F., Jensen, N. O., Christensen, C. S., and Hummelshoej, P.: Ozone uptake by an evergreen forest canopy: temporal variation and possible mechanisms, Environmental Pollution, 109, 423-429, 2000.

Mikkelsen, T. N., Ro-Poulsen, H., Hovmand, M. F., Jensen, N. O., Pilegaard, K., and Egelov, A. H.: Five-year measurements of ozone fluxes to a Danish Norway spruce canopy, Atmospheric Environment, 38, 2361-2371, 10.1016/j.atmosenv.2003.12.036, 2004.

Mills, G., Hayes, F., Wilkinson, S., and Davies, W. J.: Chronic exposure to increasing background ozone impairs stomatal functioning in grassland species, Global Change Biology, 15, 1522-1533, 10.1111/j.1365-2486.2008.01798.x, 2009.

Monks, P. S., Archibald, A. T., Colette, A., Cooper, O., Coyle, M., Derwent, R., Fowler, D., Granier, C., Law, K. S., Mills, G. E., Stevenson, D. S., Tarasova, O., Thouret, V., von Schneidemesser, E., Sommariva, R., Wild, O., and Williams, M. L.: Tropospheric ozone and its precursors from the urban to the global scale from air quality to short-lived climate forcer, Atmospheric Chemistry and Physics, 15, 8889-8973, 10.5194/acp-15-8889-2015, 2015.

Musselman, R. C., Lefohn, A. S., Massman, W. J., and Heath, R. L.: A critical review and analysis of the use of exposure- and flux-based ozone indices for predicting vegetation effects, Atmospheric Environment, 40, 1869-1888, 10.1016/j.atmosenv.2005.10.064, 2006.

Neirynck, J., Gielen, B., Janssens, I. A., and Ceulemans, R.: Insights into ozone deposition patterns from decade-long ozone flux measurements over a mixed temperate forest, J Environ Monit, 14, 1684-1695, 10.1039/c2em10937a, 2012.

Neirynck, J., and Verstraeten, A.: Variability of Ozone Deposition Velocity Over a Mixed Suburban Temperate Forest, Frontiers in Environmental Science, 6, 10.3389/fenvs.2018.00082, 2018.

Ninneman, M., and Jaffe, D.: Observed Relationship between Ozone and Temperature for Urban Nonattainment Areas in the United States, Atmosphere, 12, 1235, https://doi.org/10.3390/atmos12101235, 2021.

Nolte, C. G., Spero, T. L., Bowden, J. H., Sarofim, M. C., Martinich, J., and Mallard, M. S.: Regional temperature-ozone relationships across the U.S. under multiple climate and emissions scenarios, Journal of the Air & Waste Management Association, 71, 1251-1264, 10.1080/10962247.2021.1970048, 2021.

Nussbaumer, C. M., and Cohen, R. C.: The Role of Temperature and NO_x in Ozone Trends in the Los Angeles Basin, Environmental Science & Technology, 54, 15652-15659, 10.1021/acs.est.0c04910, 2020.

Paoletti, E., and Grulke, N. E.: Ozone exposure and stomatal sluggishness in different plant physiognomic classes, Environ Pollut, 158, 2664-2671, 10.1016/j.envpol.2010.04.024, 2010.

Perdigones, B. C., Lee, S., Cohen, R. C., Park, J. H., and Min, K. E.: Two Decades of Changes in Summertime Ozone Production in California's South Coast Air Basin, Environmental Science & Technology, 56, 10586-10595, 10.1021/acs.est.2c0102610586, 2022.

Pilegaard, K.: Processes regulating nitric oxide emissions from soils, Philosophical Transactions of the Royal Society B-Biological Sciences, 368, 10.1098/rstb.2013.0126, 2013.

Pusede, S. E., and Cohen, R. C.: On the observed response of ozone to NO_x and VOC reactivity reductions in San Joaquin Valley California 1995-present, Atmospheric Chemistry and Physics, 12, 8323-8339, 10.5194/acp-12-8323-2012, 2012.

Pusede, S. E., Gentner, D. R., Wooldridge, P. J., Browne, E. C., Rollins, A. W., Min, K. E., Russell, A. R., Thomas, J., Zhang, L., Brune, W. H., Henry, S. B., DiGangi, J. P., Keutsch, F. N., Harrold, S. A., Thornton, J. A., Beaver, M. R., St. Clair, J. M., Wennberg, P. O., Sanders, J., Ren, X., VandenBoer, T. C., Markovic, M. Z., Guha, A., Weber, R., Goldstein, A. H., and Cohen, R. C.: On the temperature dependence of organic reactivity, nitrogen oxides, ozone production, and the impact of emission controls in San Joaquin Valley, California, Atmospheric Chemistry and Physics, 14, 3373-3395, 10.5194/acp-14-3373-2014, 2014.

Pusede, S. E., Steiner, A. L., and Cohen, R. C.: Temperature and recent trends in the chemistry of continental surface ozone, Chem Rev, 115, 3898-3918, 10.1021/cr5006815, 2015.

Rannik, U., Mammarella, I., Keronen, P., and Vesala, T.: Vertical advection and nocturnal deposition of ozone over a boreal pine forest, Atmospheric Chemistry and Physics, 9, 2089-2095, 2009.

Rannik, U., N. Altimir, N., Mammarella, I., Bäck, J., Rinne, J., Ruuskanen, T. M., Hari, P., Vesala, T., and Kulmala, M.: Ozone deposition into a boreal forest over a decade of observations: evaluating deposition partitioning and driving variables, Atmospheric Chemistry and Physics, 12, 12165-12182, 10.5194/acp-12-12165-2012, 2012.

Rasmussen, D. J., Fiore, A. M., Naik, V., Horowitz, L. W., McGinnis, S. J., and Schultz, M. G.: Surface ozone-temperature relationships in the eastern US: A monthly climatology for evaluating chemistry-climate models, Atmospheric Environment, 47, 142-153, 10.1016/j.atmosenv.2011.11.021, 2012.

Rasmussen, D. J., Hu, J. L., Mahmud, A., and Kleeman, M. J.: The Ozone-Climate Penalty: Past, Present, and Future, Environmental Science & Technology, 47, 14258-14266, 10.1021/es403446m, 2013.

Reich, P. B.: Quantifying plant response to ozone: a unifying theory, Tree Physiol, 3, 63-91, 10.1093/treephys/3.1.63, 1987.

Rieder, H. E., Fiore, A. M., Clifton, O. E., Correa, G., Horowitz, L. W., and Naik, V.: Combining model projections with site-level observations to estimate changes in distributions and seasonality of ozone in surface air over the U.S.A., Atmospheric Environment, 193, 302-315, https://doi.org/10.1016/j.atmosenv.2018.07.042, 2018.

Romer, P. S., Duffey, K. C., Wooldridge, P. J., Edgerton, E., Baumann, K., Feiner, P. A., Miller, D. O., Brune, W. H., Koss, A. R., de Gouw, J. A., Misztal, P. K., Goldstein, A. H., and Cohen, R. C.: Effects of temperature-dependent NO_x emissions on continental ozone production, Atmospheric Chemistry and Physics, 18, 2601-2614, https://doi.org/10.5194/acp-18-2601-2018, 2018.

Rondón, A., Johansson, C., and Granat, L.: Dry deposition of nitrogen dioxide and ozone to coniferous forests, Journal of Geophysical Research-Atmospheres, 98, 5159-5172, 10.1029/92jd02335, 1993.

Sadiq, M., Tai, A. P. K., Lombardozzi, D., and Val Martin, M.: Effects of ozone–vegetation coupling on surface ozone air quality via biogeochemical and meteorological feedbacks, Atmospheric Chemistry and Physics, 17, 3055-3066, 10.5194/acp-17-3055-2017, 2017.

Sanderson, M. G., Collins, W. J., Hemming, D. L., and Betts, R. A.: Stomatal conductance changes due to increasing carbon dioxide levels: Projected impact on surface ozone levels, Tellus Series B-Chemical and Physical Meteorology, 59, 404-411, 10.1111/j.1600-0889.2007.00277.x, 2007.

Sillman, S., and Samson, F. J.: Impact of temperature on oxidant photochemistry in urban polluted rural and remote environments, Journal of Geophysical Research-Atmospheres, 100, 11497-11508, 10.1029/94jd02146, 1995.

Silva, S. J., and Heald, C. L.: Investigating Dry Deposition of Ozone to Vegetation, Journal of Geophysical Research-Atmospheres, 123, 559-573, 10.1002/2017jd027278, 2018.

Sitch, S., Cox, P. M., Collins, W. J., and Huntingford, C.: Indirect radiative forcing of climate change through ozone effects on the land-carbon sink, Nature, 448, 791-794, 10.1038/nature06059, 2007.

Soja, G., Barnes, J. D., Posch, M., Vandermeiren, K., Pleijel, H., and Mills, G.: Phenological weighting of ozone exposures in the calculation of critical levels for wheat, bean and plantain, Environmental Pollution, 109, 517-524, 10.1016/s0269-7491(00)00055-5, 2000.

Steiner, A. L., Tonse, S., Cohen, R. C., Goldstein, A. H., and Harley, R. A.: Influence of future climate and emissions on regional air quality in California, Journal of Geophysical Research, 111, 10.1029/2005jd006935, 2006.

Steiner, A. L., Davis, A. J., Sillman, S., Owen, R. C., Michalak, A. M., and Fiore, A. M.: Observed suppression of ozone formation at extremely high temperatures due to chemical and biophysical feedbacks, Proc Natl Acad Sci U S A, 107, 19685-19690, 10.1073/pnas.1008336107, 2010.

Szopa, S., V. Naik, B. Adhikary, P. Artaxo, T. Berntsen, W.D. Collins, S. Fuzzi, L. Gallardo, A. Kiendler-Scharr, Z. Klimont, H. Liao, N. Unger, and P. Zanis: Short-Lived Climate Forcers in Climate Change 2021: The Physical Science Basis. Contribution of Working Group I to the Sixth Assessment Report of the Intergovernmental Panel on Climate Change, Intergovernmental Panel on Climate Change, Cambridge, United Kingdom and New York, NY, USA, 817–922, 2021.

Tuovinen, J. P., Emberson, L., and Simpson, D.: Modelling ozone fluxes to forests for risk assessment: status and prospects, Annals of Forest Science, 66, 10.1051/forest/2009024, 2009.

Turnipseed, A. A., Burns, S. P., Moore, D. J. P., Hu, J., Guenther, A. B., and Monson, R. K.: Controls over ozone deposition to a high elevation subalpine forest, Agricultural and Forest Meteorology, 149, 1447-1459, 10.1016/j.agrformet.2009.04.001, 2009.

Urban, J., Ingwers, M., McGuire, M. A., and Teskey, R. O.: Stomatal conductance increases with rising temperature, Plant Signal Behav, 12, e1356534, 10.1080/15592324.2017.1356534, 2017.

VanLoocke, A., Betzelberger, A. M., Ainsworth, E. A., and Bernacchi, C. J.: Rising ozone concentrations decrease soybean evapotranspiration and water use efficiency whilst increasing canopy temperature, New Phytol, 195, 164-171, 10.1111/j.1469-8137.2012.04152.x, 2012.

Vermeuel, M. P., Cleary, P. A., Desai, A. R., and Bertram, T. H.: Simultaneous Measurements of O3 and HCOOH Vertical Fluxes Indicate Rapid In-Canopy Terpene Chemistry Enhances O3 Removal Over Mixed Temperate Forests, Geophysical Research Letters, 48, 2020GL090996, 10.1029/2020GL090996, 2021.

Visser, A. J., Ganzeveld, L. N., Goded, I., Krol, M. C., Mammarella, I., Manca, G., and Boersma, K. F.: Ozone deposition impact assessments for forest canopies require accurate ozone flux partitioning on diurnal timescales, Atmospheric Chemistry and Physics, 21, 18393-18411, 10.5194/acp-21-18393-2021, 2021.

von Schneidemesser, E., Monks, P. S., Allan, J. D., Bruhwiler, L., Forster, P., Fowler, D., Lauer, A., Morgan, W. T., Paasonen, P., Righi, M., Sindelarova, K., and Sutton, M. A.: Chemistry and the Linkages between Air Quality and Climate Change, Chemical Reviews, 115, 3856−3897, 10.1021/acs.chemrev.5b00089, 2015.

Wittig, V. E., Ainsworth, E. A., and Long, S. P.: To what extent do current and projected increases in surface ozone affect photosynthesis and stomatal conductance of trees? A meta-analytic review of the last 3 decades of experiments, Plant Cell Environ, 30, 1150-1162, 10.1111/j.1365-3040.2007.01717.x, 2007.

Wittig, V. E., Ainsworth, E. A., Naidu, S. L., Karnosky, D. F., and Long, S. P.: Quantifying the impact of current and future tropospheric ozone on tree biomass, growth, physiology and biochemistry: a quantitative meta-analysis, Global Change Biology, 15, 396-424, 10.1111/j.1365-2486.2008.01774.x, 2009.

Wong, A. Y. H., Geddes, J. A., Tai, A. P. K., and Silva, S. J.: Importance of dry deposition parameterization choice in global simulations of surface ozone, Atmospheric Chemistry and Physics, 19, 14365-14385, 10.5194/acp-19-14365-2019, 2019.

Wong, A. Y. H., Geddes, J. A., Ducker, J. A., Holmes, C. D., Fares, S., Goldstein, A. H., Mammarella, I., and Munger, J. W.: New Evidence for the Importance of Non-Stomatal Pathways in Ozone Deposition During Extreme Heat and Dry Anomalies, Geophysical Research Letters, 49, 10.1029/2021gl095717, 2022.

Wu, S., Mickley, L. J., Leibensperger, E. M., Jacob, D. J., Rind, D., and Streets, D. G.: Effects of 2000–2050 global change on ozone air quality in the United States, Journal of Geophysical Research Atmospheres, 113, D06302, 10.1029/2007JD008917, 2008.

Younglove, T., McCool, P. M., Musselman, R. C., and Kahl, M. E.: Growth-stage dependent crop yield response to ozone exposure, Environmental Pollution, 86, 287-295, 10.1016/0269-7491(94)90169-4, 1994.

Zapletal, M., Cudlin, P., Chroust, P., Urban, O., Pokorny, R., Edwards-Jonasova, M., Czerny, R., Janous, D., Taufarova, K., Vecera, Z., Mikuska, P., and Paoletti, E.: Ozone flux over a Norway spruce forest and correlation with net ecosystem production, Environ Pollut, 159, 1024-1034, 10.1016/j.envpol.2010.11.037, 2011.

Zapletal, M., Pretel, J., Chroust, P., Cudlin, P., Edwards-Jonasova, M., Urban, O., Pokorny, R., Czerny, R., and Hunova, I.: The influence of climate change on stomatal ozone flux to a mountain Norway spruce forest, Environmental Pollution, 169, 267-273, 10.1016/j.envpol.2012.05.008, 2012.

Zhang, J. F., Wei, Y. J., and Fang, Z. F.: Ozone Pollution: A Major Health Hazard Worldwide, Front. Immunol., 10, 10, 10.3389/fimmu.2019.02518, 2019.

Zhang, L., Brook, J. R., and Vet, R.: On ozone dry deposition—with emphasis on non-stomatal uptake and wet canopies, Atmosperic Environment, 36, 4787-4799, https://doi.org/10.1016/S1352-2310(02)00567-8, 2002.

Zhao, S. L., Pappin, A. J., Mesbah, S. M., Zhang, J. Y. J., MacDonald, N. L., and Hakami, A.: Adjoint estimation of ozone climate penalties, Geophysical Research Letters, 40, 5559-5563, 10.1002/2013gl057623, 2013.

CHAPTER 2: ON THE OBSERVED NO_2 DEPENDENCE OF THE OZONE CLIMATE PENALTY ACROSS THE CONTIGUOUS UNITED STATES

A slightly modified version of this chapter is under review at *Environmental Science & Technology*.

2.1 Introduction

Tropospheric ozone (O_3) has a well-known temperature dependence (Pusede et al., 2015; Sillman and Samson, 1995), and warmer temperatures, among other climate change impacts, are predicted to worsen O_3 air quality in the coming decades (Fiore et al., 2012; Jacob and Winner, 2009). Temperature drives numerous processes affecting O_3 production, loss, and transport, with the net O_3 sensitivity to temperature commonly referred to as the O_3 climate penalty (Bloomer et al., 2009; Wu et al., 2008). Over the last half century, O_3 climate penalties have been reported in the range of 0–8 ppb O_3 $^oC^{-1}$ across the contiguous U.S. (Avise et al., 2012; Brown-Steiner et al., 2015; Ninneman and Jaffe, 2021; Nolte et al., 2021; Rasmussen et al., 2012; Rasmussen et al., 2013; Steiner et al., 2010; Zhao et al., 2013). There are multiple formulations of the climate penalty, but each describes the change in O_3 mixing ratio with a change in temperature, typically as the slope of their regression (Bloomer et al., 2009). The O_3 climate penalty is often framed as the additional reduction in O_3 precursor emissions required to offset future warming temperatures (Bloomer et al., 2009; Pusede et al., 2015; Rasmussen et al., 2013; Wu et al., 2008). While the effects of climate change on O_3 are multifaceted, knowledge of relationships between O_3 climate penalties and O_3 precursors is critical because emission controls, especially on nitrogen oxides ($NO_x \equiv NO + NO_2$), are the primary tool currently available to urban air quality managers for O_3-related climate adaptation (Coates et al., 2016; Li, 2018; Rieder et al., 2018).

Surface O_3 is harmful to people and plants (Ainsworth et al., 2012; Cohen et al., 2017; Jerrett et al., 2009; Reich, 1987). O_3 is regulated in the U.S. as a criteria pollutant under the Clean Air Act, leading to major improvements in O_3 air quality, specifically from emissions controls on O_3 precursors, NO_x and volatile organic compounds (VOCs) (Cooper et al., 2012; Simon et al., 2015). Reductions in O_3 precursor emissions alter the temperature dependence of O_3 production (PO_3) chemistry and have contributed to lowered O_3 climate penalties in many polluted urban areas (Bloomer et al., 2009; Pusede et al., 2015; Rasmussen et al., 2012; Steiner et al., 2006). O_3 loss is also climate sensitive and affected by the combined dependence of plant stomatal conductance on temperature and water stress (Bunce, 2000; Demetillo et al., 2019; Fowler et al., 2009; Kavassalis and Murphy, 2017; Tawfik and Steiner, 2013; Urban et al., 2017), with climate change predicted to cause more frequent and severe droughts in the near future (Dai, 2011). Multiscale and climate-sensitive atmospheric features such as the jet stream (Barnes and Fiore, 2013; Kerr et al., 2020) and Bermuda High (Kerr et al., 2019; Shen et al., 2015) explain a substantial portion of O_3-temperature relationships in regions where they are important, and stagnant atmospheric conditions, which are predicted to be more common in many locations with climate change, correspond to higher surface temperatures and worsened O_3 air pollution (Brown-Steiner et al., 2015; Camalier et al., 2007; Fiore et al., 2012; Jacob and Winner, 2009; Jaffe and Zhang, 2017; Kerr et al., 2019; Kerr et al., 2020; Otero et al., 2022; Porter and Heald, 2019; Tawfik and Steiner, 2013). This confluence of factors influences the effectiveness of emission controls on O_3 and its climate penalty, with steeper reductions in anthropogenic O_3 precursors potentially required to protect public health from poor O_3 air quality in the coming decades than would be otherwise needed (Wu et al., 2008).

In this manuscript, I describe the observed dependence of O_3 climate penalties on NO_2, an O_3 precursor that is alterable through regulations on anthropogenic NO_x emissions. I analyze O_3-season (May–September) climate penalties within nine climate regions and 32 major urban areas across the contiguous U.S. in 1999–2001 and 2017–2019, with comparisons reflecting NO_x emissions differences in time and space. I describe variability in O_3 climate penalties as a function of NO_2, exploiting large NO_x emissions decreases from weekdays to weekends, which occur in absence of large changes in other aspects of O_3 chemistry, loss, and atmospheric transport. I demonstrate that the temperature dependence of PO_3 has been an important term affecting regional and urban O_3 climate penalties, with O_3 climate penalties responding to NO_x emissions decreases at higher NO_2 than O_3. Finally, I discuss the potential benefits of additional NO_x reductions on O_3 climate penalties in cities in 2015 O_3 National Ambient Air Quality Standard (NAAQS) nonattainment areas.

2.2 Methods

O_3 climate penalties ($m_{O3\text{-}T}$) are calculated as unweighted univariate linear regression slopes of the correlation between maximum daily 8-h average (MDA8) O_3 mixing ratios and daily maximum temperatures during the O_3 season, defined as May–September. MDA8 O_3 mixing ratios are obtained from the U.S. Environmental Protection Agency (EPA) Air Quality System (U.S. EPA Air Data, 2022). I include all monitors in the contiguous U.S. with MDA8 O_3 data on at least ten O_3-season days, either in both 1999–2001 and 2017–2019 or in at least one three-year period as indicated below. A total of 1286 monitors met these conditions in 1999–2001, 1320 monitors in 2017–2019, and 797 monitors in both periods. I remove days classified as exceptional events that

are excluded from NAAQS compliance determinations and keep days flagged as exceptional events by local air agencies but either not requested for exclusion or not concurred by the EPA. My results are largely insensitive to the exclusion or inclusion of either event type, although the number of exceptional event days is increasing. I use measurements of surface air temperature from the Automated Surface Observing System and Automated Weather Observing System, accessible through the Iowa State University Iowa Environmental Mesonet download service (Iowa Environmental Mesonet, 2022). I calculate the 8-h mean temperature over the same shifting daily time windows as MDA8 O_3 mixing ratios. O_3 and meteorological datasets are paired according to the minimum distance between two sites regardless of topography or other factors affecting local temperature, which adds noise to my results but is not likely to be a source of systematic error. I average site-level $m_{O3\text{-}T}$ and MDA8 O_3 over 1999–2001 and 2017–2019 on all days and separately on weekdays (Tuesday–Friday) and weekends (Saturday–Sunday). Mondays and Saturdays are considered transition days; as a result, I omit Mondays but retain Saturdays to improve weekend statistics. Data from July fourth holidays are also removed. When weekday and weekend $m_{O3\text{-}T}$ and MDA8 O_3 are compared, I require at least ten O_3-season days on both weekdays and weekends without restricting the analysis to monitors with observations in both periods. In 1999–2001 and 2017–2019, 1274 and 1315 monitors met these conditions, respectively. I focus on the nine NOAA U.S. climate regions in the contiguous U.S. and 32 major Metropolitan Statistical Areas (MSAs), including most MSAs in areas designated as in nonattainment for the 2015 O_3 NAAQS (Figure 2.1) (Karl and Koss, 1984; Simon et al., 2015).

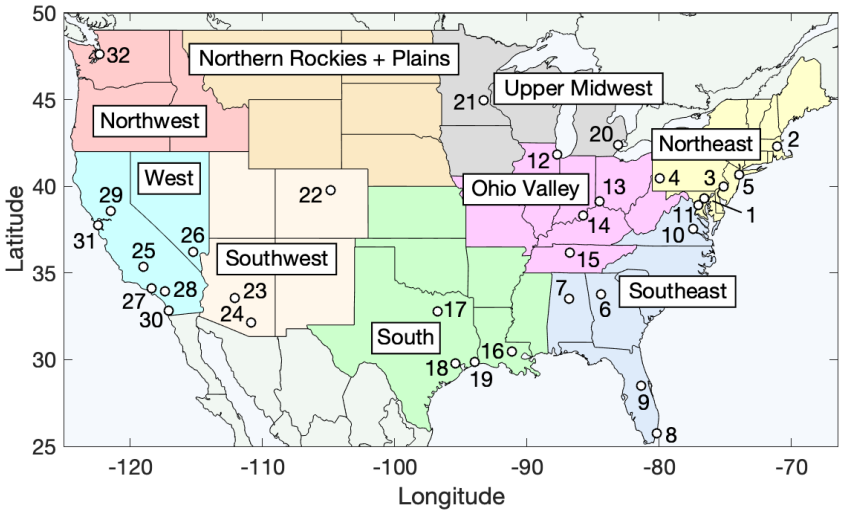

Figure 2.1. NOAA U.S. climate regions across the contiguous U.S.: Northeast (yellow), Southeast (blue), Ohio Valley (lilac), South (green), Upper Midwest (gray), Northern Rockies and Plains (pale orange), Southwest (peach), West (cyan), and Northwest (light red). MSAs are labeled numerically, corresponding to Table 2.1.

I use NO_2 tropospheric vertical column densities (TVCDs) measured by the TROPOspheric Monitoring Instrument (TROPOMI) onboard the sun-synchronous Copernicus Sentinel-5 Precursor satellite at ~1:30 pm local time (van Geffen et al., 2019; Veefkind et al., 2012). From 1 May 2018 to 6 August 2019, the nadir TROPOMI spatial resolution was 3.5 km x 7 km; subsequently, the nadir spatial resolution improved to 3.5 km x 5.5 km. I use Level 2 NO_2 TVCDs (qa value > 0.75) oversampled to 0.01º x 0.01º using a physics-based algorithm (Sun et al., 2018). I oversample O_3-season 2018–2019 TVCDs across the contiguous U.S. separately on weekdays (Tuesday–Friday) and weekends (Saturday–Sunday). I rely on 2018–2019 satellite NO_2 observations instead of surface measurements due to the limited number of surface nitrogen dioxide (NO_2*) monitors. Use of the term NO_2* acknowledges a positive interference from other nitrogen species (Dunlea et al., 2007), which has a larger effect on measurement accuracy than precision, with NO_2* data shown to be well suited for analyzing spatiotemporal trends (Russell et

al., 2010). Overhead NO_2 TVCDs are paired with O_3 measurements as the 0.01º x 0.01º grid containing the monitoring station. In the absence of 1999–2001 TROPOMI observations, and to help visualize $m_{O3\text{-}T}$ and MDA8 O_3 trends, I scale 2017–2018 NO_2 TVCDs by the ratio of 1999–2001 and 2017–2019 daytime (12–3 pm LT) surface NO_2*, averaged with each climate region, downloaded from the EPA Air Quality System. I note, observed weekday-weekend variability in $m_{O3\text{-}T}$ and MDA8 O_3 is independent of this NO_2 scaling, as are my conclusions.

2.3 Results and Discussion

2.3.1 Trends in $m_{O3\text{-}T}$, $r_{O3\text{-}T}$, and MDA8 O_3 across Variability in NO_2

I report changes in mean $m_{O3\text{-}T}$, Pearson correlation coefficients ($r_{O3\text{-}T}$), and MDA8 O_3 mixing ratios between 1999–2001 and 2017–2019 within nine NOAA climate regions and 32 MSAs (Figure 2.2; Table 2.1). These periods span substantial NO_x emissions decreases across the U.S. (Jiang et al., 2018), with 50–70% lower mean surface NO_2* in 2017–2019 than 1999–2001 in all climate regions except the Northern Rockies and Plains, where NO_2* fell by ~10%. I find statistically significant decreases in mean $m_{O3\text{-}T}$ in six of the nine climate regions between 1999–2001 and 2017–2019, the Northeast, Southeast, Ohio Valley, South, Upper Midwest, and West (Wilcoxon signed-rank test, a nonparametric test of paired samples). The largest decreases occurred in the Northeast, Southeast, and Ohio Valley, where mean $m_{O3\text{-}T}$ fell by >1 ppb $°C^{-1}$. There were smaller decreases in $m_{O3\text{-}T}$ in the South, Upper Midwest, and West (0.4–0.9 ppb $°C^{-1}$) and statistically insignificant changes in $m_{O3\text{-}T}$ in the Southwest and Northern Rockies and Plains. The Northwest is the only region to undergo significant, although small, increases in $m_{O3\text{-}T}$.

I report results for 32 MSAs (Table 2.1), where general patterns in urban-regional differences emerge, but with exceptions, and where mean urban $m_{O3\text{-}T}$ are both larger and smaller than on average across their lower-NO_2 regions. In the Northeast, Southeast, Ohio Valley, South, and Upper Midwest, urban $m_{O3\text{-}T}$ are often higher than regional mean $m_{O3\text{-}T}$, both in 1999–2001 and 2017–2019, with greater decreases in urban than regional $m_{O3\text{-}T}$ since 1999–2001 (e.g., New York City, Atlanta, and Houston). Several coastal MSAs exhibit lower mean $m_{O3\text{-}T}$ than their climate regions, e.g., Boston, Miami, Chicago, and San Diego, with thermally-driven flows known to distribute O_3 and other pollutants away from coastal cities (Geddes et al., 2021; Graney et al., 2004; Harris and Kotamarthi, 2005). In the Southwest, West, and Northwest, there is no clear tendency for higher urban than regional $m_{O3\text{-}T}$, and, in many MSAs, changes in $m_{O3\text{-}T}$ since 1999–2001 are insignificant. In Denver, Sacramento, and Bakersfield, $m_{O3\text{-}T}$ are higher on average than in their respective regions, with significant decreases in $m_{O3\text{-}T}$ since 1999–2001. In Phoenix, Los Angeles, Riverside, and Seattle, $m_{O3\text{-}T}$ either did not change or increased since 1999–2001.

Changes in $r_{O3\text{-}T}$ and MDA8 O_3 between 1999–2001 and 2017–2019, and differences between MSAs and regions, echo $m_{O3\text{-}T}$ trends (Figure 2.2; Table 2.1). Weakened or strengthened $r_{O3\text{-}T}$ since 1999–2001 are strongly correlated with decreased or increased $m_{O3\text{-}T}$, respectively (Figure 2.S1) demonstrating that O_3 is more temperature sensitive under high temperature conditions. In the Northeast, Southeast, Ohio Valley, South, and Upper Midwest, climate regions with the largest declines in $m_{O3\text{-}T}$, I observe significant reductions in $r_{O3\text{-}T}$, stronger urban than regional $r_{O3\text{-}T}$ (e.g., Atlanta), and regional decreases in MDA8 O_3 of 5–11 ppb (10–25%). In the Southwest, West, and Northwest, $r_{O3\text{-}T}$ increased since 1999–2001, especially in the Northwest and, for example, Los Angeles, Riverside, and Phoenix. In these regions, as well as in the Northern Rockies and Plains, decreases in MDA8 O_3 between 1999–2001 and 2017–2019 were small or statistically

insignificant. Overall, regional and MSA-level $m_{O3\text{-}T}$ are weakly or uncorrelated with MDA8 O_3 in both periods, with differences across all monitors moderately associated, suggesting high O_3 is not always temperature sensitive (Figure 2.S1). That said, changes in $m_{O3\text{-}T}$ and MDA8 O_3 between 1999–2001 and 2017–2019 are strongly correlated regionally (r = 0.97) and within MSAs (r = 0.72), although correlated more moderately at the monitor level (r = 0.60), indicating intraregional and intraurban variability in the relationships in the trends in $m_{O3\text{-}T}$ and MDA8 O_3 (Figure 2.S2).

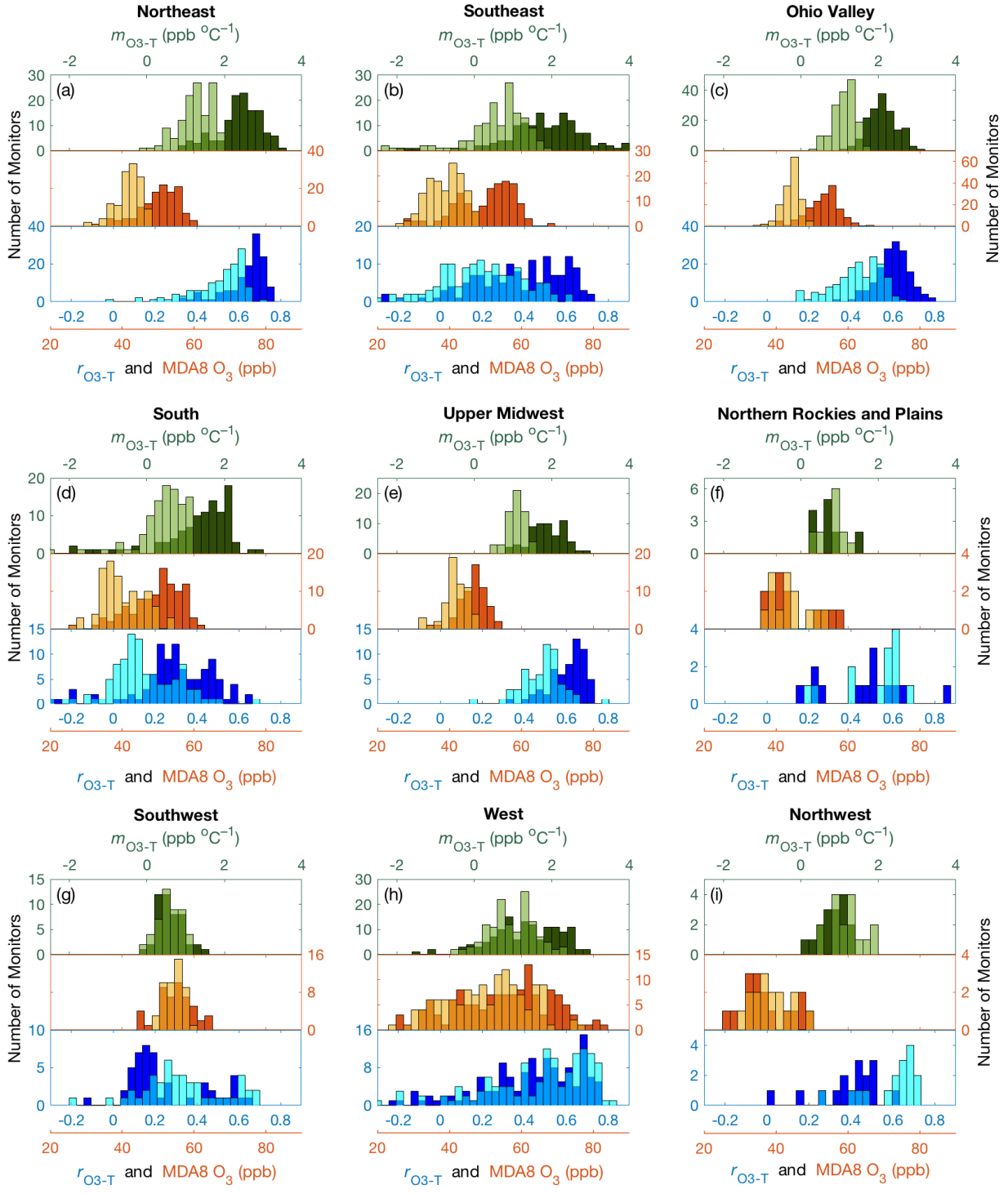

Figure 2.2. Mean O_3-season (May–September) $m_{O3\text{-}T}$ (top), MDA8 O_3 (middle), and $r_{O3\text{-}T}$ (bottom) at each O_3 monitoring station with measurements in both 1999–2001 (dark green, orange, and blue, respectively) and 2017–2017 (light green, gold, and cyan, respectively) in the nine NOAA climate regions: Northeast (a), Southeast (b), Ohio Valley (c), South (d), Upper Midwest (e), Northern Rockies and Plains (f), Southwest (g), West (h), and Northwest (i).

Table 2.1. O_3-season mean $m_{O3\text{-}T}$ (ppb °C^{-1}) with mean slope errors, $r_{O3\text{-}T}$, and MDA8 O_3 (ppb) at *N* monitoring stations with measurements in both 1999–2001 and 2017–2019 in nine climate regions and 32 MSAs. Variability as 1 standard deviation is represented parenthetically. Statistical significance for differences in 1999–2001 and 2017–2019 is based on the Wilcoxon signed-rank test (regions; $p < 0.01$) and 1999–2001 and 2017–2019 mean errors added in quadrature (MSAs) and indicated as * in 2017–2019.

		$m_{O3\text{-}T}$ (ppb °C^{-1})	$r_{O3\text{-}T}$	MDA8 O_3 (ppb)	$m_{O3\text{-}T}$ (ppb °C^{-1})	$r_{O3\text{-}T}$	MDA8 O_3 (ppb)	*N*
			1999–2001			2017–2019		
Northeast		**2.4 ± 0.2 (0.6)**	**0.64 (0.1)**	**50.3 (5.5)**	**1.3 ± 0.2 (0.4)***	**0.51 (0.13)***	**41.8 (3.6)***	**127**
1	Baltimore-Columbia-Towson, MD	2.6 ± 0.1 (0.1)	0.65 (0.1)	55.3 (2.3)	1.7 ± 0.1 (0.2)*	0.61 (0.1)*	46.6 (0.7)*	5
2	Boston-Cambridge-Newton, MA	1.8 ± 0.1 (0.3)	0.60 (0.1)	38.4 (9.3)	1.1 ± 0.1 (0.1)*	0.57 (0.1)	38.9 (2.2)	2
3	Philadelphia-Camden-Wilmington, PA-NJ-DE-MD	3.0 ± 0.1 (0.3)	0.71 (0.1)	52.7 (5.6)	1.7 ± 0.1 (0.2)*	0.59 (0.1)*	44.6 (1.1)*	12
4	Pittsburg, PA	2.7 ± 0.1 (0.2)	0.70 (0.1)	53.6 (1.9)	1.4 ± 0.1 (0.2)*	0.53 (0.1)*	44.7 (1.8)*	10
5	New York-Newark-Jersey City, NY-NJ-PA	2.7 ± 0.1 (0.4)	0.68 (0.1)	49.7 (4.7)	1.5 ± 0.1 (0.3)*	0.58 (0.1)*	42.0 (2.5)*	17
Southeast		**1.8 ± 0.4 (1.1)**	**0.37 (0.2)**	**50.0 (8.0)**	**0.6 ± 0.3 (0.8)***	**0.19 (0.2)***	**38.9 (4.7)***	**138**
6	Atlanta, GA	3.3 ± 0.1 (0.7)	0.55 (0.1)	58.4 (2.3)	1.2 ± 0.1 (0.4)*	0.29 (0.1)*	42.0 (3.1)*	10
7	Birmingham-Hoover, AL	2.5 ± 0.1 (0.4)	0.47 (0.1)	52.0 (3.1)	1.1 ± 0.1 (0.2)*	0.28 (0.1)*	41.1 (2.0)*	8
8	Miami, FL	–1.9 ± 0.3 (0.5)	–0.26 (0.1)	30.0 (1.8)	–1.4 ± 0.2 (0.5)*	–0.24 (0.1)*	28.8 (1.2)	4
9	Orlando-Kissimmee-Sanford, FL	1.6 ± 0.2 (0.4)	0.25 (0.1)	43.0 (0.9)	0.7 ± 0.2 (0.3)*	0.13 (0.1)*	35.3 (1.5)*	5
10	Richmond, VA	2.4 ± 0.1 (0.2)	0.62 (0.1)	54.2 (0.5)	1.1 ± 0.1 (0.3)*	0.43 (0.1)*	41.5 (2.1)*	5
11	Washington-Arlington-Alexandria, DC-VA-MD-WV	2.6 ± 0.1 (0.4)	0.67 (0.1)	53.6 (1.5)	1.3 ± 0.1 (0.3)*	0.51 (0.1)*	42.7 (3.4)*	6
Ohio Valley		**2.1 ± 0.2 (0.4)**	**0.6 (0.1)**	**53.0 (4.7)**	**1.1 ± 0.2 (0.3)***	**0.43 (0.1)***	**44.2 (2.4)***	**159**
12	Chicago-Naperville-Elgin, IL-IN-WI	1.9 ± 0.1 (0.3)	0.64 (0.1)	45.2 (3.9)	1.2 ± 0.1 (0.2)*	0.53 (0.1)*	45.2 (1.8)	15
13	Cincinnati, OH-KY-IN	2.4 ± 0.1 (0.2)	0.62 (0.1)	53.1 (1.8)	1.5 ± 0.1 (0.2)*	0.54 (0.1)*	46.7 (2.2)*	6
14	Louisville-Jefferson County, KY-IN	2.5 ± 0.1 (0.2)	0.63 (0.1)	56.3 (2.9)	1.4 ± 0.1 (0.2)*	0.47 (0.1)*	44.4 (0.6)*	5
15	Nashville-Davidson-Murfreesboro-Franklin, TN	2.2 ± 0.1 (0.3)	0.52 (0.1)	56.5 (4.7)	1.2 ± 0.1 (0.3)*	0.37 (0.1)*	43.1 (1.8)*	5
South		**1.3 ± 0.4 (0.9)**	**0.29 (0.2)**	**49.5 (7.0)**	**0.5 ± 0.3 (0.6)***	**0.14 (0.2)***	**40.2 (5.8)***	**100**
16	Baton Rouge, LA	1.9 ± 0.2 (0.4)	0.27 (0.1)	48.4 (2.4)	0.6 ± 0.2 (0.3)*	0.08 (0.1)*	36.9 (0.8)*	9
17	Dallas-Fort Worth-Arlington, TX	1.5 ± 0.1 (0.6)	0.37 (0.1)	55.4 (3.9)	0.6 ± 0.1 (0.3)*	0.18 (0.1)*	45.0 (2.7)*	14
18	Houston-The Woodlands-Sugar Land, TX	1.5 ± 0.2(1.1)	0.20 (0.2)	45.6 (4.5)	0.2 ± 0.1 (0.5)*	0.04 (0.1)*	36.5 (2.6)*	14
19	Beaumont-Port Arthur, LA	1.8 ± 0.2 (0.4)	0.27 (0.1)	41.1 (1.9)	0.3 ± 0.2 (0.2)*	0.05 (0.1)*	34.9 (0.8)*	6
Upper Midwest		**1.9 ± 0.2 (0.5)**	**0.61 (0.1)**	**46.6 (3.7)**	**1.1 ± 0.2 (0.2)***	**0.49 (0.1)***	**41.7 (3.3)***	**59**
20	Detroit-Warren-Dearborn, MI	2.4 ± 0.1 (0.1)	0.66 (0.1)	46.3 (2.7)	1.5 ± 0.1 (0.1)*	0.60 (0.1)*	43.9 (2.1)*	6
21	Minneapolis-St. Paul-Bloomington, MN	1.5 ± 0.1 (0.1)	0.63 (0.1)	42.5 (1.4)	1.1 ± 0.1 (0.3)*	0.51 (0.1)*	36.4 (3.9)*	3
Northern Rockies Plains		**0.7 ± 0.1 (0.4)**	**0.46 (0.2)**	**44.4 (7.5)**	**0.8 ± 0.1 (0.3)**	**0.51 (0.2)**	**43.5 (5.4)**	**13**
Southwest		**0.6 ± 0.2 (0.3)**	**0.25 (0.2)**	**55.0 (4.7)**	**0.6 ± 0.2 (0.3)**	**0.33 (0.2)***	**54.4 (2.6)**	**48**
22	Denver-Aurora-Lakewood, CO	1.2 ± 0.1 (0.2)	0.58 (0.1)	50.8 (5.5)	0.9 ± 0.1 (0.1)*	0.63 (0.1)*	55.6 (3.4)*	5
23	Phoenix-Mesa-Scottsdale, AZ	0.5 ± 0.1 (0.2)	0.14 (0.1)	59.1 (3.8)	0.4 ± 0.1 (0.2)	0.21 (0.1)*	54.6 (3.1)*	13
24	Tucson, AZ	0.4 ± 0.1 (0.1)	0.11 (0.1)	52.7 (0.8)	0.4 ± 0.1 (0.1)	0.19 (0.1)*	51.9 (0.7)*	5
West		**1.3 ± 0.2 (0.9)**	**0.42 (0.2)**	**55.1 (13.2)**	**1.0 ± 0.1 (0.6)***	**0.47 (0.2)***	**50.6 (11.3)***	**133**
25	Bakersfield, CA	1.9 ± 0.1 (0.6)	0.60 (0.1)	71.1 (5.2)	1.4 ± 0.1 (0.2)*	0.71 (0.1)*	62.9 (2.5)*	6
26	Las Vegas, NV	0.8 ± 0.1 (0.3)	0.31 (0.1)	60.3 (2.1)	0.5 ± 0.1 (0.1)*	0.31 (0.1)	55.8 (1.7)*	8
27	Los Angeles-Long Beach-Anaheim, CA	1.0 ± 0.1 (1.2)	0.24 (0.3)	49.8 (7.1)	1.1 ± 0.1 (0.4)	0.45 (0.2)*	52.0 (8.3)*	8
28	Riverside-San Bernardino-Ontario, CA	1.5 ± 0.1 (0.5)	0.40 (0.1)	68.3 (5.8)	1.5 ± 0.1 (0.5)	0.62 (0.1)*	66.1 (5.4)*	17
29	Sacramento-Roseville-Arden-Arcade, CA	2.1 ± 0.1 (0.5)	0.67 (0.1)	56.8 (5.9)	1.2 ± 0.1 (0.3)*	0.62 (0.1)*	50.5 (3.8)*	13
30	San Diego-Carlsbad, CA	–0.4 ± 0.2 (1.6)	–0.03 (0.4)	53.2 (10.6)	0.1 ± 0.1 (1.0)*	0.03 (0.5)	45.9 (11.1)*	3
31	San Francisco-Oakland-Hayward, CA	1.2 ± 0.1 (0.8)	0.45 (0.3)	34.4 (8.9)	0.7 ± 0.1 (0.5)*	0.35 (0.3)*	35.6 (6.3)	7
Northwest		**0.8 ± 0.2 (0.4)**	**0.40 (0.2)**	**37.4 (7.0)**	**1.2 ± 0.1 (0.4)***	**0.59 (0.1)***	**38.6 (5.2)**	**16**
32	Seattle	0.9 ± 0.1 (0.5)	0.34 (0.2)	33.4 (6.7)	1.4 ± 0.1 (0.7)*	0.56 (0.2)*	36.1 (3.8)*	5

2.3.2 The NO_2 Dependence of $m_{O3\text{-}T}$ and MDA8 O_3

Trends in $m_{O3\text{-}T}$ between 1999–2001 and 2017–2019 and within MSAs and their climate regions do not demonstrate linear relationships with NO_2 (Figure 2.2; Table 2.1); however, when $m_{O3\text{-}T}$ varies functionally with NO_2, its NO_2 dependence is driven by that of PO_3, which is nonlinear with NO_2 (Figure 2.3) (Pusede et al., 2015). In brief, PO_3 responds positively and proportionally to increases in NO_2 under low NO_x conditions, with NO being the limiting reagent in O_3-forming HO_x ($\equiv$ OH + HO_2 + RO_2) radical cycling. Under high NO_x conditions, PO_3 responds inversely proportionally to increases in NO_2, as NO_2 combines with OH to produce nitric acid, reducing O_3-forming OH reactions with VOCs. At low NO_x, PO_3 is largely insensitive to changes in VOCs, and, at high NO_x levels, additional VOC emissions increase PO_3. PO_3 maximizes at intermediate NO_x, with peak PO_3 shifting to higher NO_2 concentrations at higher VOC levels. Knowledge of the NO_2 abundance at the transition between NO_x-limited and NO_x-suppressed PO_3 regimes is critical for regulating O_3 air quality, as NO_x and VOC controls are most effective in the PO_3 regime in which they are limiting.

PO_3 is also a nonlinear function of temperature, and this temperature dependence varies with NO_2; therefore, when PO_3 dominates the O_3 mass balance, $m_{O3\text{-}T}$ also depends on NO_x (Pusede et al., 2015; Rasmussen et al., 2013). While bimolecular reaction rates increase on hot days (Aw and Kleeman, 2003; Sillman and Samson, 1995), surface-level PO_3 is more strongly influenced by the temperature dependence of the absolute and proportional abundance of NO_x, VOCs reactive with OH, and HO_x radicals (Pusede et al., 2015; Sillman and Samson, 1995). Temperature-dependent NO_x emission sources, which positively affect NO_x-limited PO_3, include soils (Romer et al., 2018), electricity generation from increased air conditioning demand (He et al., 2013), and thermal

decomposition of peroxy acyl nitrates (Sillman and Samson, 1995; Steiner et al., 2006). Many VOCs are emitted as an exponential function of temperature (Di Carlo et al., 2004; Guenther et al., 2006; Pusede et al., 2014), and tropospheric concentrations of HO_x precursors, in particular, O_3, water vapor, and HCHO, are elevated on high temperature days. Temperature-driven changes in VOCs and HO_x have their largest effects when PO_3 is more NO_x suppressed, with temperature shown to behave as a proxy for OH-reactive VOCs in polluted locations (Abeleira and Farmer, 2017; de Foy et al., 2020; Nussbaumer and Cohen, 2020; Pollack et al., 2021; Pusede and Cohen, 2012). Because of differences in overall NO_x, VOCs, and HO_x temperature sensitivities, higher $m_{O3\text{-}T}$ result from NO_x-suppressed PO_3 (Bloomer et al., 2009; Ito et al., 2009; Nussbaumer and Cohen, 2020; Pusede and Cohen, 2012; Pusede et al., 2014; Pusede et al., 2015; Rasmussen et al., 2012; Rasmussen et al., 2013; Steiner et al., 2010), but under very high NO_x conditions, NO titration of O_3 can push $m_{O3\text{-}T}$ to zero (Rasmussen et al., 2013).

In a novel application of the classic PO_3 isopleth (Haagen-Smit and Fox, 1954; Seinfeld, 1991), which simultaneously represents PO_3 as a function of both NO_x and VOCs, Rasmussen et al. (2013) described O_3 climate penalties in NO_x and VOC emissions space. Modeled climate penalties, which the authors defined as the simulated O_3 response to a temperature perturbation, exhibited a similar functional form as PO_3 but peaked at higher NO_x levels than the corresponding PO_3. This occurrence of peak $m_{O3\text{-}T}$ at higher NO_2 than PO_3 is a consequence of the NO_2 dependence of the effects of temperature-driven changes in VOCs and HO_x precursors, including peroxy nitrate thermal decomposition. In Figure 2.3, I show differences in PO_3 versus NO_2 due to changes in VOC reactivity to OH calculated using an analytical model (*SI Appendix*) (Farmer and Cohen, 2008; Murphy et al., 2007; Pusede et al., 2014). In the scenario that PO_3 drives O_3 variability and VOC emissions are temperature dependent, the difference between PO_3 curves, i.e.,

PO_3 under two different VOC conditions, would approximate a major portion of the NO_2 dependence of $m_{O3\text{-}T}$ (Figure 2.3a). Connecting the difference in PO_3 under two VOC reactivity conditions to $m_{O3\text{-}T}$ requires the temperature change driving the VOC change. So defined, the largest $m_{O3\text{-}T}$ would occur at 50–65% higher NO_2 than peak PO_3, with greater differences at higher NO_2 levels, as based on PO_3 curves at the mean of the two VOC reactivity conditions over 1–20 ppb NO_x. If temperature increases HO_x radical production with VOCs remaining constant, the peak change in PO_3 occurs at 20% higher NO_2 than peak PO_3. As a result, NO_x control is an effective O_3 climate adaptation strategy at markedly higher NO_2 levels than peak PO_3 where this NO_2 dependence is manifest.

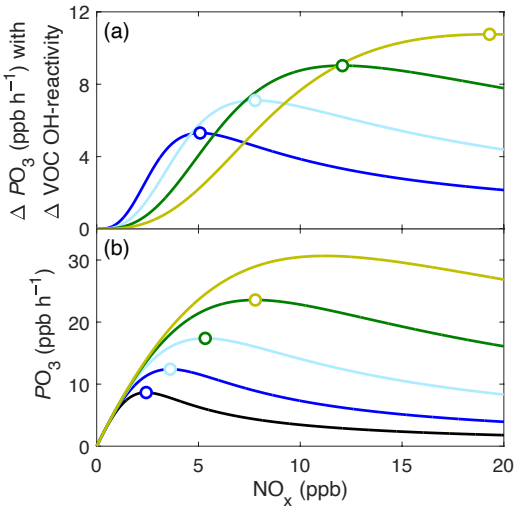

Figure 2.3. Differences between PO_3 curves as function of NO_x at five VOC reactivity levels (a). PO_3 as a function of NO_x under five VOC reactivity levels that increase exponentially: lowest (black), low (blue), intermediate (light blue), high (green), and highest (yellow-green). For example, the green curve in panel a is the difference between the green and light blue PO_3 curves in panel b. Circles are the peak change in PO_3 and PO_3, with the difference based on the increase in PO_3 from the lower VOC level (same color circle).

To observe regional variability in the NO_2 dependence of $m_{O3\text{-}T}$, I employ an empirical approach developed by Pusede and Cohen (2012) and applied by others (Abeleira and Farmer, 2017; de Foy

et al., 2020; Nussbaumer and Cohen, 2020; Pollack et al., 2021) to describe $m_{O3\text{-}T}$ and MDA8 O_3 as a function of NO_2, tethering weekday observations with their corresponding values on weekends (Figure 2.4). NO_2 concentrations are typically higher on weekdays than weekends because of patterns in commercial heavy-duty diesel truck traffic in U.S. cities (Marr and Harley, 2002; Russell et al., 2012). While weekday-weekend NO_2 differences are diminishing (Demetillo et al., 2019), in part because of improved diesel fleet NO_x emissions control (Schwarzman et al., 2021), they remain sizable in many locations. Diesel engines are not major sources of VOCs reactive with OH, and conditions affecting O_3 loss and transport are weekday-weekend independent with sufficient time averaging. As a result, there is an established practice of analyzing O_3 differences on weekdays and weekends to understand PO_3 chemistry (Buysse et al., 2018; Demetillo et al., 2019; Murphy et al., 2006a; Murphy et al., 2007; Pollack et al., 2012; Stephens et al., 2008). By tethering weekday-weekend conjugates, observations trace individual VOC reactivity curves in Figure 2.3, revealing spatiotemporal trends in the NO_2 dependence of $m_{O3\text{-}T}$ and MDA8 O_3, rather than their mere covariance, under conditions when PO_3 is a major term affecting O_3 variability (Pusede and Cohen, 2012).

Viewed together, $m_{O3\text{-}T}$ variations with NO_2 in 1999–2001 and 2017–2019 broadly reflect O_3-NO_x chemical relationships presented in Figure 2.3 in most climate regions. I average the large number of regional observations into equally spaced weekday NO_2 bins (0.3 x 10^{15} molecules cm^{-2}) and tether mean weekday $m_{O3\text{-}T}$ and MDA8 O_3 to mean values from corresponding monitors on weekends. While NO_2 TVCDs in 1999–2001 are scaled as described in the Methods, the observed weekday-weekend differences in $m_{O3\text{-}T}$ and MDA8 O_3 are independent of this scaling, and generally, although not always, reinforce its suitability for visualizing $m_{O3\text{-}T}$ and MDA8 O_3 NO_2 sensitivities. There are two key observations in Figure 2.4: (1) the derivatives of tethered weekday-

weekend $m_{O3\text{-}T}$ and MDA8 O_3 follow the overall NO_2 dependence in Figure 2.3 in most regions, and (2) $m_{O3\text{-}T}$ values respond positively and proportionally to increases in NO_2 concentrations at higher NO_2 levels than MDA8 O_3. The results demonstrate that the temperature dependence of local PO_3 as a function of NO_2 has been an important control over $m_{O3\text{-}T}$ and MDA8 O_3 on average in seven of the nine climate regions, exceptions being the Northern Rockies and Plains and Northwest.

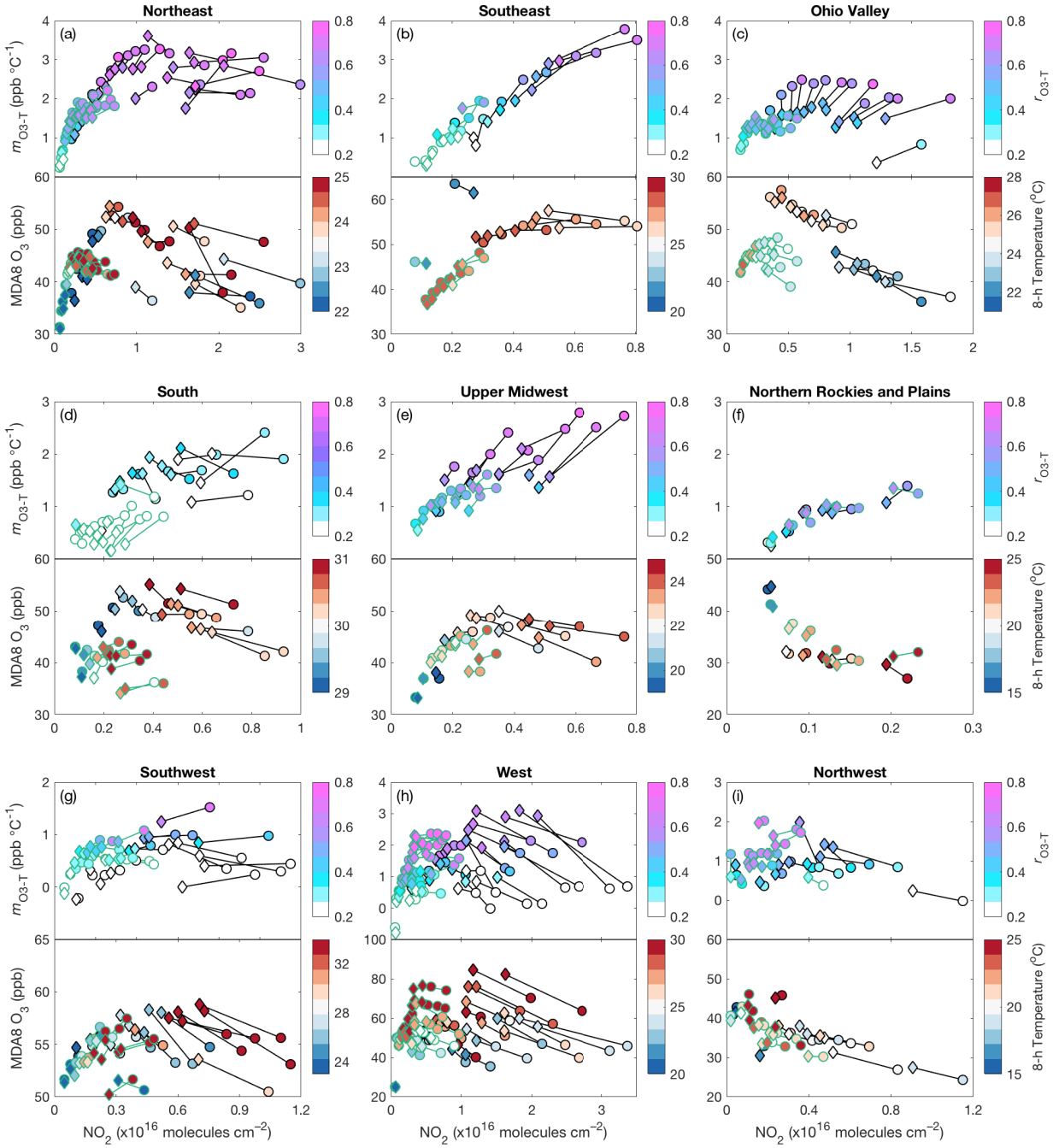

Figure 2.4. Weekday (circles) and weekend (diamonds) $m_{O3\text{-}T}$ (ppb $^{o}C^{-1}$) (top) and MDA8 O_3 (ppb) (bottom) versus NO_2 TVCDs (molecules cm^{-2}) colored by $r_{O3\text{-}T}$ and 8-h average daily temperature, respectively, in nine NOAA climate regions: Northeast (a), Southeast (b), Ohio Valley (c), South (d), Upper Midwest (e), Northern Rockies and Plains (f), Southwest (g), West (h), and Northwest (i). Weekday observations are binned every 0.3 x 10^{15} molecules cm^{-2} NO_2 and tethered to their corresponding means on weekends. Data in 1999–2001 are outlined in black and data in 2017–2019 are outlined in green. To support visualization only, NO_2 TVCDs in 1999–2001 are estimated by scaling 2018–2019 NO_2 TVCDs according to surface NO_2* mixing ratios in both periods.

In the Northeast, Southeast, Ohio Valley, South, and Upper Midwest, regions that saw the greatest decreases in $m_{O3\text{-}T}$ between 1999–2001 and 2017–2019, $m_{O3\text{-}T}$ have and continue to positively vary with NO_2 and/or were/are at a peak with respect to NO_2 (Figure 2.4). Weekday-weekend $m_{O3\text{-}T}$ and MDA8 O_3 differences largely trace the NO_2 relationships depicted in Figure 2.3, with $m_{O3\text{-}T}$ being responsive to NO_x emission controls at higher NO_2 than MDA8 O_3. While there is scatter in the observations and evidence of inadequacies in the NO_2 scaling approach, particularly in the Ohio Valley in 1999–2001, PO_3 relationships with NO_2 are broadly apparent in $m_{O3\text{-}T}$ and MDA8 O_3 trends. Observed scatter is in part a feature of the regional averaging, which combines measurements in urban, suburban, and rural locations and cities with potentially very different atmospheric compositions. I see PO_3 in 1999–2001 was largely NO_x-suppressed at higher NO_2 levels in these regions, except in the Southeast, where weekday-weekend differences in MDA8 O_3 indicate chemistry was near peak PO_3. The MDA8 O_3 outliers in the Southeast are data collected at Great Smokey Mountain National Park.

In the Southwest and West, where smaller or insignificant decreases in $m_{O3\text{-}T}$ were observed between 1999–2001 and 2017–2019, PO_3 chemistry was and continues to be more NO_x-suppressed than in other regions, with higher $m_{O3\text{-}T}$ and MDA8 O_3 at higher temperatures. In 1999–2001, $m_{O3\text{-}T}$ was inversely proportional to NO_2 (this is most pronounced in the West) and near a peak with respect to NO_2 in 2017–2019, with evidence of continued NO_x-suppressed or peak PO_3 in many locations in the West and a transition to NO_x-limited PO_3 in the Southwest. Here, I see $m_{O3\text{-}T}$ has been responsive to NO_2 reductions; however, because the chemistry is nonlinear, these changes were not apparent when simply comparing 1999–2001 and 2017–2019 mean and $m_{O3\text{-}T}$ distributions (Figure 2.2; Table 2.1). In the West, I find NO_2 levels at peak $m_{O3\text{-}T}$ are closer to those at peak MDA8 O_3 than in other regions. Many of these high-NO_2 observations are in the Los

Angeles and Riverside MSAs, where recent work has shown $P\mathrm{O_3}$ trends over the last two decades followed $\mathrm{HO_x}$ trends (Perdigones et al., 2022). As described above (Figure 2.3), if $m_{\mathrm{O3\text{-}T}}$ is driven by temperature-dependent $\mathrm{HO_x}$ radical production, $m_{\mathrm{O3\text{-}T}}$ transitions to $\mathrm{NO_2}$ sensitivity at $\mathrm{NO_2}$ concentrations more similar to the $\mathrm{NO_2}$ levels when $P\mathrm{O_3}$ transitions to $\mathrm{NO_x}$-limited chemistry. When I remove measurements from the Los Angeles and Riverside MSAs from the regional mean, I observe relative trends in $m_{\mathrm{O3\text{-}T}}$ and MDA8 $\mathrm{O_3}$ with $\mathrm{NO_2}$ more akin to those in Figures 2.3a–b (Figure 2.S3).

In each of these regions, the Northeast, Southeast, Ohio Valley, South, Upper Midwest, West, and Southwest, I find lower $r_{\mathrm{O3\text{-}T}}$ with smaller $m_{\mathrm{O3\text{-}T}}$, largely independent of $\mathrm{NO_2}$; see, for example, the Southwest and West. When $m_{\mathrm{O3\text{-}T}} < 1$ ppb $^{\circ}\mathrm{C}^{-1}$, $r_{\mathrm{O3\text{-}T}}$ are typically less than 0.3. At the lowest $\mathrm{NO_2}$ levels, $\mathrm{NO_2}$ is often similar on weekdays and weekends such that the $\mathrm{NO_2}$ dependence of local $P\mathrm{O_3}$ is not independently tested; although, $m_{\mathrm{O3\text{-}T}}$ and MDA8 $\mathrm{O_3}$ under low-$\mathrm{NO_2}$ conditions follow relationships with $\mathrm{NO_2}$ more broadly. Finally, MDA8 $\mathrm{O_3}$ variability with temperature in these regions reflects that higher temperatures often lead to higher levels of $\mathrm{O_3}$-forming VOCs and/or $\mathrm{HO_x}$ and that weekday-weekend tethers generally trace individual VOC reactivity and/or $\mathrm{HO_x}$ production rate $P\mathrm{O_3}$ curves (Pusede and Cohen, 2012).

In the Northern Rockies and Plains and Northwest regions, $m_{\mathrm{O3\text{-}T}}$ and MDA8 $\mathrm{O_3}$ relationships with $\mathrm{NO_2}$ do not predominantly reflect those in Figure 2.3. A body of literature has linked $\mathrm{O_3}$ air pollution and wildfires in the western U.S., with $\mathrm{O_3}$ mixing ratios being well correlated with area burned and biomass consumed (Jaffe et al., 2008; Jaffe and Wigder, 2012) and climate change increasing wildfire frequency and severity (Spracklen et al., 2009). Wildfires influence surface $\mathrm{O_3}$ and its precursors (Buysse et al., 2019; Jaffe, 2011; Pfister et al., 2008) and fire activity is enhanced

on hot summer days (Westerling et al., 2003). In the Northern Rockies and Plains, there are no populous MSAs, and NO_2 TVCDs are substantially lower than in other regions. The largest increases in MDA8 O_3 since 1999–2001 have occurred at both the lowest $m_{O3\text{-}T}$ and NO_2. In the Northwest, there is evidence for NO_x-suppressed PO_3 affecting $m_{O3\text{-}T}$ and MDA8 O_3 at higher NO_2 (> 2 x 10^{15} molecules cm^{-2}) and correspondingly more NO_2-sensitive $m_{O3\text{-}T}$. Measurements collected under moderate and higher NO_2 conditions are largely from the Seattle MSA (note the colder temperatures).

2.3.3 Continued O_3 Climate Adaptation through NO_x Control in Cities

Here, I explore whether additional NO_x reductions would lower $m_{O3\text{-}T}$, focusing on MSAs with Marginal to Extreme 2015 O_3 NAAQS nonattainment designations (U.S. EPA Green Book, 2022). MSA-level $m_{O3\text{-}T}$, MDA8 O_3, and NO_2 relationships are likewise explained in large part in terms of O_3-NO_x chemical relationships in Figure 2.3 and reveal opportunities for further NO_x-driven reductions in $m_{O3\text{-}T}$ (Figures 2.5 and 2.S4). To facilitate discussion, I report 2017–2019 mean and maximum weekday-weekend differences in $m_{O3\text{-}T}$ across monitors in a given MSA where weekday-weekend NO_x emissions patterns provide a constraint on the NO_2 dependence of PO_3, specifically where NO_2 is lower on weekends than weekdays by at least 0.1 x 10^{15} molecules cm^{-2} (Table 2.S1). This same constraint is placed on Figures 2.5 and 2.S4 (but not Figure 2.4). Because weekend NO_2 reductions vary between cities, in the text, I normalize weekday-weekend differences in $m_{O3\text{-}T}$ by the corresponding NO_2 change. Weekday-weekend $m_{O3\text{-}T}$ declines reflect the efficacy of NO_x emissions controls when $m_{O3\text{-}T}$ are NO_2 sensitive, with results potentially underestimating NO_x reduction benefits in high-NO_2 (NO_x suppressed) cities and requiring knowledge of nonlinear NO_2 relationships.

In New York–Newark, Philadelphia, Washington, D.C., Atlanta, and Houston, as well as the other MSAs in their respective regions with nonattainment designations listed in Table 2.1, Baltimore and Dallas, weekday $m_{O3\text{-}T}$ are sensitive to further NO_2 reductions (Figures 2.5 and 2.S4). Mean and maximum weekend $m_{O3\text{-}T}$ decreases are 0.7 ± 0.7 (1σ) ppb °C^{-1} and 0.3–4.4 ppb °C^{-1} per unit 10^{15} molecules NO_2 cm^{-2}, respectively, corresponding to 22 ± 7% (1σ) lower weekend NO_2 TVCDs. Not all MSAs in nonattainment areas in the Ohio Valley and Upper Midwest listed in Table 2.1 have $m_{O3\text{-}T}$ that are currently on average NO_2 sensitive, suggesting benefits of NO_x emissions reductions will be slower to appear. In Detroit, 2017–2019 mean and maximum weekend $m_{O3\text{-}T}$ reductions are 0.5 ppb °C^{-1} and 0.9 ppb °C^{-1} per unit 10^{15} molecules NO_2 cm^{-2}, respectively. However, in Chicago and Cincinnati, mean weekend $m_{O3\text{-}T}$ decreases are negligible, while maximum weekend $m_{O3\text{-}T}$ decreases are 0.3–0.4 ppb °C^{-1} per unit 10^{15} molecules NO_2 cm^{-2}. In Louisville, mean and maximum weekend $m_{O3\text{-}T}$ differences are negative and negligible, respectively, meaning chemistry at the monitors in these MSAs continues to be NO_x suppressed.

California is home to the only MSAs in the U.S. with Serious, Severe 15, and Extreme 2015 O_3 NAAQS nonattainment designations. In Los Angeles and Riverside, $m_{O3\text{-}T}$ peaks at NO_2 concentrations similar to MDA8 O_3 mixing ratios, which, as described above, suggests temperature-dependent production of HO_x radicals is an important factor determining the NO_2 dependence of $m_{O3\text{-}T}$ (Perdigones et al., 2022). Mean 2017–2019 weekday-weekend $m_{O3\text{-}T}$ differences are near zero; however, $m_{O3\text{-}T}$ is at peak with respect to NO_2 (Figure 2.5). The 2017–2019 average maximum weekend $m_{O3\text{-}T}$ reduction is 1.2 ppb °C^{-1} per unit 10^{15} molecules NO_2 cm^{-2}, indicating there are O_3 climate adaption benefits with further NO_x control, at least at some monitoring locations. PO_3 in Bakersfield, Sacramento, and San Francisco is largely NO_x limited (Figure 2.S4), with mean and maximum weekday-weekend $m_{O3\text{-}T}$ decreases of 1.0 ± 0.5 (1σ) ppb

$°C^{-1}$ and 1.4–2.5 ppb $°C^{-1}$ per unit 10^{15} molecules NO_2 cm^{-2}, respectively, and, while mean weekday-weekend $m_{O3\text{-}T}$ changes in San Diego are negative, maximum decreases are 0.8 ppb $°C^{-1}$ per 10^{15} molecules NO_2 cm^{-2}. In Phoenix, I find $m_{O3\text{-}T}$ is, and has been, largely independent of NO_2, while MDA8 O_3 follows an NO_2 response similar to PO_3. Here, $m_{O3\text{-}T}$ are and have been <1 ppb $°C^{-1}$ since 1999–2001, lacking the NO_2 relationships in Figure 2.3a in accordance with a limited role for temperature-dependent VOCs in a desert location. Finally, like the other MSAs, there are potential O_3 climate adaptation benefits in Denver and Las Vegas (Figure 2.S4), where mean and 2017–2019 average maximum weekday-weekend $m_{O3\text{-}T}$ decreases are 0.5 ± 0.1 (1σ) ppb $°C^{-1}$ and 1.6–2.0 ppb $°C^{-1}$ per unit 10^{15} molecules NO_2 cm^{-2}, respectively.

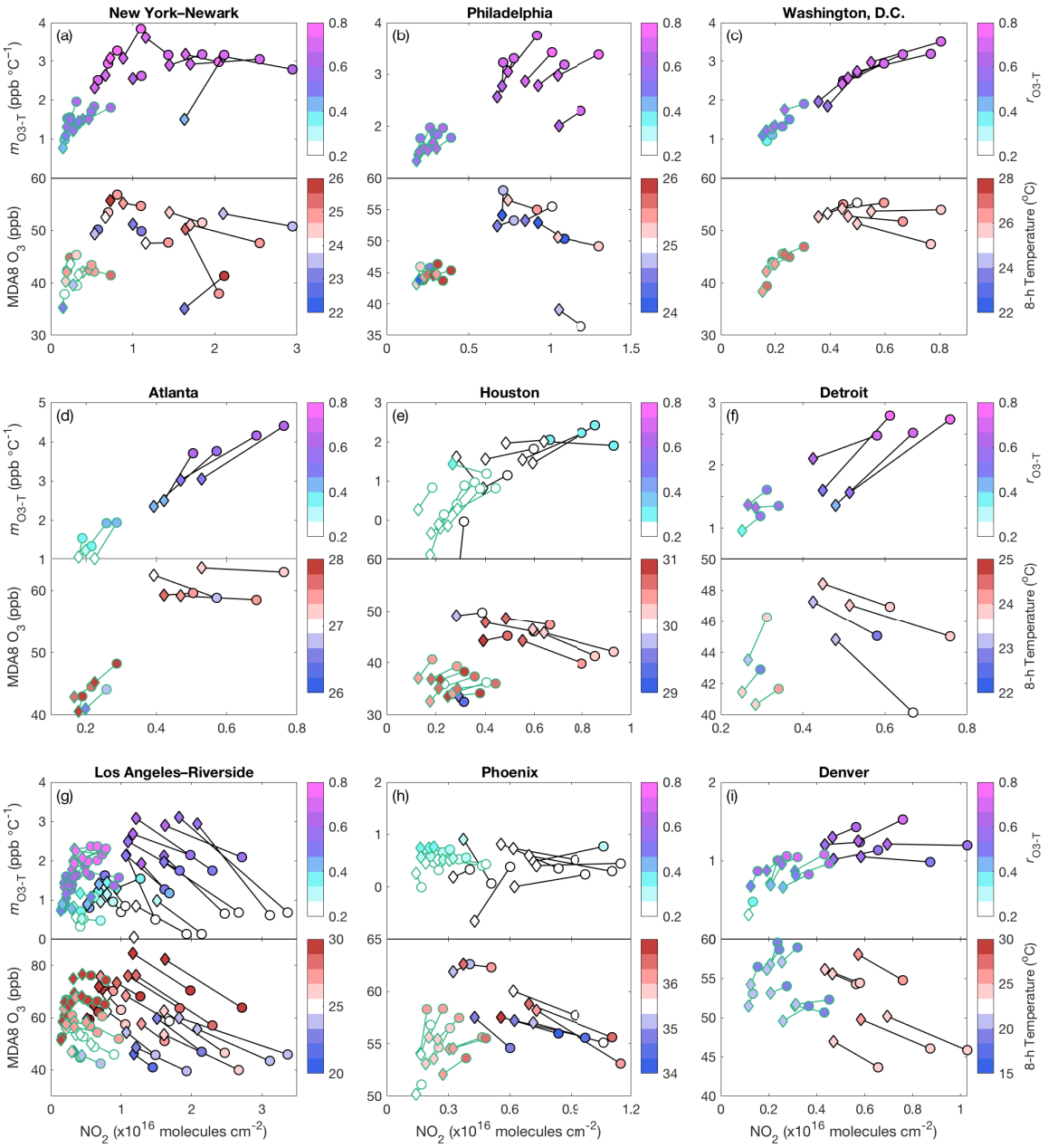

Figure 2.5. Weekday (circles) and weekend (diamonds) $m_{O3\text{-}T}$ (ppb °C^{-1}) (top) and MDA8 O_3 (ppb) (bottom) versus NO_2 TVCD (molecules cm^{-2}), where NO_2 is lower on weekends than weekdays by at least 0.1 x 10^{15} molecules cm^{-2}, colored by $r_{O3\text{-}T}$ and 8-h average daily temperature, respectively, in six MSAs: New York-Newark (a), Philadelphia-Camden-Wilmington (b), Washington-Arlington-Alexandria (c), Atlanta (d), Houston-The Woodlands-Sugar Land (e), Detroit-Warren-Dearborn (f), Los Angeles-Long Beach-Anaheim and Riverside-San Bernadino-Ontario (g), Phoenix-Mesa-Scottsdale (h), and Denver-Aurora-Lakewood (i). Weekday observations are binned every 0.3 x 10^{15} molecules cm^{-2} NO_2 and tethered to the corresponding mean values on weekends. Data in 1999–2001 are outlined in black and data in 2017–2019 are outlined in green. To support visualization only, NO_2 TVCDs in 1999–2001 are estimated by scaling 2018–2019 NO_2 TVCDs according to surface NO_2* mixing ratios in both periods.

2.4 Summary and Implications

The temperature dependence of $P\mathrm{O_3}$ has and continues to contribute to $m_{\mathrm{O3\text{-}T}}$ variability in many U.S. climate regions and $\mathrm{O_3}$-polluted MSAs since 1999–2001. This does not imply that other temperature-dependent processes are not also at play, but specifically that $P\mathrm{O_3}$ chemical relationships are emergent in the covariation of $m_{\mathrm{O3\text{-}T}}$, MDA8 $\mathrm{O_3}$, and $\mathrm{NO_2}$. My approach highlights processes important at moderate and high $\mathrm{NO_2}$ levels and where anthropogenic $\mathrm{NO_x}$ emissions patterns offer a constraint on the $\mathrm{NO_2}$ dependence, rather than on the spatiotemporal variability of low-$\mathrm{NO_2}$ $m_{\mathrm{O3\text{-}T}}$. Locations with $\mathrm{NO_x}$-limited $P\mathrm{O_3}$ are well suited for understanding non-production terms in the $\mathrm{O_3}$ mass balance (Pusede et al., 2015), for example, across the widely-used U.S. EPA Clean Air Status and Trends Network (CASTNET) (Bloomer et al., 2009; Brown-Steiner et al., 2015; Rasmussen et al., 2012; Strode et al., 2015; U.S. EPA CASTNET 2022), designed to monitor rural $\mathrm{O_3}$ trends, and coarse spatial resolution chemical transport models. $\mathrm{NO_2}$ TVCDs over the 83 CASTNET stations meeting the $m_{\mathrm{O3\text{-}T}}$ selection criteria in this analysis are on average 50% lower than measured over all monitors in my 2017–2019 dataset. Mean weekday-weekend $\mathrm{NO_2}$ TVCD differences over these CASTNET stations are statistically indistinguishable from zero, with just two locations experiencing weekday-weekend $\mathrm{NO_2}$ differences of at least 20%. The dominant temperature-dependent processes identified using CASTNET and/or coarse models can also affect cities, but their low-$\mathrm{NO_2}$ vantage is important context when describing the efficacy of anthropogenic $\mathrm{NO_x}$ emissions controls on $m_{\mathrm{O3\text{-}T}}$ in populated areas.

$\mathrm{NO_x}$ emissions reductions have the potential to further lower $m_{\mathrm{O3\text{-}T}}$ on weekdays in MSAs with Marginal to Extreme 2015 $\mathrm{O_3}$ NAAQS nonattainment designations, which I infer by comparing 2017–2019 MSA-level $m_{\mathrm{O3\text{-}T}}$ observations on weekdays and weekends, corresponding to a mean

weekend decrease in co-located NO_2 TVCDs of 20 ± 7%. The U.S. EPA recently tightened NO_x emissions standards on heavy-duty diesel trucks beginning in the 2027 model year, with proposed NO_x reductions of 60% by 2045 (Federal Register, 2022). My work suggests these NO_x controls will lower $m_{O3\text{-}T}$ in O_3-polluted MSAs, even where PO_3 continues to be NO_x-suppressed. While climate change will affect O_3 in multiple ways, NO_x emissions reductions have been and will continue to be an effective strategy for O_3-related climate adaptation in cities.

2.5 Appendix

Analytical PO_3 model. I model ozone production (PO_3) as a function of NO_x, VOC reactivity with hydroxyl radical (OH), the primary HO_x ($\equiv$ OH + HO_2 + RO_2) production rate (PHO_x), and alkyl nitrate branching ratio (R2 versus R9) following Murphy et al. (2006b) and Farmer (2011). The model is built on three assumptions: PHO_x and HO_x loss (LHO_x) are in steady state (eq. S1), peroxy nitrates (RO_2NO_2) are in equilibrium with radical precursors, and radical propagation is much faster than radical termination (eq. S2), where RH is any gas-phase organic molecule.

$$\text{(S1)} \quad PHO_x = 2k_{RO_2+RO_2}[RO_2]^2 + 2k_{RO_2+HO_2}[RO_2][HO_2] + 2k_{HO_2+HO_2}[HO_2]^2 + k_{OH+NO_2}[OH][NO_2] + \alpha k_{RO_2+NO}[RO_2][NO]$$

$$\text{(S2)} \quad [RO_2] = [HO_2] = \frac{k_{OH+RH}[RH][OH]}{(1-\alpha)\,k_{HO_2+NO}[NO]}$$

Radical propagation reactions are R1–R4 and termination reactions are R5–R9.

$$\text{(R1)} \quad RH + OH \xrightarrow{O_2,\,M} RO_2 + H_2O$$
$$\text{(R2)} \quad RO_2 + NO \rightarrow RO + NO_2$$
$$\text{(R3)} \quad RO + O_2 \rightarrow R'O + HO_2$$
$$\text{(R4)} \quad HO_2 + NO \rightarrow OH + NO_2$$
$$\text{(R5)} \quad RO_2 + RO_2 \rightarrow ROOR + O_2$$
$$\text{(R6)} \quad RO_2 + HO_2 \rightarrow HOOR + O_2$$
$$\text{(R7)} \quad HO_2 + HO_2 \rightarrow HOOH + O_2$$
$$\text{(R8)} \quad OH + NO_2 \rightarrow HNO_3$$
$$\text{(R9)} \quad RO_2 + NO \rightarrow RONO_2$$

The OH concentration is solved for with the quadradic equation, and PO_3 is given by eq S3.

$$\text{(S3)} \quad PO_3 = k_{RO_2+NO}[RO_2][NO] + k_{HO_2+NO}[HO_2][NO]$$

The termination reaction rates are based on the expressions at 300 K: $k_{NO_2+OH} = 2.58 \times 10^{-11}$ cm^3 molecules^{-1} s^{-1} (Mollner, 2010), $k_{RO_2+RO_2} = 6.8 \times 10^{-12}$ cm^3 molecules^{-1} s^{-1}, $k_{RO_2+HO_2} = 8.0 \times 10^{-12}$ cm^3 molecules^{-1} s^{-1}, and $k_{HO_2+HO_2} = 2.74 \times 10^{-14}$ cm^3 molecules^{-1} s^{-1} (Sander, 2006). RO_2 rates are for $C_2H_5O_2$ (Farmer, 2011; Perring, 2010).

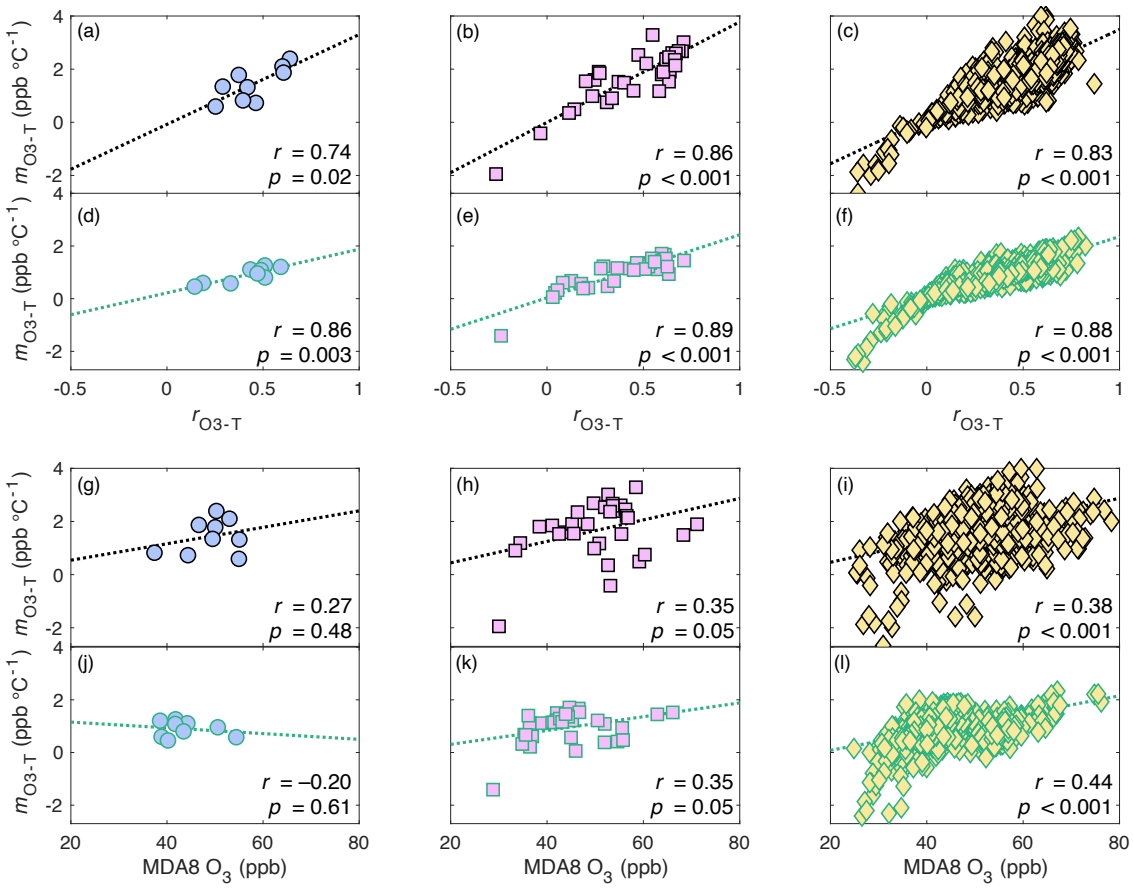

Figure 2.S1. $m_{O3\text{-}T}$ (ppb ºC^{-1}) versus $r_{O3\text{-}T}$ (top row) and MDA8 O_3 (ppb) (bottom row) in 1999–2001 (black outline) and 2017–2019 (green outline) in the nine climate regions (panels a, d, g, and j), 32 MSAs (panels b, e, h, and k), and at all O_3 monitors in the contiguous U.S. (panels c, f, i, and l). Lines of best fit (dashed), Pearson correlation coefficients (r), and fit p-values are shown.

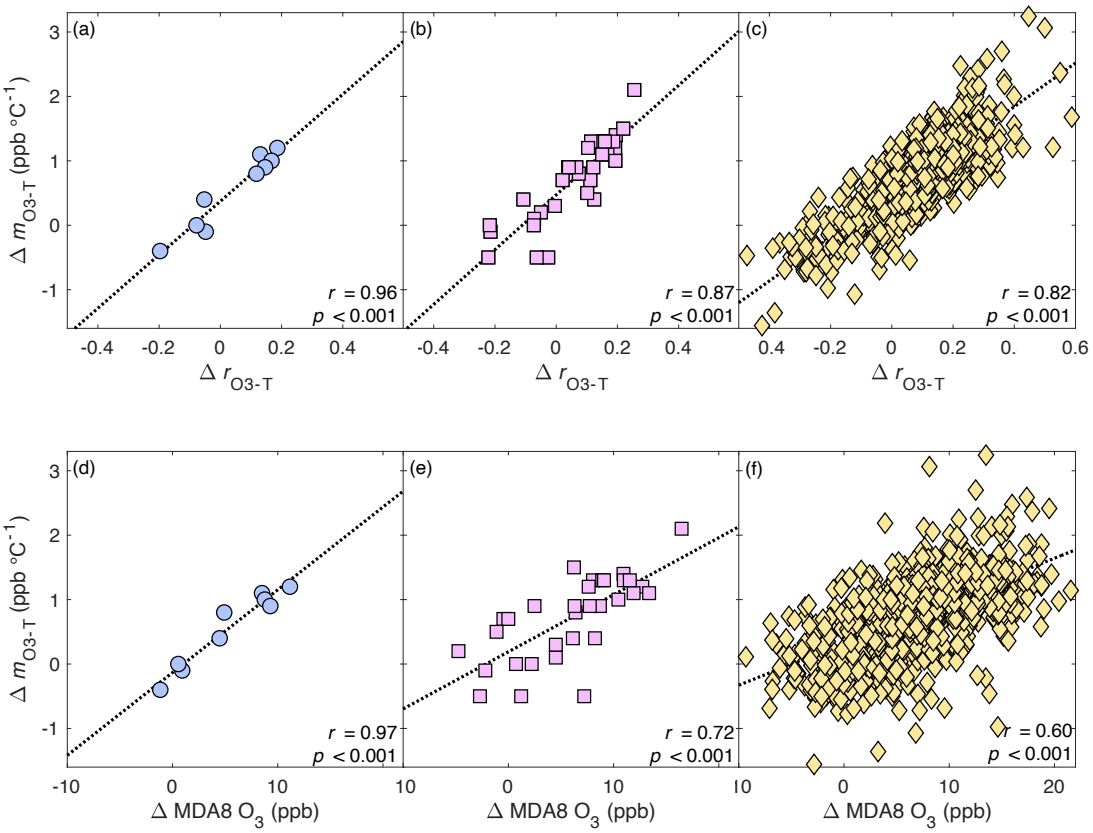

Figure 2.S2. Correlations between changes in $m_{O3\text{-}T}$ (ppb ºC^{-1}) versus changes in $r_{O3\text{-}T}$ and changes in MDA8 O_3 (ppb) between 1999–2001 and 2017–2019 in the nine climate regions (panels a and d), 32 MSAs (panels b and e), and at all O_3 monitors in the contiguous U.S. (panels c and f).

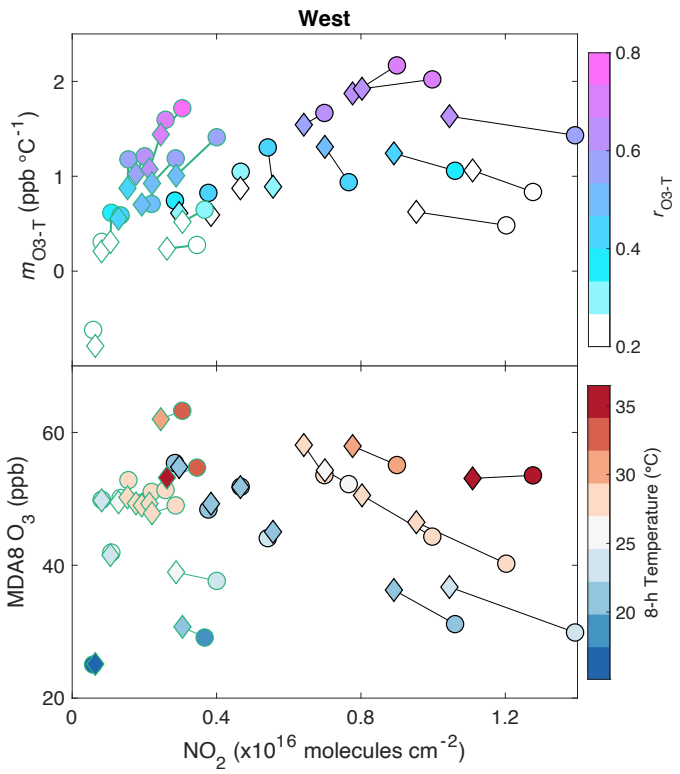

Figure 2.S3. Weekday (circles) and weekend (diamonds) $m_{O3\text{-}T}$ (ppb $^{o}C^{-1}$) (top) and MDA8 O_3 (ppb) (bottom) versus NO_2 TVCDs (molecules cm^{-2}) colored by $r_{O3\text{-}T}$ and 8-h average daily temperature, respectively, in the West excluding the Los Angeles and Riverside MSAs. Weekday observations are binned every 0.3 x 10^{15} molecules cm^{-2} NO_2 and tethered to the corresponding means on weekends. Data in 1999–2001 are outlined in black and data in 2017–2019 are outlined in green. To support the visualization only, NO_2 TCVDs in 1999–2001 are estimated by scaling 2018–2019 NO_2 TVCDs according to surface NO_2* mixing ratios in both periods as described in the Methods.

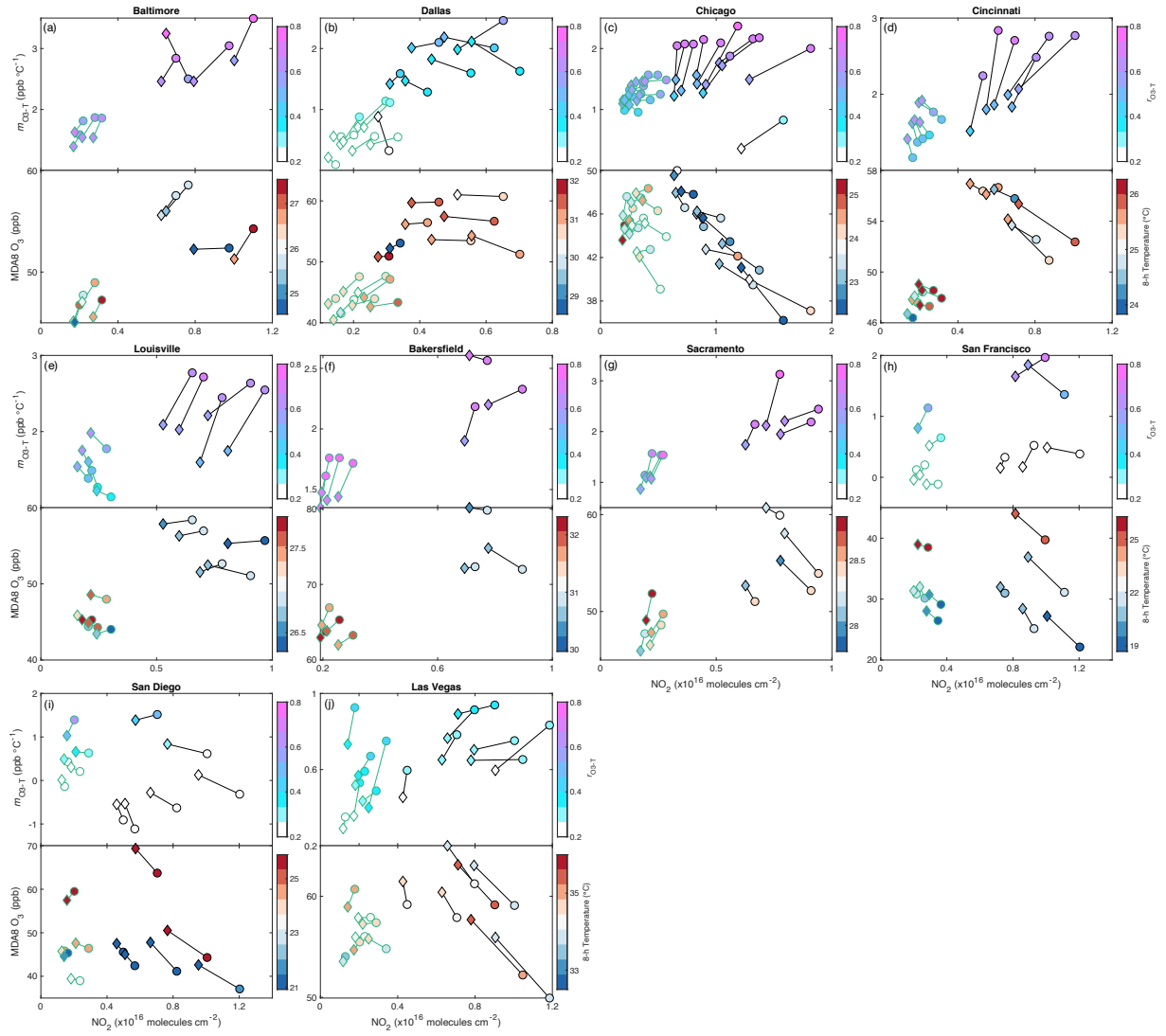

Figure 2.S4. Weekday (circles) and weekend (diamonds) $m_{O3\text{-}T}$ (ppb $^{o}C^{-1}$) (top) and MDA8 O_3 (ppb) (bottom) versus NO_2 TVCD (molecules cm^{-2}), where NO_2 is lower on weekends than weekdays by at least 0.1 x 10^{15} molecules cm^{-2}, colored by $r_{O3\text{-}T}$ and 8-h average daily temperature, respectively, in 10 MSAs: Baltimore-Columbia-Towson (a), Dallas-Fort Worth-Arlington (b), Chicago-Naperville-Elgin (c), Cincinnati (d), Louisville-Jefferson County (e), Bakersfield (f), Sacramento-Roseville-Arden-Arcade (g), San Francisco-Oakland-Hayward (h), San Diego-Carlsbad (i), and Las Vegas (j). Weekday observations are binned every 0.3 x 10^{15} molecules cm^{-2} NO_2 and tethered to the corresponding means on weekends. Data in 1999–2001 are outlined in black and data in 2017–2019 are outlined in green. To support visualization only, NO_2 TCVDs in 1999–2001 are estimated by scaling 2018–2019 NO_2 TVCDs according to surface NO_2* mixing ratios in both periods.

Table 2.S1. O_3-season percent difference in weekday–weekend NO_2 TVCD (%) and normalized mean average and mean maximum weekday–weekend decrease in $m_{O3\text{-}T}$ (ppb °C^{-1} per unit 10^{15} molecules NO_2 cm^{-2}) in 19 MSAs. Variability as 1 standard deviation is represented parenthetically.

	Weekday-weekend NO_2 TVCD (%)	**Normalized 2017–2019 weekday-weekend $m_{O3\text{-}T}$ (ppb °C^{-1} per unit 10^{15} molecules NO_2 cm^{-2})**	
		Mean	**Maximum**
Baltimore-Columbia-Towson, MD	20	0.7 (0.7)	2.3
Philadelphia-Camden-Wilmington, PA-NJ-DE-MD	21	0.7 (0.5)	2.1
New York-Newark-Jersey City, NY-NJ-PA	27	0.6 (0.5)	1.7
Atlanta, GA	12	1.7 (0.9)	3.3
Washington-Arlington-Alexandria, DC-VA-MD-WV	19	0.0 (0.3)	0.3
Chicago-Naperville-Elgin, IL-IN-WI	24	0.0 (0.3)	0.4
Cincinnati, OH-KY-IN	19	0.0 (0.3)	0.3
Louisville-Jefferson County, KY-IN	23	–0.5 (0.3)	–0.1
Dallas-Fort Worth-Arlington, TX	23	0.3 (0.8)	1.7
Houston-The Woodlands-Sugar Land, TX	33	1.1 (1.0)	4.4
Detroit-Warren-Dearborn, MI	13	0.5 (0.3)	0.9
Denver-Aurora-Lakewood, CO	20	0.5 (0.6)	2.0
Phoenix-Mesa-Scottsdale, AZ	25	–0.3 (0.6)	0.2
Bakersfield, CA	10	1.0 (0.3)	1.4
Las Vegas, NV	19	0.4 (0.4)	1.6
Los Angeles-Long Beach-Anaheim and Riverside-San Bernardino-Ontario, CA	32	0.1 (0.5)	1.2
Sacramento-Roseville-Arden-Arcade, CA	6	1.5 (0.6)	2.5
San Diego-Carlsbad, CA	20	–0.6 (1.6)	0.8
San Francisco-Oakland-Hayward, CA	18	0.6 (0.7)	1.8

References

Abeleira, A. J., and Farmer, D. K.: Summer ozone in the northern Front Range metropolitan area: weekend-weekday effects, temperature dependences, and the impact of drought, Atmospheric Chemistry and Physics, 17, 6517-6529, 10.5194/acp-17-6517-2017, 2017.

Ainsworth, E. A., Yendrek, C. R., Sitch, S., Collins, W. J., and Emberson, L. D.: The effects of tropospheric ozone on net primary productivity and implications for climate change, Annu Rev Plant Biol, 63, 637-661, 10.1146/annurev-arplant-042110-103829, 2012.

Avise, J., Abraham, R. G., Chung, S. H., Chen, J., Lamb, B., Salathe, E. P., Zhang, Y. X., Nolte, C. G., Loughlin, D. H., Guenther, A., Wiedinmyer, C., and Duhl, T.: Evaluating the effects of climate change on summertime ozone using a relative response factor approach for policymakers, Journal of the Air & Waste Management Association, 62, 10.1080/10962247.2012.696531, 2012.

Aw, J., and Kleeman, M. J.: Evaluating the first-order effect of intraannual temperature variability on urban air pollution, Journal of Geophysical Research-Atmospheres, 108, 10.1029/2002jd002688, 2003.

Barnes, E. A., and Fiore, A. M.: Surface ozone variability and the jet position: Implications for projecting future air quality, Geophysical Research Letters, 40, 2839-2844, 10.1002/grl.50411, 2013.

Bloomer, B. J., Stehr, J. W., Piety, C. A., Salawitch, R. J., and Dickerson, R. R.: Observed relationships of ozone air pollution with temperature and emissions, Geophysical Research Letters, 36, L09803, doi:10.1029/2009GL037308, 2009.

Brown-Steiner, B., Hess, P. G., and Lin, M. Y.: On the capabilities and limitations of GCCM simulations of summertime regional air quality: A diagnostic analysis of ozone and temperature simulations in the US using CESM CAM-Chem, Atmospheric Environment, 101, 134-148, 10.1016/j.atmosenv.2014.11.001, 2015.

Bunce, J. A.: Responses of stomatal conductance to light, humidity and temperature in winter wheat and barley grown at three concentrations of carbon dioxide in the field, Global Change Biology, 6, 371-382, 2000.

Buysse, C. E., Munyan, J. A., Bailey, C. A., Kotsakis, A., Sagona, J. A., Esperanza, A., and Pusede, S. E.: On the Effect of Upwind Emission Controls on Ozone in Sequoia National Park, Atmos. Chem. Phys., 18, 17061-17076, 10.5194/acp-18-17061-2018, 2018.

Buysse, C. E., Kaulfus, A., Nair, U., and Jaffe, D. A.: Relationships between Particulate Matter, Ozone, and Nitrogen Oxides during Urban Smoke Events in the Western US, Environ. Sci. Technol., 53, 12519-12528, 10.1021/acs.est.9b05241, 2019.

Camalier, L., Cox, W., and Dolwick, P.: The effects of meteorology on ozone in urban areas and their use in assessing ozone trends, Atmospheric Environment, 41, 7127-7137, 10.1016/j.atmosenv.2007.04.061, 2007.

Coates, J., Mar, K. A., Ojha, N., and Butler, T. M.: The influence of temperature on ozone production under varying NOx conditions – a modelling study, Atmospheric Chemistry and Physics, 16, 11601-11615, 10.5194/acp-16-11601-2016, 2016.

Cohen, A. J., Brauer, M., Burnett, R., Anderson, H. R., Frostad, J., Estep, K., Balakrishnan, K., Brunekreef, B., Dandona, L., Dandona, R., Feigin, V., Freedman, G., Hubbell, B., Jobling, A., Kan, H., Knibbs, L., Liu, Y., Martin, R., Morawska, L., Pope, C. A., Shin, H., Straif, K., Shaddick, G., Thomas, M., van Dingenen, R., van Donkelaar, A., Vos, T., Murray, C. J. L., and Forouzanfar, M. H.: Estimates and 25-year trends of the global burden of disease attributable to ambient air pollution: an analysis of data from the Global Burden of Diseases Study 2015, The Lancet, 389, 1907-1918, 10.1016/s0140-6736(17)30505-6, 2017.

Control of Air Pollution From New Motor Vehicles: Heavy-Duty Engine and Vehicle Standards. Agency, E. P., Ed. Federal Register: 2022; Vol. Vo. 87, No. 59.

Cooper, O. R., Gao, R.-S., Tarasick, D., Leblanc, T., and Sweeney, C.: Long-term ozone trends at rural ozone monitoring sites across the United States, 1990-2010, Journal of Geophysical Research: Atmospheres, 117, D22307, 10.1029/2012JD018261, 2012.

Dai, A. G.: Drought under global warming: a review, Wiley Interdisciplinary Reviews-Climate Change, 2, 45-65, 10.1002/wcc.81, 2011.

de Foy, B., Brune, W. H., and Schauer, J. J.: Changes in ozone photochemical regime in Fresno, California from 1994 to 2018 deduced from changes in the weekend effect, Environmental Pollution, 263, 10.1016/j.envpol.2020.114380, 2020.

Demetillo, M. A. G., Anderson, J. F., Geddes, J. A., Yang, X., Najacht, E. Y., Herrera, S. A., Kabasares, K. M., Kotsakis, A. E., Lerdau, M. T., and Pusede, S. E.: Observing Severe Drought Influences on Ozone Air Pollution in California, Environmental Science & Technology, 53, 4695-4706, 10.1021/acs.est.8b04852, 2019.

Di Carlo, P., Brune, W. H., Martinez, M., Harder, H., Lesher, R., Ren, X., Thornberry, T., Carroll, M. A., Young, V., Shepson, P. B., Riemer, D., Apel, E., and Campbell, C.: Missing OH Reactivity in a Forest: Evidence for Unknown Reactive Biogenic VOCs, Science, 304, 722-725, 10.1126/science.1094392, 2004.

Dunlea, E. J., Herndon, S. C., Nelson, D. D., Volkamer, R. M., San Martini, F., Sheehy, P. M., Zahniser, M. S., Shorter, J. H., Wormhoudt, J. C., Lamb, B. K., Allwine, E. J., Gaffney, J. S., Marley, N. A., Grutter, M., Marquez, C., Blanco, S., Cardenas, B., Retama, A., Ramos Villegas, C. R., Kolb, C. E., Molina, L. T., and Molina, M. J.: Evaluation of nitrogen dioxide chemiluminescence monitors in a polluted urban environment, Atmos. Chem. Phys., 7, 2691-2704, 10.5194/acp-7-2691-2007, 2007.

Farmer, D. K., and Cohen, R. C.: Observations of HNO_3, ΣAN, ΣPN and NO_2 Fluxes: evidence for rapid HO_x chemistry within a pine forest canopy, Atmos. Chem. Phys., 8, 3899-3917, 10.5194/acp-8-3899-2008, 2008.

Farmer, D. K. P., A. E.; Wooldridge, P. J.; Blake, D. R.; Baker, A.; Meinardi, S.; Huey, L. G.; Tanner, D.; Vargas, O.; Cohen, R. C.: Impact of organic nitrates on urban ozone production, Atmospheric Chemistry and Physics, 11, 4085-4094, 2011.

Fiore, A. M., Naik, V., Spracklen, D. V., Steiner, A., Unger, N., Prather, M., Bergmann, D., Cameron-Smith, P. J., Cionni, I., Collins, W. J., Dalsoren, S., Eyring, V., Folberth, G. A., Ginoux, P., Horowitz, L. W., Josse, B., Lamarque, J. F., MacKenzie, I. A., Nagashima, T., O'Connor, F. M., Righi, M., Rumbold, S. T., Shindell, D. T., Skeie, R. B., Sudo, K., Szopa, S., Takemura, T., and Zeng, G.: Global air quality and climate, Chemical Society Reviews, 41, 6663-6683, 10.1039/c2cs35095e, 2012.

Fowler, D., Pilegaard, K., Sutton, M. A., Ambus, P., Raivonen, M., Duyzer, J., Simpson, D., Fagerli, H., Fuzzi, S., Schjoerring, J. K., Granier, C., Neftel, A., Isaksen, I. S. A., Laj, P., Maione, M., Monks, P. S., Burkhardt, J., Daemmgen, U., Neirynck, J., Personne, E., Wichink-Kruit, R., Butterbach-Bahl, K., Flechard, C., Tuovinen, J. P., Coyle, M., Gerosa, G., Loubet, B., Altimir, N., Gruenhage, L., Ammann, C., Cieslik, S., Paoletti, E., Mikkelsen, T. N., Ro-Poulsen, H., Cellier, P., Cape, J. N., Horváth, L., Loreto, F., Niinemets, Ü., Palmer, P. I., Rinne, J., Misztal, P., Nemitz, E., Nilsson, D., Pryor, S., Gallagher, M. W., Vesala, T., Skiba, U., Brüggemann, N., Zechmeister-Boltenstern, S., Williams, J., O'Dowd, C., Facchini, M. C., de Leeuw, G., Flossman, A., Chaumerliac, N., and Erisman, J. W.: Atmospheric composition change: Ecosystems–Atmosphere interactions, Atmospheric Environment, 43, 5193-5267, 10.1016/j.atmosenv.2009.07.068, 2009.

Geddes, J. A., Wang, B., and Li, D.: Ozone and Nitrogen Dioxide Pollution in a Coastal Urban Environment: The Role of Sea Breezes, and Implications of Their Representation for Remote Sensing of Local Air Quality, J. Geophys. Res.-Atmos., 126, 10.1029/2021jd035314, 2021.

Graney, J. R., Dvonch, J. T., and Keeler, G. J.: Use of multi-element tracers to source apportion mercury in south Florida aerosols, Atmospheric Environment, 38, 1715-1726, 10.1016/j.atmosenv.2003.12.018, 2004.

Guenther, A., Karl, T., Harley, P., Wiedinmyer, C., Palmer, P. I., and Geron, C.: Estimates of Global Terrestrial Isoprene Emissions Using MEGAN (Model of Emissions of Gases and Aerosols from Nature), Atmos. Chem. Phys., 6, 3181-3210, 10.5194/acp-6-3181-2006, 2006.

Haagen-Smit, A. J., and Fox, M. M.: Photochemical Ozone Formation with Hydrocarbons and Automobile Exhaust, Air Repair, 4, 105-136, 10.1080/00966665.1954.10467649, 1954.

He, H., Hembeck, L., Hosley, K. M., Canty, T. P., Salawitch, R. J., and Dickerson, R. R.: High ozone concentrations on hot days: The role of electric power demand and NO_x emissions, Geophysical Research Letters, 40, 5291-5294, 10.1002/grl.50967, 2013.

Iowa Environmental Mesonet: mesonet.agron.iastate.edu/, access: November 1, 2022.

Ito, A., Sillman, S., and Penner, J. E.: Global chemical transport model study of ozone response to changes in chemical kinetics and biogenic volatile organic compounds emissions due to increasing temperatures: Sensitivities to isoprene nitrate chemistry and grid resolution, Journal of Geophysical Research-Atmospheres, 114, 10.1029/2008jd011254, 2009.

Iowa Environmental Mesonet: mesonet.agron.iastate.edu/, access: November 1, 2022.

Jacob, D. J., and Winner, D. A.: Effect of climate change on air quality, Atmospheric Environment, 43, 51-63, 10.1016/j.atmosenv.2008.09.051, 2009.

Jaffe, D., Chand, D., Hafner, W., Westerling, A., and Spracklen, D.: Influence of Fires on O3 Concentrations in the Western U.S, Environ. Sci. Technol., 42, 5885-5891, 10.1021/es800084k, 2008.

Jaffe, D.: Relationship between Surface and Free Tropospheric Ozone in the Western U.S, Environ. Sci. Technol., 45, 432-438, 10.1021/es1028102, 2011.

Jaffe, D. A., and Wigder, N. L.: Ozone production from wildfires: A critical review, Atmos. Environ., 51, 1-10, https://doi.org/10.1016/j.atmosenv.2011.11.063, 2012.

Jaffe, D. A., and Zhang, L.: Meteorological anomalies lead to elevated O_3 in the western U.S. in June 2015, Geophysical Research Letters, 44, 1990-1997, https://doi.org/10.1002/2016GL072010, 2017.

Jerrett, M., Burnett, R. T., Pope III, C. A., Ito, K., Thurston, G., Krewski, D., Shi, Y., Calle, E., and Thun, M.: Long-Term Ozone Exposure and Mortality, The New England Journal of Medicine, 360, 1085-1095, 2009.

Jiang, Z., McDonald, B. C., Worden, H., Worden, J. R., Miyazaki, K., Qu, Z., Henze, D. K., Jones, D. B. A., Arellano, A. F., Fischer, E. V., Zhu, L., and Boersma, K. F.: Unexpected Slowdown of U.S. Pollutant Emission Reduction in the Past Decade, Proc. Natl. Acad. Sci. U. S. A., 115, 5099-5104, 10.1073/pnas.1801191115, 2018.

Karl, T., and Koss, W. J.: Regional and National Monthly, Seasonal, and Annual Temperature Weighted by Area, 1895−1983. , National Climatic Data Center, Asheville, NC, 38, 1984.

Kavassalis, S. C., and Murphy, J. G.: Understanding ozone-meteorology correlations: A role for dry deposition, Geophysical Research Letters, 44, 2922-2931, 10.1002/2016gl071791, 2017.

Kerr, G. H., Waugh, D. W., Strode, S. A., Steenrod, S. D., Oman, L. D., and Strahan, S. E.: Disentangling the Drivers of the Summertime Ozone-Temperature Relationship Over the United States, Journal of Geophysical Research Atmospheres, 124, 10503-10524, https://doi.org/10.1029/2019JD030572, 2019.

Kerr, G. H., Waugh, D. W., Steenrod, S. D., Strode, S. A., and Strahan, S. E.: Surface Ozone-Meteorology Relationships: Spatial Variations and the Role of the Jet Stream, Journal of Geophysical Research-Atmospheres, 125, 10.1029/2020jd032735, 2020.

Li, J., Mao, J., Fiore, A. M., Cohen, R. C., Crounse, J. D., Teng, A. P., Wennberg, P. O., Lee, B. H., Lopez-Hilfiker, F. D., Thornton, J. A., Peischl, J., Pollack, I. B., Ryerson, T. B., Veres, P., Roberts, J. M., Neuman, J. A., Nowak, J. B., Wolfe, G. M., Hanisco, T. F., Fried, A., Singh, H. B., Dibb, J., Paulot, F., and Horowitz, L. W.: Decadal changes in summertime reactive oxidized nitrogen and surface ozone over the Southeast United States, Atmospheric Chemistry and Physics, 18, 2341-2361, https://doi.org/10.5194/acp-18-2341-2018, 2018.

Marr, L. C., and Harley, R. A.: Modeling the Effect of Weekday−Weekend Differences in Motor Vehicle Emissions on Photochemical Air Pollution in Central California, Environmental Science & Technology, 36, 4099-4106, 10.1021/es020629x, 2002.

Mollner, A. K. V., S.; Feng, L.; Sprague, M. K.; Okumura, M.; Milligan, D. B.; Bloss, W. J.; Sander, S. P.; Martien, P. T.; Harley, R. A.; McCoy, A. B.; Carter, W. P. L.: Rate of Gas Phase Association of Hydroxyl Radical and Nitrogen Dioxide, SCIENCE, 330, 646-649, 2010.

Murphy, J. G., Day, A., Cleary, P. A., Wooldridge, P. J., and Cohen, R. C.: Observations of the Diurnal and Seasonal Trends in Nitrogen Oxides in the Western Sierra Nevada, Atmos. Chem. Phys., 6, 5321-5338, 10.5194/acp-6-5321-2006, 2006a.

Murphy, J. G., Day, D. A., Cleary, P. A., Wooldridge, P. J., Millet, D. B., Goldstein, A. H., and Cohen, R. C.: The weekend effect within and downwind of Sacramento: Part 2. Observational evidence for chemical and dynamical contributions, Atmos. Chem. Phys. Discuss., 6, 11971–12019, doi:10.5194/acpd6-11971-2006, 2006b.

Murphy, J. G., Day, D. A., Cleary, P. A., Wooldridge, P. J., Millet, D. B., Goldstein, A. H., and Cohen, R. C.: The weekend effect within and downwind of Sacramento - Part 1: Observations of ozone, nitrogen oxides, and VOC reactivity, Atmos. Chem. Phys., 7, 5327-5339, 10.5194/acp-7-5327-2007, 2007.

Ninneman, M., and Jaffe, D.: Observed Relationship between Ozone and Temperature for Urban Nonattainment Areas in the United States, Atmosphere, 12, 1235, https://doi.org/10.3390/atmos12101235, 2021.

Nolte, C. G., Spero, T. L., Bowden, J. H., Sarofim, M. C., Martinich, J., and Mallard, M. S.: Regional temperature-ozone relationships across the U.S. under multiple climate and emissions scenarios, Journal of the Air & Waste Management Association, 71, 1251-1264, 10.1080/10962247.2021.1970048, 2021.

Nussbaumer, C. M., and Cohen, R. C.: The Role of Temperature and NO_x in Ozone Trends in the Los Angeles Basin, Environmental Science & Technology, 54, 15652-15659, 10.1021/acs.est.0c04910, 2020.

Otero, N., Jurado, O. E., Butler, T., and Rust, H. N. W.: The impact of atmospheric blocking on the compounding effect of ozone pollution and temperature: a copula-based approach, Atmospheric Chemistry and Physics, 22, 1905-1919, 10.5194/acp-22-1905-2022, 2022.

Perdigones, B. C., Lee, S., Cohen, R. C., Park, J. H., and Min, K. E.: Two Decades of Changes in Summertime Ozone Production in California's South Coast Air Basin, Environmental Science & Technology, 56, 10586-10595, 10.1021/acs.est.2c0102610586, 2022.

Perring, A. E. B., T. H.; Farmer, D. K.; Wooldridge, P. J.; Dibb, J.; Blake, N. J.; Blake, D. R.; Singh, H. B.; Fuelberg, H.; Diskin, G.; Sachse, G.; Cohen, R. C.: The production and persistence of $\Sigma RONO_2$ in the Mexico City plume, Atmospheric Chemistry and Physics, 10, 7215-7229, 2010.

Pfister, G. G., Wiedinmyer, C., and Emmons, L. K.: Impacts of the fall 2007 California wildfires on surface ozone: Integrating local observations with global model simulations, Geophys. Res. Lett., 35, 10.1029/2008gl034747, 2008.

Pollack, I. B., Ryerson, T. B., Trainer, M., Parrish, D. D., Andrews, A. E., Atlas, E. L., Blake, D. R., Brown, S. S., Commane, R., Daube, B. C., de Gouw, J. A., Dube, W. P., Flynn, J., Frost, G. J., Gilman, J. B., Grossberg, N., Holloway, J. S., Kofler, J., Kort, E. A., Kuster, W. C., Lang, P. M., Lefer, B., Lueb, R. A., Neuman, J. A., Nowak, J. B., Novelli, P. C., Peischl, J., Perring, A. E., Roberts, J. M., Santoni, G., Schwarz, J. P., Spackman, J. R., Wagner, N. L., Warneke, C., Washenfelder, R. A., Wofsy, S. C., and Xiang, B.: Airborne and ground-based observations of a weekend effect in ozone, precursors, and oxidation products in the California South Coast Air Basin, J. Geophys. Res.-Atmos., 117, 10.1029/2011jd016772, 2012.

Pollack, I. B., Helmig, D., O'Dell, K., and Fischer, E. V.: Weekend-Weekday Implications and the Impact of Wildfire Smoke on Ozone and Its Precursors at Boulder Reservoir, Colorado Between 2017 and 2019, Journal of Geophysical Research-Atmospheres, 126, 10.1029/2021jd035221, 2021.

Porter, W. C., and Heald, C. L.: The mechanisms and meteorological drivers of the summertime ozone-temperature relationship, Atmospheric Chemistry and Physics, 19, 13367–13381, https://doi.org/10.5194/acp-19-13367-2019, 2019.

Pusede, S. E., and Cohen, R. C.: On the observed response of ozone to NO_x and VOC reactivity reductions in San Joaquin Valley California 1995-present, Atmospheric Chemistry and Physics, 12, 8323-8339, 10.5194/acp-12-8323-2012, 2012.

Pusede, S. E., Gentner, D. R., Wooldridge, P. J., Browne, E. C., Rollins, A. W., Min, K. E., Russell, A. R., Thomas, J., Zhang, L., Brune, W. H., Henry, S. B., DiGangi, J. P., Keutsch, F. N., Harrold, S. A., Thornton, J. A., Beaver, M. R., St. Clair, J. M., Wennberg, P. O., Sanders, J., Ren, X., VandenBoer, T. C., Markovic, M. Z., Guha, A., Weber, R.,

Goldstein, A. H., and Cohen, R. C.: On the temperature dependence of organic reactivity, nitrogen oxides, ozone production, and the impact of emission controls in San Joaquin Valley, California, Atmospheric Chemistry and Physics, 14, 3373-3395, 10.5194/acp-14-3373-2014, 2014.

Pusede, S. E., Steiner, A. L., and Cohen, R. C.: Temperature and recent trends in the chemistry of continental surface ozone, Chem Rev, 115, 3898-3918, 10.1021/cr5006815, 2015.

Rasmussen, D. J., Fiore, A. M., Naik, V., Horowitz, L. W., McGinnis, S. J., and Schultz, M. G.: Surface ozone-temperature relationships in the eastern US: A monthly climatology for evaluating chemistry-climate models, Atmospheric Environment, 47, 142-153, 10.1016/j.atmosenv.2011.11.021, 2012.

Rasmussen, D. J., Hu, J., Mahmud, A., and Kleeman, M. J.: The Ozone-Climate Penalty: Past, Present, and Future, Environ. Sci. Technol., 47, 14258-14266, 10.1021/es403446m, 2013.

Reich, P. B.: Quantifying plant response to ozone: a unifying theory, Tree Physiol, 3, 63-91, 10.1093/treephys/3.1.63, 1987.

Rieder, H. E., Fiore, A. M., Clifton, O. E., Correa, G., Horowitz, L. W., and Naik, V.: Combining model projections with site-level observations to estimate changes in distributions and seasonality of ozone in surface air over the U.S.A., Atmospheric Environment, 193, 302-315, https://doi.org/10.1016/j.atmosenv.2018.07.042, 2018.

Romer, P. S., Duffey, K. C., Wooldridge, P. J., Edgerton, E., Baumann, K., Feiner, P. A., Miller, D. O., Brune, W. H., Koss, A. R., de Gouw, J. A., Misztal, P. K., Goldstein, A. H., and Cohen, R. C.: Effects of temperature-dependent NO_x emissions on continental ozone production, Atmospheric Chemistry and Physics, 18, 2601-2614, https://doi.org/10.5194/acp-18-2601-2018, 2018.

Russell, A. R., Valin, L. C., Bucsela, E. J., Wenig, M. O., and Cohen, R. C.: Space-based Constraints on Spatial and Temporal Patterns of NO_x Emissions in California, 2005-2008, Environmental Science & Technology, 44, 3608-3615, 10.1021/es903451j, 2010.

Russell, A. R., Valin, L. C., and Cohen, R. C.: Trends in OMI NO_2 observations over the United States: effects of emission control technology and the economic recession, Atmospheric Chemistry and Physics, 12, 12197-12209, 10.5194/acp-12-12197-2012, 2012.

Sander, S. P. F.-P., B. J.; Friedl, R. R.; Golden, D. M.; Huie, R. E.; Keller-Rudek, H.; Kolb, C. E.; Kurylo, M. J.; Molina, M. J.; Moortgat, G. K.; Orkin, V. L.; Ravishankara, A. R.; Wine, P. H.: Chemical Kinetics and Photochemical Data for Use in Atmospheric Studies, Evaluation Number 15 in JPL Publication 06-2, Jet Propulsion Laboratory, 2006.

Schwarzman, M., Schildroth, S., Bhetraratana, M., Alvarado, A., and Balmes, J.: Raising standards to lower diesel emissions, Science, 371, 1314-1316, 10.1126/science.abf8159, 2021.

Seinfeld, J. H.: Rethinking the ozone Problem in Urban and Regional Air Pollution, National Academy Press, Washington, D.C., 1991.

Shen, L., Mickley, L. J., and Tai, A. P. K.: Influence of synoptic patterns on surface ozone variability over the eastern United States from 1980 to 2012, Atmospheric Chemistry and Physics, 15, 10925-10938, 10.5194/acp-15-10925-2015, 2015.

Sillman, S., and Samson, F. J.: Impact of temperature on oxidant photochemistry in urban polluted rural and remote environments, Journal of Geophysical Research-Atmospheres, 100, 11497-11508, 10.1029/94jd02146, 1995.

Simon, H., Reff, A., Wells, B., Xing, J., and Frank, N.: Ozone Trends Across the United States over a Period of Decreasing NO_x and VOC Emissions, Environmental Science & Technology, 49, 186-195, 10.1021/es504514z, 2015.

Spracklen, D. V., Mickley, L. J., Logan, J. A., Hudman, R. C., Yevich, R., Flannigan, M. D., and Westerling, A. L.: Impacts of climate change from 2000 to 2050 on wildfire activity and carbonaceous aerosol concentrations in the western United States, J. Geophys. Res.-Atmos., 114, 10.1029/2008jd010966, 2009.

Steiner, A. L., Tonse, S., Cohen, R. C., Goldstein, A. H., and Harley, R. A.: Influence of future climate and emissions on regional air quality in California, Journal of Geophysical Research, 111, 10.1029/2005jd006935, 2006.

Steiner, A. L., Davis, A. J., Sillman, S., Owen, R. C., Michalak, A. M., and Fiore, A. M.: Observed Suppression of Ozone Formation at Extremely High Temperatures Due to Chemical and Biophysical Feedbacks, Proc. Natl. Acad. Sci. U. S. A., 107, 19685-19690, 10.1073/pnas.1008336107, 2010.

Stephens, S., Madronich, S., Wu, F., Olson, J. B., Ramos, R., Retama, A., and Muñoz, R.: Weekly patterns of México City's surface concentrations of CO, NO_x, PM_{10} and O_3 during 1986–2007, Atmos. Chem. Phys., 8, 5313-5325, 10.5194/acp-8-5313-2008, 2008.

Strode, S. A., Rodriguez, J. M., Logan, J. A., Cooper, O. R., Witte, J. C., Lamsal, L. N., Damon, M., Van Aartsen, B., Steenrod, S. D., and Strahan, S. E.: Trends and variability in surface ozone over the United States, Journal of Geophysical Research-Atmospheres, 120, 9020-9042, 10.1002/2014jd022784, 2015.

Sun, K., Zhu, L., Cady-Pereira, K., Chan Miller, C., Chance, K., Clarisse, L., Coheur, P.-F., González Abad, G., Huang, G., Liu, X., Van Damme, M., Yang, K., and Zondlo, M.: A physics-based approach to oversample multi-satellite, multispecies observations to a common grid, Atmospheric Measurement Techniques, 11, 6679-6701, 10.5194/amt-11-6679-2018, 2018.

Tawfik, A. B., and Steiner, A. L.: A proposed physical mechanism for ozone-meteorology correlations using land-atmosphere coupling regimes, Atmospheric Environment, 72, 50-59, http://dx.doi.org/10.1016/j.atmosenv.2013.03.002, 2013.

Urban, J., Ingwers, M., McGuire, M. A., and Teskey, R. O.: Stomatal conductance increases with rising temperature, Plant Signal Behav, 12, e1356534, 10.1080/15592324.2017.1356534, 2017.

U.S. EPA: Clean Air Status and Trends Network (CASTNET): epa.gov/castnet, access: March 8, 2022.

U.S. EPA: Green Book: epa.gov/green-book, access: February 28, 2022.

U.S. EPA: Air Data: epa.gov/outdoor-air-quality-data, access: November 14, 2022.

van Geffen, J. H. G. M., Eskes, H. J., Boersma, K. F., Maaskkers, J. D., and Veefkind, J. P.: TROPOMI ATBD of the total and tropospheric NO_2 data products, KNMI, 2019.

Veefkind, J. P., Aben, I., McMullan, K., Förster, H., de Vries, J., Otter, G., Claas, J., Eskes, H. J., de Haan, J. F., Kleipool, Q., van Weele, M., Hasekamp, O., Hoogeveen, R., Landgraf, J., Snel, R., Tol, P., Ingmann, P., Voors, R., Kruizinga, B., Vink, R., Visser, H., and Levelt, P. F.: TROPOMI on the ESA Sentinel-5 Precursor: A GMES mission for global observations of the atmospheric composition for climate, air quality and ozone layer applications, Remote Sensing of Environment, 120, 70-83, 10.1016/j.rse.2011.09.027, 2012.

Westerling, A. L., Gershunov, A., Brown, T. J., Cayan, D. R., and Dettinger, M. D.: Climate and wildfire in the western United States, Bull. Am. Meteorol. Soc., 84, 595-+, 10.1175/bams-84-5-595, 2003.

Wu, S., Mickley, L. J., Leibensperger, E. M., Jacob, D. J., Rind, D., and Streets, D. G.: Effects of 2000–2050 global change on ozone air quality in the United States, Journal of Geophysical Research Atmospheres, 113, D06302, 10.1029/2007JD008917, 2008.

Zhao, S. L., Pappin, A. J., Mesbah, S. M., Zhang, J. Y. J., MacDonald, N. L., and Hakami, A.: Adjoint estimation of ozone climate penalties, Geophysical Research Letters, 40, 5559-5563, 10.1002/2013gl057623, 2013.

CHAPTER 3: MEASURING OZONE FLUX AND DEPOSITION VELOCITIES IN A CENTRAL VIRGINIA FOREST

3.1 Introduction

Ozone (O_3) is an air pollutant and short-lived greenhouse gas that is harmful to people and plants (Jerrett et al., 2009; Reich, 1987). Chemical transport models suggest 15–30% of O_3 is lost annually from the troposphere by dry deposition to the Earth's surface (Wild, 2007; Young et al., 2013). Therefore, the O_3 deposition velocity (v_d) is an important variable in the global O_3 budget. However, O_3 depositional loss is among the most uncertain and poorly constrained terms in the O_3 mass balance (Wild, 2007). O_3 v_d varies with vegetation type, land cover type, and environmental conditions, which influence the rates and relative rates of stomatal and nonstomatal O_3 uptake. Daily mean O_3 v_d over vegetation frequently ranges 0–1 cm s^{-1}, with higher O_3 v_d over forests and croplands and lower O_3 v_d over grasslands and tundra (Hardacre et al., 2015), with half-hourly measurements potentially exceeding 2 cm s^{-1} (Fares et al., 2014; Muller et al., 2009; Turnipseed et al., 2009). The O_3 v_d is both over and under predicted by models, sometimes by a factor of two (Clifton et al., 2017; Fowler et al., 2009; Hardacre et al., 2015; Martin et al., 2014). Uncertainties are due in part to lack of O_3 v_d observations over time periods capturing the full variability in environmental conditions (Clifton et al., 2020) and with many global ecosystems either under- or unsampled (Young et al., 2018).

O_3 v_d observations are challenging to collect and not routinized with few commercial options. O_3 v_d is empirically determined from the O_3 flux (F_{O3}) (Eq. 1), where F_{O3} is a measurement of the

covariation between the deviation of O_3 and vertical wind velocity from their means, inferring O_3 exchange between the atmosphere and biosphere. Observational techniques and approaches for estimating F_{O3} at the canopy scale include the flux-gradient, modified Bowen ratio, and eddy covariance methods. Leaf and soil chambers can also be used to quantify O_3 v_d, but their small footprints make canopy-scale estimates difficult to extrapolate (Clifton et al., 2020). The eddy covariance approach is widely accepted as the most direct and accurate method of measuring F_{O3} (Burba, 2013; Clifton et al., 2020; Muller et al., 2009); however, the lack of suitable off-the-shelf instrumentation have led many studies to rely on the alternative approximations.

$$O_3\ v_d = -F_{O_3}/[O_3] \quad (1)$$

First, in the flux-gradient method, F_{O3} is inferred via the vertical gradient in O_3 (or other scalar) mixing ratio scaled by the eddy diffusivity constant (K), where K accounts for the rate of vertical mixing (Businger et al., 1971; Dyer and Hicks, 1970; Webb, 1970) (Eq. 2). The flux-gradient method is based on micrometeorological similarity theory, wherein it is assumed that turbulent eddies carry all atmospheric constituents equally, for example, O_3 and CO_2, such that K determined for one scalar represents that for all scalars, i.e., $K_{O3} = K_{CO2}$ (Oke, 1987). Eq. 2 is an analog of Fick's Law of Diffusion, where vertical transport is caused by the random movement of trace gases by turbulent diffusion along the mixing ratio gradient (Denmead and Bradley, 1985; Denmead, 2008). Molecular movement of any given trace gas follows the direction of high to low concentration of that scalar. Numerous equations have been developed to calculate K from measurements including equations based on momentum fluxes, sensible heat fluxes, friction velocities, and horizontal wind gradients (Denmead and Bradley, 1985; Droppo, 1985; Goldstein et al., 1996; Meredith et al., 2014).

$$F_{O_3} = -K \frac{\partial[\overline{O_3}]}{\partial z} \quad (2)$$

The flux-gradient method requires precise and accurate measurements of O_3 vertical variability, using two analyzers operating simultaneously or one analyzer with a system that either switches between sampling inlets or equipped with device raising and lowering a single inlet, each of which can introduce errors. If using two analyzers, instrumental biases must be carefully accounted for, and if switching between inlets or raising and lowering inlets, measurements are not simultaneous, requiring conditions in which O_3 mixing ratios are not changing rapidly over the measurement cycle (Clifton et al., 2020). Turbulence is influenced by the roughness of the canopy top near the canopy surface, creating wake turbulence and altering the vertical concentration and wind gradients of the atmosphere (Baldocchi et al., 1988; Neirynck et al., 2012; Oke, 1987). Flux-gradient flux observations must therefore be made above this so-called roughness sublayer (Raupach and Legg, 1984). The roughness sublayer scales with canopy height, extending at least twice the height of the vegetation (Baldocchi et al., 1988; Garratt, 1978; Raupach et al., 1980; Simpson et al., 1998) and potentially making measurements prohibitively high over tall canopies. While the flux-gradient method has been shown capture similar fluxes to the eddy covariance method using off-the-shelf instrumentation, there are more micrometeorological requirements, which are frequently violated in the atmosphere (Muller et al., 2009).

Second, the modified Bowen Ratio method, also based on flux-gradient theory, combines the measured flux of a scalar (frequently CO_2) with the O_3 mixing ratio gradient to determine F_{O3} (Eq. 3) (Businger, 1986; Clifton et al., 2020). This method assumes that the diffusivity constant for O_3 is equal to that of a known scalar (x). The modified Bowen Ratio method is infrequently used as it

can give O_3 v_d estimates that are up to two times larger and/or poorly correlated with those based on the eddy covariance technique (Clifton et al., 2020; Wu et al., 2015; Zhu et al., 2020).

$$F_{O_3} = F_x \left(\frac{\partial C_{O3}}{\partial z} \Big/ \frac{\partial C_x}{\partial z} \right) \quad (3)$$

Finally, eddy covariance is a micrometeorological technique based on the principles of mass and momentum conservation. Using micrometeorological assumptions, the turbulent O_3 flux can be derived from the Reynolds-averaged conservation equation (Eq. 4):

$$\frac{\partial O_3}{\partial t} = -\bar{u}\frac{\partial O_3}{\partial x} - \bar{v}\frac{\partial O_3}{\partial y} - \bar{w}\frac{\partial O_3}{\partial z} - \frac{\partial \overline{u'O_3'}}{\partial x} - \frac{\partial \overline{v'O_3'}}{\partial y} - \frac{\partial \overline{w'O_3'}}{\partial z} + S + D \quad (4)$$

where the O_3 rate of change is a function of u, v, and w, which are the longitudinal, lateral, and vertical wind velocities, respectively. S is a chemical source/sink term, and D is the molecular diffusion. By assuming (a) the O_3 mixing ratio is stable over the measurement period ($\frac{\partial O_3}{\partial t} = 0$), (b) there is no horizontal advection and that the surface is level ($\bar{u}\frac{\partial O_3}{\partial x} = \bar{v}\frac{\partial O_3}{\partial y} = \bar{w}\frac{\partial O_3}{\partial z} = 0$), (c) there is no horizontal flux convergence/divergence ($\frac{\partial \overline{u'O_3'}}{\partial x} = \frac{\partial \overline{v'O_3'}}{\partial y} = 0$), (d) molecular diffusion is negligible, and (e) that there is no chemical production and/or loss below the sampling inlet, such that S is equal to the net exchange of the scalar, Eq. 4 simplifies to:

$$\frac{\partial \overline{w'O_3'}}{\partial z} = S \quad (5)$$

Integrating Eq. 5, $F_{O3} = \overline{w'O_3'}$ (Baldocchi et al., 1988; Foken et al., 2012a). Here, F_{O3} is equivalent to the turbulence-driven vertical mass transport of O_3 through a reference layer. In practice, F_{O3} is computed as the product of the deviations from the mean of O_3 mixing ratio and w over an averaging period, typically 30 minutes (Baldocchi et al., 1988; Foken, 2006; McMillen, 1988) (Eq. 6). High-precision, fast-response sensors (sub-second time response) are needed to capture high-

frequency eddy flux contributions within the surface boundary layer. Ranging from the surface to tens of meters, in the surface boundary layer, frequently called the constant flux layer, turbulence transports mass, heat, and momentum and these fluxes are invariable with height. (Foken et al., 2012a; Garratt, 1992). Observations are typically collected atop stationary research towers above plant canopies, where the O_3 sensors are co-located with fast (generally 10 s^{-1}) 3D anemometers.

$$F_{O_3} = \frac{1}{n}\sum_{i=1}^{n}(w_i - \overline{w})\left([O_3]_i - \overline{[O_3]}\right) = \overline{w'\,[O_3]'} \quad (6)$$

Over the past four decades, eddy covariance F_{O3} measurements have focused on forest and grassland canopies (e.g., Bauer et al., 2000; Coe et al., 1995; Fares et al., 2014; Hogg et al., 2007; Horvath et al., 2018; Keronen et al., 2003; Kurpius and Goldstein, 2003; Li et al., 2018; Massman, 1993; Mikkelsen et al., 2000; Muller et al., 2009; Padro, 1996; Plake et al., 2015; Rannik et al., 2012; Turnipseed et al., 2009; Wohlfahrt et al., 2009) and croplands (e.g., Lamaud et al., 2009; Massman, 1995; Padro, 1996; Stella et al., 2012; Wesley et al., 1978; Zhu et al., 2015), with few measurements over water (Bariteau et al., 2010; Fung, 2018; Loades et al., 2020). However, of the 93 sites globally with recorded eddy covariance F_{O3} measurements (as of 2020), only 13% have datasets spanning at least one year (Clifton et al., 2020). Long-term observations are needed to improve modeled estimates, yet sizeable interannual variability (Clifton et al., 2017; Rannik et al., 2012) makes year-long measurements insufficient for model evaluation and land cover type generalizations (Clifton et al., 2020).

Fast-response sensors generally use chemiluminescence detection, measuring the light emission from the reaction between O_3 and a gas, solid (dry), or liquid (wet) reagent. Chemiluminescence is the luminescence from an exoergic chemical reaction, where excited state electrons relax to their

ground state, emitting photons of lower energy than the initial excitation (fluorescence) (Dodeigne et al., 1999). These instruments require high levels of maintenance for continuous operation. Gas-based analyzers are costly to maintain and use nitric oxide or ethene, reagents that are toxic and flammable. Dry chemiluminescence-based instruments are physically small, with low power requirements that require consumable discs of solid dye. While the longevity of these discs has improved (e.g., Zahn et al., 2012), they still rapidly degrade, needing frequent replacement (Clifton et al., 2020). Wet chemiluminescence-based instruments also have low power requirements, but require the constant cycling of a liquid dye, typically using a peristaltic pump, a feature known to fail frequently (Keronen et al., 2003). Each type of instrument counts photons with a photomultiplier tube, regardless of reagent state, requiring some minimal thermal control on the systems.

Here, I discuss eddy covariance data collection and processing of F_{O3}, O_3 v_d, and O_3 mixing ratios in a Central Virginia forest from July 2019–July 2021. I use a wet chemiluminescence analyzer and a 3D sonic anemometer to measure F_{O3} and O_3 v_d and a UV absorption analyzer to measure vertical gradients in O_3 mixing ratios. I describe the measurement location, tower, and laboratory and instrument setup, modifications, and calibration procedures. I provide a spectral analysis of the eddy covariance system to identify systematic errors and calculate random errors both empirically and theoretically. I present two years of O_3 mixing ratios, F_{O3}, and O_3 v_d.

3.2 Methods

3.2.1 Virginia Forest Laboratory, Pace Tower

I collected O_3 eddy covariance and mixing ratio gradient observations at the Virginia Forest Laboratory (VFL) in the forested Piedmont region of Central Virginia near the eastern base of the Blue Ridge Mountains (37.9229°N, 78.2739°W). The canopy is 24-m tall, comprised of mixed deciduous trees with patches of conifer, and is representative of second-growth forests throughout the region. The VFL is dominated by white oak, southern red oak, red maple, Virginia pine, and tulip poplar. The 40-m tall walk-up tower is known as the Pace Tower and the climate-controlled laboratory near the tower base has power supplied by the electrical grid (Figure 3.1). At the 40-m level, a boom extends approximately 3 m out and away from the south side of the platform and supports the F_{O3} sampling inlet and sonic anemometer. Sampling inlets for the O_3 mixing ratio vertical gradient are located at 40 m, 30 m, 20 m, 9 m, and 1 m. The 40-m, 30-m, 20-m, and 9-m inlets extend approximately 0.5 m out from the tower. The 1-m inlet was placed 2 m away from the base of the tower, with all O_3 instrumentation housed in the laboratory.

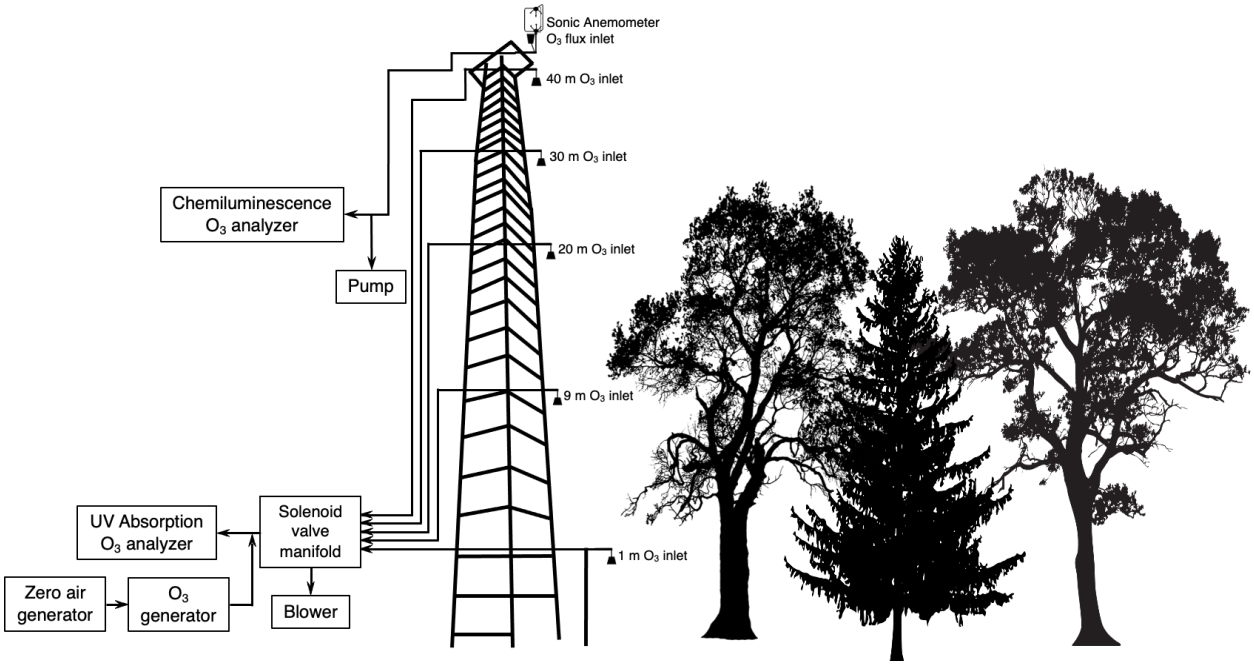

Figure 3.1. Schematic of O_3 flux and gradient inlets and instrumentation. Arrows indicate the direction of the flow. All instrumentation is inside the on-site laboratory (not shown).

3.2.2 Instrumentation

3.2.2.1 Eddy covariance F_{O3}

I measured F_{O3} to the forest canopy with a fast (10 s^{-1}) and precise O_3 system based on the principle of O_3 chemiluminescence with Eosin-Y dye (LOZ-3F, Drummond Technology). In the LOZ-3F flux instrument, ambient air is brought into a reaction chamber containing a fabric wick saturated with an ethylene glycol solution of Eosin-Y dye. A heated solution drier (HSD) removes water from the dye solution. O_3 reacts with Eosin-Y molecules forming an excited state product, which fluoresces, and the emitted red photons are detected using a photomultiplier tube.

The instrument was designed to continuously recirculate the ethylene glycol solution from the supply reservoir using a peristaltic pump system. Because of the failure of this function and the

liquid flow detection system, I modified the instrument such that the liquid dye flowed from a supply reservoir to the detection cell, and then to a second reservoir, without recycling (Figure 3.2). The supply reservoir was a simple inverted, narrow-mouth plastic bottle maintained at atmospheric pressure and connected with PFA tubing to the HSD (0.125 in OD, 0.030 in ID PFA). The height difference between the supply and waste reservoirs served as a coarse flow control. Because Eosin-Y dye is photosensitive, the supply reservoir was surrounded in aluminum foil. For fine control on the speed of the liquid flow and to reduce the frequency of site visits, stainless steel capillaries were installed in the liquid line immediately before the reaction vessel. The wick was replaced once per operational year. Because the ethylene glycol solution polymerizes, slowly creating waxy blockages within the instrument, the HSD, all liquid tubing, and the reservoirs were cleaned as needed. I regularly flushed the inlet to the reaction vessel with an ethylene glycol with 10% alcohol solution to remove dried dye collected on the wick inside the reaction vessel.

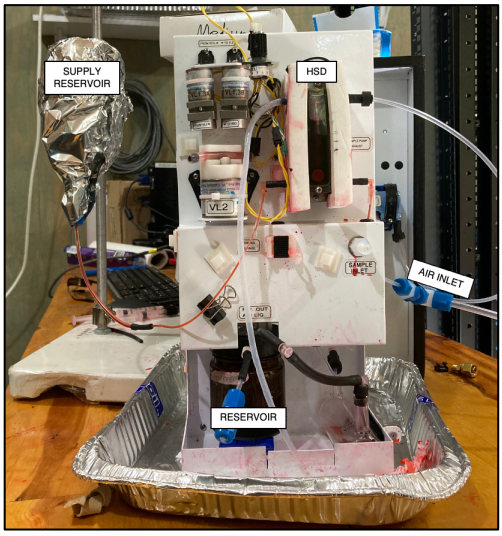

Figure 3.2. Modified LOZ-3F O_3 flux instrument with the supply reservoir, main reservoir, HSD, and air inlet labeled.

A 50-m sample line (0.375 in OD and 0.313 in ID, PFA) running from the 40-m boom arm to the instrument delivered ambient air to the LOZ-3F (Figure 3.3a). A PTFE funnel covered with PTFE mesh (0.045 in x 0.025 in) protected the inlet, keeping it clear of large debris and insects. Particulates were removed with a filter at the inlet (47 mm filter membrane, 1-2 μm, Savillex), replaced annually. A dry scroll pump (nXDS20i, Edwards) pulled air down the sample line at a rate of 30 L min^{-1}, maintaining turbulent flow through the line (RE = 5127) (Lenschow and Raupach, 1991; Leuning and King, 1992). The Reynolds number (RE) is a function of the flow (Q), π, the inner radius of the tubing (r), and the kinematic viscosity of air (v) (Eq. 7). A valved flow meter (EW 32460-50, Cole-Parmer) controlled and monitored the flow rate. Due to problems with the ethylene glycol solution circulating in the wrong direction, I lowered the flow rate to 25 L min^{-1} in March 2021, which still maintained turbulent flow through the line (RE = 4727). A liquid trap (Whatman VACU-GUARD 60 mm disc, 0.45 PTFE housing) protected the dry scroll pump.

$$RE = 2Q/\pi rv \tag{7}$$

To correct for baseline drift in the LOZ-3F signal, the instrument sampled zero air for 30 s once per hour by removing O_3 from ambient air with an internal scrubber. After 15 s, the zero baseline automatically reset, adjusting the O_3 mixing ratio every 1 s to the mean of the preceding 4 s. I corrected additional zero drift over the course of each hour during data processing. The LOZ-3F instrument power supply shut off intermittently. To minimize the resulting data loss, an outlet timer cycled the power to the LOZ-3F at the top of every hour. I discarded the first four minutes of measurements from each hour to eliminate effects of the power cycling. In October 2020, the LOZ-3F internal pump became inconsistent, with periods of no flow. I disassembled and cleaned

the sample pump before replacement in January 2021 and omitted data affected by these pump fluctuations.

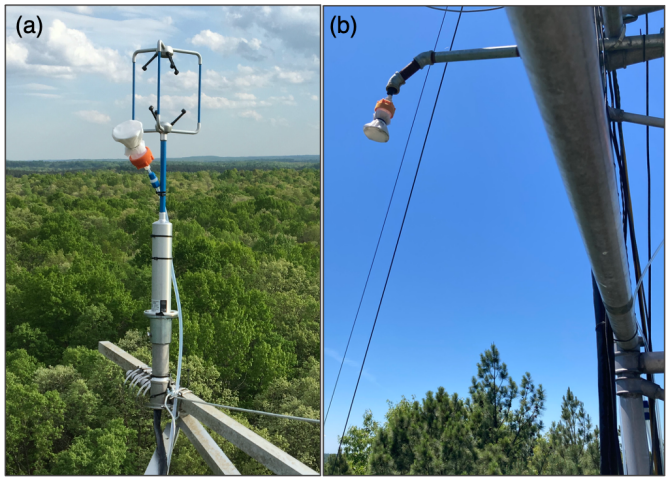

Figure 3.3. 3D sonic anemometer and O_3 flux inlet (a) and 30 m O_3 gradient inlet (b).

3.2.2.2 O_3 mixing ratio observations

I collected an accurate measure of the O_3 mixing ratio using a slower-response (2–60 s) O_3 system based on UV absorption (July–December 2019: T400, Teledyne API, December 2019–January 2020: 202, 2B Technologies, January 2020–July 2021: 205, 2B Technologies). I measured the O_3 mixing ratio vertical gradient at five heights above and within the canopy using the UV O_3 system, co-sampling with the LOZ-3F flux instrument at 40 m for the first 20 minutes of each hour before cycling through the four lower gradient inlets for the remainder of the hour. Each gradient inlet had a PFA sample line (0.375 in OD, 0.313 in ID, PFA) running from the inlet to a solenoid valve manifold. The length of the 30-m, 20-m, 9-m, and 1-m lines matched the length of the 40-m line. PTFE funnels and PTFE mesh (0.045 in x 0.025 in) protected each inlet from large debris and insects (Figure 3.3b). I replaced filters at the inlets (47 mm Filter Membrane, 1-2 μm, Savillex), protecting against particulate contamination, annually. After the first year of operation, I reduced

the sample lines to 0.250 in OD, 0.203 in ID to reduce the residence time in the lines. The sample lines were connected to a manifold of five 3-way solenoid valves (EW-01540-11, Cole-Parmer). Beginning at the top of each hour, measurements were collected at the 40-m inlet for 20 minutes, the 30-m inlet followed by the 20-m inlet for 11 minutes each, and the 9 m inlet followed by the 1-m inlet for 9 minutes in each. A regenerative blower (R2103, Gast) pulled air down the non-active sample lines at approximately 10 L min^{-1}. The gradient instrument was calibrated daily in the field at 2 am local time (LT) using an O_3 generator and zero air generator (146i, ThermoFisher Scientific and T701, Teledyne API, respectively). I applied calibrations during data processing and describe them in Section 3.2.3.1.

3.2.2.3 Three-dimensional winds

Vertical winds were measured at 10 s^{-1} by a Gill WindMaster 3D ultrasonic anemometer. The anemometer was co-located on the boom with the flux inlet (Figure 3.3a).

3.2.2.4 Water vapor

Water vapor concentration (10 s^{-1}) was measured with an open-path infrared absorption sensor (Li7500, LICOR). Vertical winds were measured at 10 s^{-1} by a 3D sonic anemometer (CSAT3, Campbell Scientific). Measurements were made at 32 m.

3.2.3 Data Processing

3.2.3.1 O_3 mixing ratio

I calibrated the UV absorption based O_3 analyzers at 0, 80 and 120 ppb O_3, with known O_3 mixing ratios generated using a 185 nm UV lamp (146i, ThermoFisher Scientific). Each O_3 mixture was

sampled for 20 minutes, discarding the first 5–7 minutes of each calibration step and any data more than three standard deviations from the mean, with a small number of additional outliers removed manually. I fit calibration data using a univariate linear regression, assuming slopes and intercepts drifted linearly between calibrations. Over July 2019–July 2021, mean slope errors were 0.7% and mean intercept errors were 1.3%.

Changes to the calibration schedule and instrumentation occurred throughout the 2-year measurement period. From July 2019–April 2020, O_3-free air was sampled from 2–2:20 am LT, 80 ppb O_3 air was sampled from 2:20–2:40 am LT, and 120 ppb O_3 air was sampled from 2:40–3 am LT. From May 2020–July 2021, the order of the calibration gases rotated on a three-day schedule to determine if the solenoid valves influenced the calibrations. The first day occurred as described previously. On the second day, 80 ppb O_3 air was sampled from 2–2:20 am LT, 120 ppb O_3 air was sampled 2:20–2:40 am LT, and O_3-free air was sampled from 2:40–3 am LT. On the third day, 120 ppb O_3 air was sampled from 2–2:20 am LT, O_3-free air was sampled from 2:20–2:40 am LT, and 80 ppb O_3 air was sampled from 2:40–3 am LT. I observed no influence of the solenoid valves on the calibrations; however, because the O_3-free air mixing ratio step did not stabilize during their 20-minute periods when the second and third-day patterns were used, I applied only calibrations using the first day pattern during this time period. In January 2020, the removal of the T400 Teledyne API instrument caused the 205 2B Technologies instrument to receive a higher air flow from the O_3 generator, over pressurizing the instrument and inducing an oscillatory pattern with uncharacteristically low data points during the 80 ppb O_3 and 120 ppb O_3 steps. Further testing demonstrated that over pressurizing the instrument while sampling 80 ppb or 120 ppb of O_3 depressed the instrument signal response. As a result, I removed the lowest points in each oscillation from the sensitivity calculations (28 January 2020–July 2021). I omitted

calibrations from 13 April–23 May 2020 due to the malfunctioning of the zero air generator. I filled the calibration gap linearly using the seven nearest preceding and following calibrations. In 2021, the O_3-free calibration gas step became unsteady and thus I excluded it from sensitivity calculations. Therefore, all calibrations applied in 2021 are 2-point calibrations using 80 ppb O_3 and 120 ppb O_3. For reference, a 2-point calibration using 80 ppb O_3 and 120 ppb O_3 applied to the 2020 O_3 mixing ratios, elevates observations by 6–12%.

I processed gradient mixing ratio data as follows. To avoid lingering effects from the calibration gas, I removed the 20 minutes following each calibration (3–3:20 am LT). Due to frequent spurious readings from the T400 Teledyne API, I despiked data from 18 September–7 December 2019 based on the median absolute deviation, where if the difference between the measured value and a calculated running median exceeds a set threshold, then the value is considered an outlier (Mauder et al., 2013). I applied the despiking method twice, first to remove the most extreme outliers, using a 5-min running median and set threshold of 4 ppb, and again to remove remaining outliers, using a 15-min running median and set threshold of 4 ppb. I averaged each gradient height hourly.

3.2.3.2 Eddy covariance F_{O3} and O_3 v_d

I corrected the fast LOZ-3F O_3 data based on an absolute standard, the hourly 40-m O_3 gradient, and the hourly zero baseline drift. To scale F_{O3}, I filled gaps of 1–3 h in the 40-m O_3 mixing ratio data via linear interpolation. I did not fill gaps longer than 3 h. Post gap-filling, if no 40-m O_3 mixing ratio existed during an hour of operation of the LOZ-3F, I omitted that hour of flux. While the instrument resets its internal zero once per hour, as described in Section 3.2.2.1, baseline drift occurs over the course of the hour, thus I corrected data based on the assumption that the instrument

drifted steadily and linearly throughout the hour. If no zero ran within 1 h of the flux period, I omitted the period from further analysis. I subtracted the zero drift (C_{drift}) from the fast data (C_{fast}). I then corrected the fast data based on the hourly mean of the accurate slow 40-m O_3 mixing ratios (C_{slow}) using the ratio of the hourly mean slow O_3 to the hourly mean fast O_3 as a correction factor (Muller et al., 2009; Zhu et al., 2015), where the corrected fast mixing ratio is defined according to Eq. 8.

$$\text{Corrected fast } O_{3_i} = \frac{\overline{C_{slow}}}{\overline{C_{fast} - C_{drift}}} \left(C_{fast_I} - C_{drift_i} \right) \tag{8}$$

I rotated wind component vectors using the natural wind coordinate (Lee et al., 2015). To minimize the effects of spurious instrumental errors, I despiked data using the median absolute deviation method (Mauder et al., 2013), described in Section 3.2.3.1. Removing values whose difference from the 30-min median exceeded a set threshold of 3 ppb eliminated outliers while maintaining natural fluctuations in the measurement. I detrended based on the mean of the measurement period. To correct for sensor time lag between the O_3 and wind measurements, I calculated the covariance across a lag window of –20 s to 0 s, centered on –10 s, and identified the lag producing the maximum covariance (Figure 3.4). The lag is a function of the distance between the inlet and the sonic anemometer, tubing length, and flow rate. The mean lag was –7.9 ± 2.3 s with the error as the standard deviation. If the lag fell outside of one standard deviation of the mean, I set the lag to –7.9 s (July 2019–February 2021). Due to reduced flow, from March–July 2021, the mean lag was –10.3 ± 2.1 s and if outside of one standard deviation of the mean, I set the lag to –10.3 s.

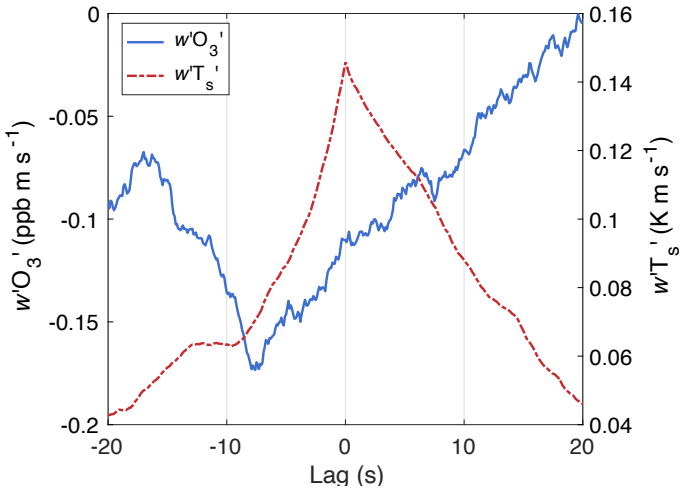

Figure 3.4. Sample lag time from 8 August 2020 at 2:30 pm LT for w with O_3 (blue solid line) and T_s (red dashed line). The maximum covariance of w'O_3' occurs at a –7.6 s lag. The maximum covariance of w'T_s' occurs at a lag of 0 s.

Using the corrected LOZ-3F O_3 and w, I calculated eddy covariance fluxes using Reynolds averaging over 30-min periods of 10 Hz measurements (Eq. 6). The 30-min averaging period and fast response instruments allow fluxes to include both high- and low-frequency eddies. Further analysis of averaging period is discussed in Section 3.2.3.3. To meet eddy covariance stationarity requirements, I calculated the covariances of five 6-min sub-samples for each measurement period and compared them to the mean over the measurement period. If the 6-min covariance deviated from the mean by ±30%, I omitted that measurement period (Foken and Wichura, 1996). F_{O3} showed no u_* dependence, thus a u_* filter was not applied.

3.2.3.3 Cospectral analysis and systematic errors

I applied F_{O3} corrections to account for spectral and systematic errors. The two Webb, Pearman, and Leuning (WPL) corrections account for fluctuations in water vapor and temperature that lead to fluctuations in O_3 unassociated with F_{O3} (Eq. 9) (Webb et al., 1980). Due to the length and size of the tubing, the temperature fluctuations in the tubing were dampened, thus I did not apply a

temperature correction (Ibrom et al., 2007; Keronen et al., 2003; Rannik et al., 1997; Zhu et al., 2015). I applied the water vapor correction to F_{O3} and is a function of the ratio of the molar mass of dry air and water vapor (μ), the density of the scalar (ρ_c), the density of dry air (ρ_d), and the density of water vapor (ρ_v). The mean WPL correction was 2.1% of F_{O3}. While this correction is generally not applied to mixing ratios (e.g., Zona et al., 2014), as mixing ratios are independent of air density, certain literature still applies it (e.g., Keronen et al., 2003). This correction will be revisted when this work is submitted for publication.

$$F_{c\,\text{corrected}} = \overline{w'\rho_c'} + \mu\left(\bar{\rho}_c/\bar{\rho}_d\right)\overline{w'\rho_v'} \tag{9}$$

Cospectral analysis of the scalar flux and an ideal flux are typically used to determine if sampling procedures appropriately capture the scalar flux. Cospectral analyses demonstrate if both low and high frequency eddies are captured, if measurement periods are of sufficient length, and if all eddies are fully sampled. Cospectral features may indicate over- or underestimations of the flux. The buoyancy flux, the mean covariance between sonic temperature (T_s) and *w,* served as the ideal flux and cospectra for comparison with the F_{O3} cospectra. As with F_{O3}, if the calculated lag between maximum T_s and *w* covariance fell outside of one standard deviation of the mean (±2 s), I set the lag to the mean, 0 s. I applied stationarity criteria described above.

Cumulative distribution plots, or ogives, demonstrate the cumulative contribution of each frequency to the flux. I show representative ogives in Figure 3.5 and observe similar features described here across the 2-year measurement period. The *w*'O_3' and *w*'T_s' ogives reach asymptotes at the high frequency end, demonstrating that sampling occurred fast enough. Asymptotes at low frequency end indicate sufficiently long averaging periods. The low frequency end approaches an asymptote and an assessment of 1-h averaging periods showed no significant

difference in the calculated flux or flux contribution, thus I determined 30-minute periods were sufficiently long.

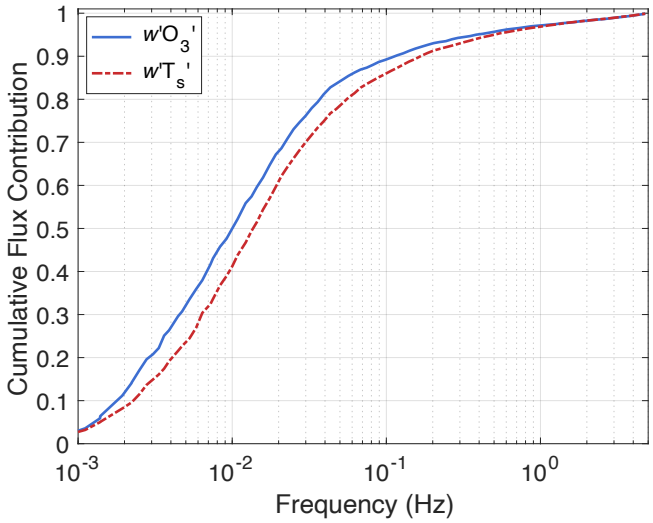

Figure 3.5. Average ogive for half-hour measurement periods from 1–3:30 pm LT June–August 2020 for w'O_3' (blue solid line) and w'T_s' (red dashed line). Cospectra are averaged into 100 equally spaced bins across the logarithmic frequency axis.

Cospectral density figures demonstrate measurements are within the inertial subrange and the frequencies contributing to the flux. Figure 3.6 shows an averaged cospectra of summertime afternoon hours when conditions are unstable ($z/L < -0.5$, z is the measurement height and L is the Obukhov length). Cospectra are variable, thus I averaged them over multiple measurement periods to observe representative trends, rather than artifacts of individual cospectrum. Theory predicts cospectral decay along a –4/3 slope in non-dimensional normalized frequency space ($n = fz/U$), a function of frequency (f), measurement height (z), and mean wind speed (U). This slope is interpreted to mean measurements capture the inertial subrange. While the slope does not exactly follow the expected decay from the ideal proposed by Kaimal et al. (1972), cospectra in forested sites deviate from model cospectra, due to their tall and irregular surfaces (Amiro, 1990; De Linge

et al., 2010). Measuring in the inertial subrange captures turbulent eddies, in the form of energy cascades, rather than energy production or dissipation (Foken et al., 2012a). The w'O_3' and w'T_s' cospectra peak at similar frequencies, corresponding to eddies of 50–100 s (150–300 m at 3 m s^{-1} wind speed) (Figure 3.7). Flux-containing eddies of 10–200 s are typical in forest canopies due to the coherent structures driving turbulent transport (Turnipseed et al., 2006). The w'O_3' ogive and frequency-weighted cospectrum (Figure 3.5 & Figure 3.7) shift toward lower frequencies than the w'T_s' cospectra, indicating that the lower frequencies contribute more to the F_{O3} than the buoyancy flux, a common sign of high frequency spectral attenuation in closed-path systems (Foken et al., 2012b).

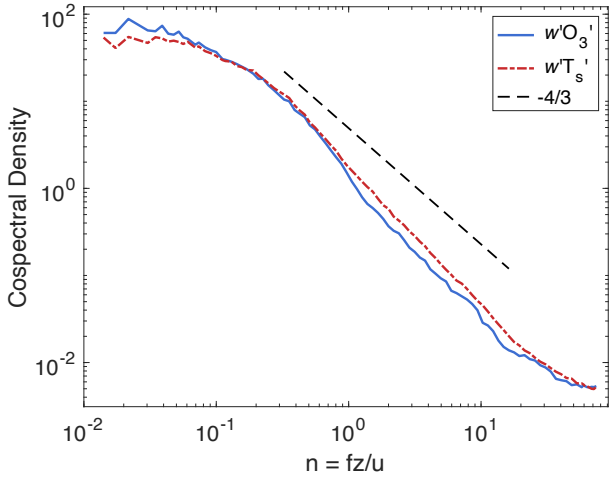

Figure 3.6. Averaged cospectral density function for w'O_3' (blue solid line) and w'T_s' (red dashed line) from 1–3:30 pm LT June–August 2020 when conditions are unstable. Cospectra are averaged into 100 equally spaced bins across the logarithmic frequency axis. The –4/3 line (black dashed line) represents the expected slope for the inertial subrange.

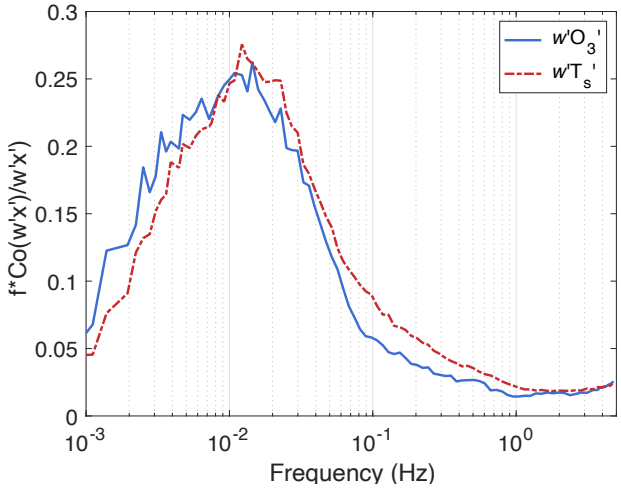

Figure 3.7. Averaged frequency weighted normalized cospectra for w'O_3' (blue solid line) and w'T_s' (red dashed line). Averaged across 1–3:30 pm LT June–August 2020 when conditions are unstable. Cospectra are averaged into 100 equally spaced bins across the logarithmic frequency axis.

High frequency attenuation, a systematic error, is the attenuation of measured covariance at high frequencies due to dampening in the inlet, sensor separation, and instrument response time (Aubinet et al., 2000; Farmer et al., 2006). Attenuation can be accounted and corrected for using modeled transfer functions or a low pass filter. First, using transfer functions, error due to inlet dampening depends on tubing radius (r), tubing length (L), air speed (q), and the molecular diffusivity of O_3 (D) (Eq. 10), error due to separation of the inlets depends on frequency (f), distance between inlets (s), and wind speed (U) (Eq. 11), and error due to instrument response time depends on the instrument time constant (τ_c) and frequency (f) (Eq. 12). Here, the mean error due to attenuation ranged from –11.1–7.5% F_{O3}, mean error due to inlet separation ranged from –3.8–3.2% F_{O3}, and mean error due to instrument response time ranged from –12.0–7.6% F_{O3}. Summing the three high frequency attenuation errors in quadrature gives a total error of –26.9–18.3%. These functions perform better over shorter vegetation and assume all tubing is straight and horizontal (Foken et al., 2012b).

$$T(f) = \exp\left\{-\frac{\pi^2 r^2 f^2 L}{12Dq}\right\} \tag{10}$$

$$T(f) = \exp\left\{-9.9\left(\frac{fs}{U}\right)^{1.5}\right\} \tag{11}$$

$$T(f) = \frac{1}{1+(2\pi f\tau_c)^2} \tag{12}$$

The second method, a low-pass filter, leverages similarities between frequency normalized cospectra of the scalar flux and ideal flux, based on the Monin-Obukhov similarity theory (Aubinet et al., 2000; Geddes and Murphy, 2014). Following this method, I assessed monthly averaged frequency weighted normalized cospectra of w'O_3' and w'T_s'. I observed, in both stable and unstable conditions, the w'O_3' cospectral power at decreased at 0.028 Hz, relative to the w'T_s' cospectral power. I corrected F_{O3} following Eq. 5 based on Geddes and Murphy (2014):

$$w'O_3'_{corr} = \int_0^{0.028\ Hz} Co_{w'O_3'} \frac{w'T_s'_{meas}}{\int_0^{0.028\ Hz} Co_{w'T_s'}} \tag{13}$$

where w'O_3'$_{corr}$ is the corrected covariance. Following this calculation, the mean correction applied to F_{O3} ranged from –26.9–29.6% F_{O3}. If the correction factor, defined as the ratio of the corrected to calculated flux, was greater than four, I removed that measurement period from the analysis because it indicates less than one third of the power spectrum was measured in that flux period (Sabbatini et al., 2018).

3.3 Results and Discussion

3.3.1 Eddy covariance random errors

The accuracy of F_{O3} depends on the accuracy of the 40-m O_3 mixing ratio and systematic errors and the precision of F_{O3} is dependent on random errors. I discuss error in the O_3 mixing ratio dataset in section 3.2.3.1 and O_3 v_d is independent of O_3 mixing ratio (Eq. 6), thus is not dependent on measurement accuracy and systematic errors discussed in section 3.2.3.3. Random errors in F_{O3} are a function of instrument noise and the stochastic nature of turbulence. I estimated instrument noise, encompassing all noise within the instrument system, empirically and theoretically. For the empirical calculation, I ran a sampling line (0.375 in OD, 0.313 in ID PFA) from the VFL laboratory to the 40-m flux inlet at the end of the boom arm and sampled O_3-free air through the full inlet system for two hours, or four 30-minute flux measurement periods, following Farmer et al. (2006). I calculated the so-called 'zero flux' according to the eddy covariance procedure described above. From these four measurement periods, I used the zero flux with the largest magnitude for the error calculation, leading to a mean flux due to instrument noise of 3.4% F_{O3}, and indicating minimal interference. I calculated the contribution of instrument noise to the flux theoretically following Lenschow et al. (2000) and used by Mauder et al. (2013) and Peltola et al. (2014):

$$\sigma^2_{\text{inst. noise}} = C_{11}(0) - C_{11}(p \rightarrow 0) \quad (14)$$

where p is the lag, $C_{11}(0)$ is the observed variance of the timeseries at lag zero, and $C_{11}(p \rightarrow 0)$ is the autocovariance function extrapolated to zero. Then, I calculated the instrument noise of the

covariance of [O_3] and w through error propagation (Eq. 7 in Mauder et al., 2013 and Eq. 9 in Peltola et al., 2014):

$$\sigma_{\text{inst. noise}} = \sqrt{\frac{1}{n} \cdot \sigma^2_{\text{inst. noise}} \cdot \sigma^2_w} \tag{15}$$

where n is the number of observations and σ^2_w is the variance in the vertical winds, leading to a mean instrument noise of 8.8% of F_{O3}. The relatively small theoretical instrument noise indicated instrument noise did not dominate the flux precision.

I calculated random errors due to turbulence using two different methods. First, following Finkelstein and Sims (2001):

$$\sigma_{\overline{w'[O_3]'}} = \sqrt{\frac{1}{n} \sum_{p=-m}^{m} \left(\overline{w'w'}(p) \cdot \overline{[O_3]'[O_3]'}(p) \cdot \overline{w'[O_3]'}(p) \cdot \overline{[O_3]'w'}(p) \right)} \tag{16}$$

where n is the number of observations, p is the lag, and the number of samples, m, is sufficiently large to capture the integral time scales, leading to a random error of 14.1%. Second, following the limit-of-detection method described by Vermeuel et al. (2021) using the standard deviation of the covariances. I calculated the standard deviation using the outer 20 points of a 400-point window, a time when O_3 and w do not co-vary, centered on the lag with the maximum covariance, scaled by 1.96 to calculate the uncertainty at the 95% confidence interval. Using this method, the mean random error over the 2-year measurement period is 29.1%. Because the two sources of random errors, instrument noise and stochastic turbulence are independent, the total random error is equal to the individual errors added in quadrature and because the Lenschow et al. (2000) and

Vermeuel et al. (2021) methods produced the largest error, I calculate the total random error using these two methods. I find the total random error is 30.4% F_{O3}.

3.3.2 O_3 mixing ratios

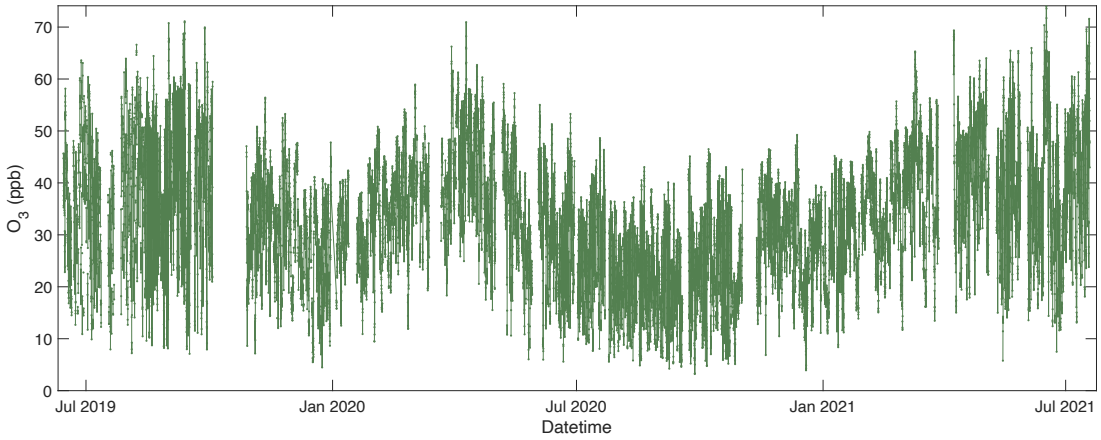

Figure 3.8. July 2019–July 2021 hourly mean 40-m O_3 mixing ratios (ppb).

I observe strong seasonal and diurnal patterns in O_3 at the VFL, with the highest mixing ratios in the spring and summer months (Figures 3.8–3.9). I define winter as December–February, spring as March–May, summer as June–August, and fall as September–November. I generally measure the highest 40-m O_3 mixing ratios in April, with a mean daily maximum of 54 ± 6 ppb, where variability is one standard deviation. While the mixing ratios are highest in the spring, the diurnal pattern is most pronounced in the summer and the fall. In the winter months, the nighttime decrease in O_3 mixing ratio is much smaller than in the summer or fall. The mean daily maximum O_3 and standard deviation in the winter is 38 ± 7 ppb, in the spring is 50 ± 9 ppb, in the summer is 45 ± 12 ppb, and in the fall is 41 ± 11 ppb. The mean daily minimum O_3 and standard deviation in the winter is 22 ± 8 ppb, in the spring is 27 ± 9 ppb, in the summer is 17 ± 8 ppb, and in the fall is 17 ± 9 ppb. In the spring, as sunlight increases, O_3 production increases, but the forest has not yet

leafed out and thus O_3 loss remains low. This allows for more O_3 accumulation, thus higher mixing ratios in the spring. In the summer and fall, more O_3 is lost deposition, so while sunny conditions still contribute to O_3 production, loss rates are also higher, resulting in lower mixing ratios. O_3 peaks daily between 12–5 pm LT, depending on the season. There is a time-of-day shift in the diurnal patterns with the seasons. In the winter, O_3 peaks at 3 pm LT. In the spring, O_3 peaks at 4 pm LT. In the summer, O_3 peaks at 2 pm LT. In the fall, O_3 peaks at 3 pm LT. In the spring and summer, O_3 begins increasing for the day between 7 and 8 am LT, while in the fall and winter, O_3 does not begin to increase until 9 am and 10 am LT, respectively.

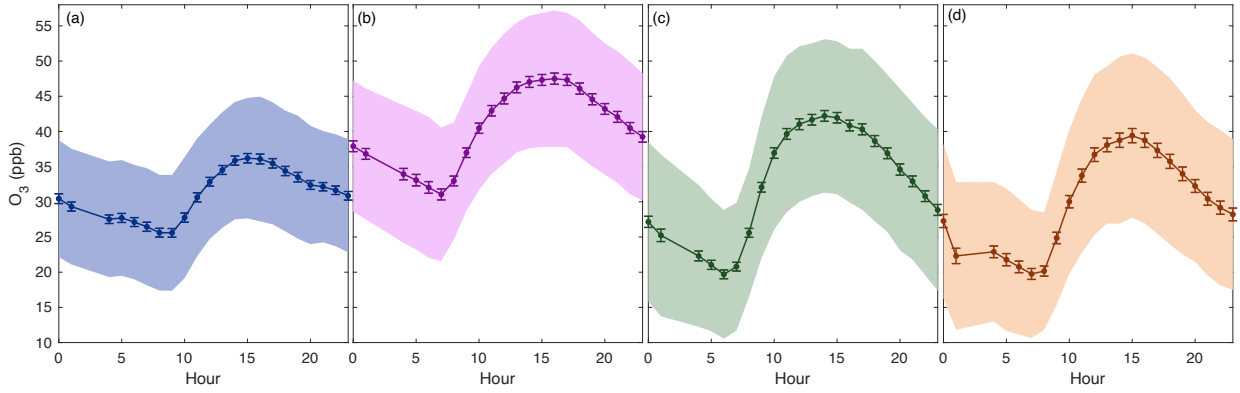

Figure 3.9. Seasonal diurnal 40 m O_3 mixing ratios at the Virginia Forest Laboratory from July 2019–July 2021 for (a) winter, (b) spring, (c) summer, and (d) fall. Shading represents one standard deviation and error bars represent standard error of the mean.

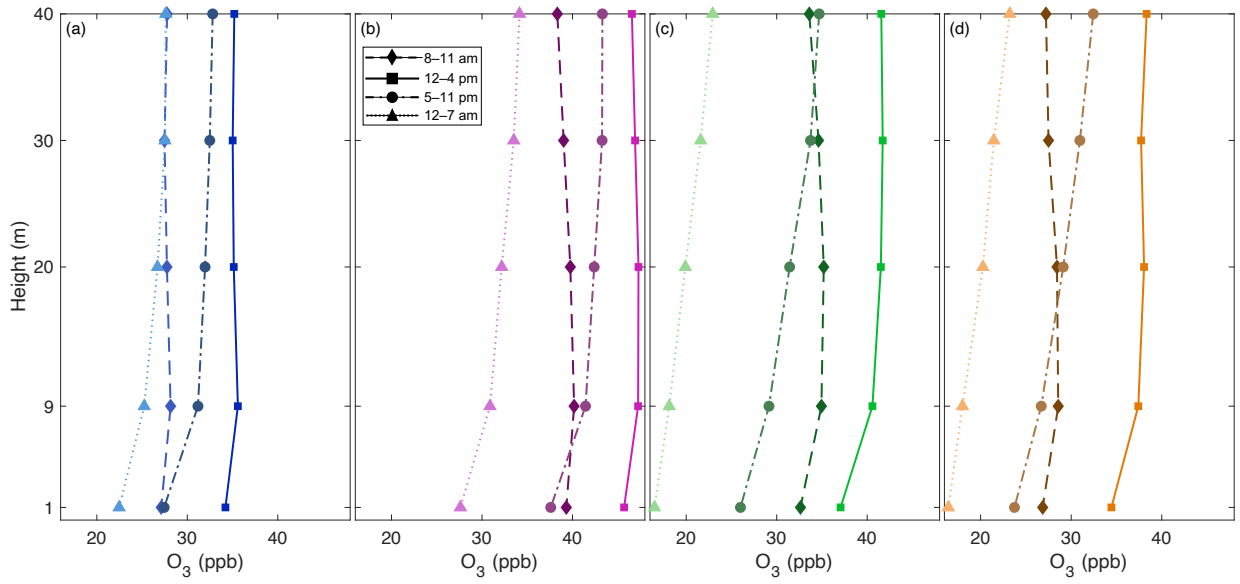

Figure 3.10. Seasonal vertical O_3 gradients (ppb) at the Virginia Forest Laboratory from July 2019–July 2021 for winter (a), spring (b), summer (c), and fall (d). Dashed lines with diamonds morning gradients (8–11 am LT averages), solid lines with squares are mid-day gradients (12–4 pm LT averages), dash-dotted lines with circles are evening gradients (5–11 pm LT averages), and dotted lines with triangles are overnight (12–7 am LT averages).

The vertical O_3 gradient demonstrates O_3 loss throughout the forest canopy. I observe O_3 mixing ratios decrease from above the canopy to within the forest. (Figure 3.10). I find the steepest vertical gradients in the evening and overnight hours. In the winter, the changes to the gradient shape throughout the day are minor compared to the changing gradient shape in spring through fall. Low overnight O_3 spring through fall indicates the important role of LO_3 at the VFL. The steep overnight gradient demonstrates that LO_3 within the canopy, particularly in the lower layers, is strong.

3.3.3 F_{O3} and O_3 v_d measurements

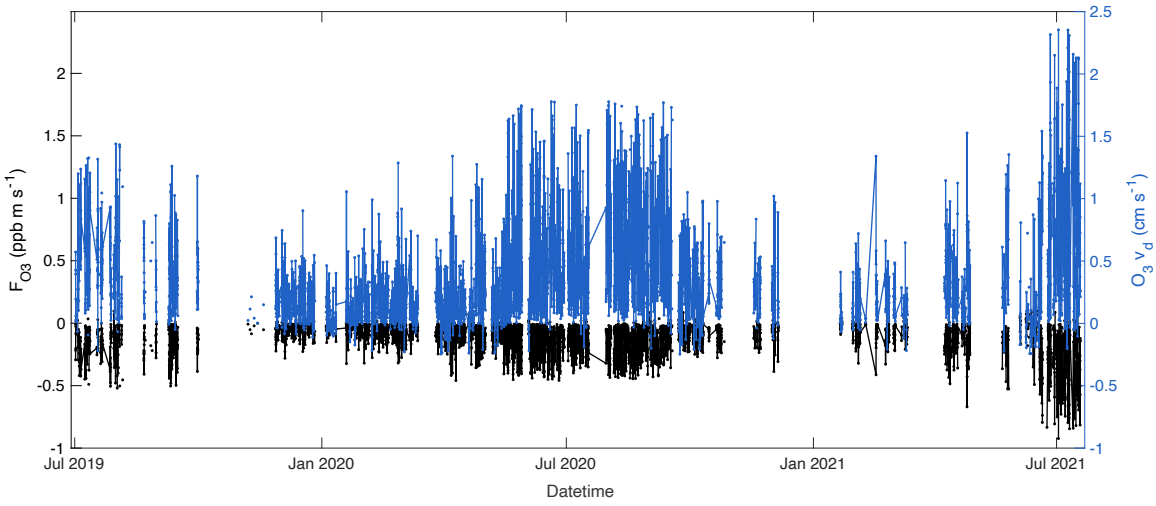

Figure 3.11. July 2019 – July 2021 F_{O3} (ppb m s^{-1}) (black) and O_3 v_d (cm s^{-1}) (blue).

F_{O3} and O_3 v_d follow similar seasonal patterns to the O_3 mixing ratio, peaking in the summer months (Figures 3.11–3.12). F_{O3} and O_3 v_d are minimal from October–March, before starting to increase in April. From May–September (the growing season), O_3 v_d begins increasing in the early morning hours before reaching an early–mid morning peak. F_{O3}, influenced by the O_3 mixing ratio diurnal pattern, rises less steeply than the O_3 v_d and typically peaks late morning. Both O_3 v_d and F_{O3} maintain near-peak values for 8–10 h before declining mid- to late-afternoon, with the longest periods of sustained high O_3 v_d occurring in the summer months. O_3 v_d frequently reaches its daily maximum 1–3 h before F_{O3}. During the growing season, peak O_3 v_d occurs 2–3 h before peak F_{O3}, while in the non-growing season, F_{O3} and O_3 v_d typically peak within 1 h of one another. Regardless of season, both O_3 v_d and F_{O3} are at minimums in the evening and/or overnight.

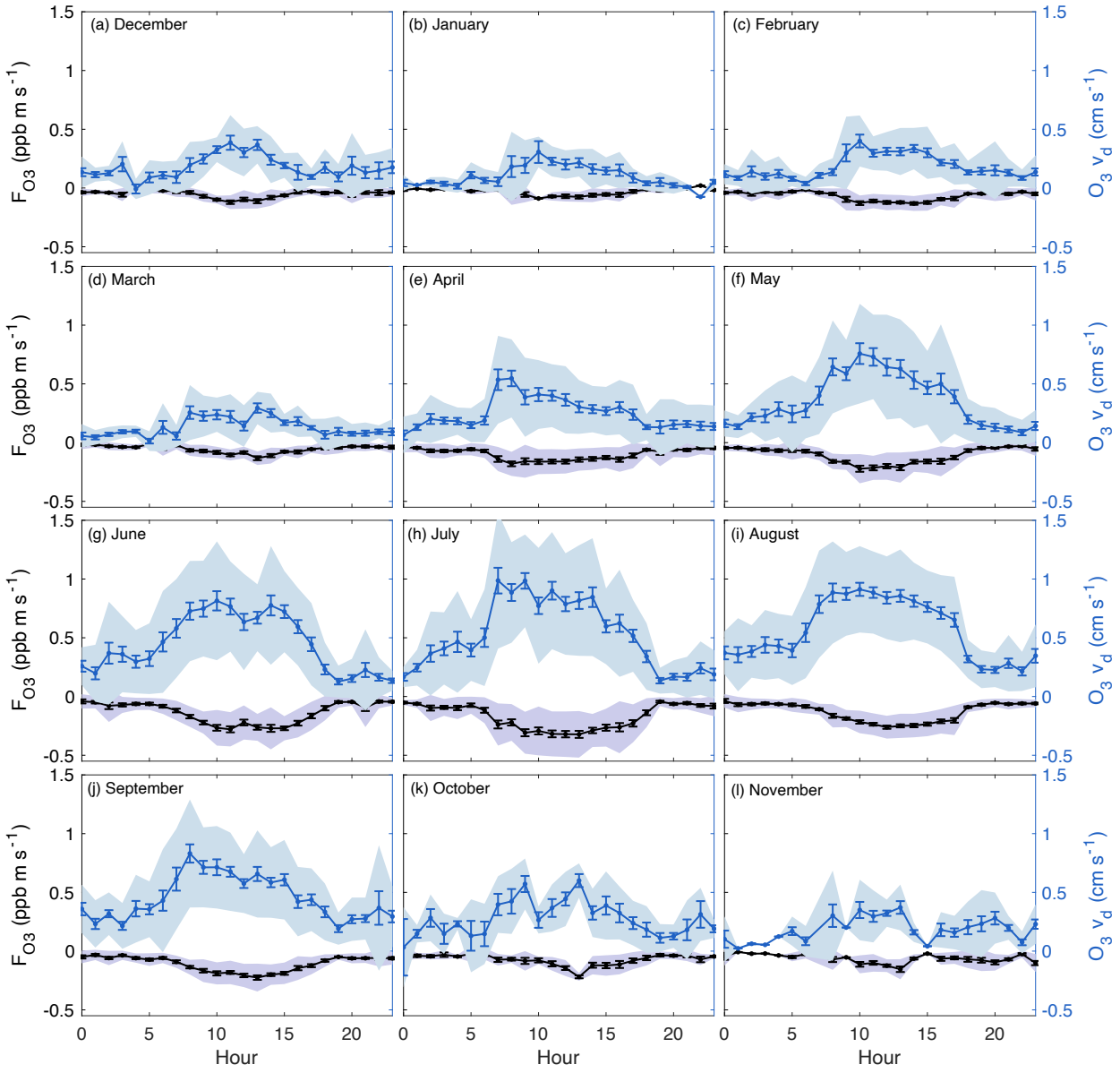

Figure 3.12. Monthly diurnal F_{O3} (ppb m s^{-1}) (black with purple shading) and O_3 v_d (cm s^{-1}) (blue with light blue shading) at the Pace tower from July 2019–July 2021. Shading represents one standard deviation and error bars represent standard error of the mean.

I observe the highest O_3 v_d in the summer, with a mean maximum of 0.9 cm s^{-1}. Similarly, peak F_{O3} occurs in the summer, with a mean maximum of –0.3 ppb m s^{-1}. In other forested environments, O_3 v_d and F_{O3} peak during the growing season, with measured mean summertime O_3 v_d ranging from 0.5–1.6 cm s^{-1} and mean summertime F_{O3} ranging from –0.62 to –0.15 ppb m

s^{-1} (Bauer et al., 2000; Fares et al., 2014; Hogg et al., 2007; Keronen et al., 2003; Kurpius and Goldstein, 2003; Mikkelsen et al., 2000; Padro, 1996; Rannik et al., 2012; Turnipseed et al., 2009; Vermeuel et al., 2021; Zona et al., 2014). At the VFL, the magnitude of F_{O3} increases with ambient O_3 in the winter, summer, and fall, but in the spring, when O_3 is the highest, F_{O3} decreases with O_3. O_3 v_d decreases with O_3 across all seasons. The O_3 v_d-O_3 trends are strongest spring through fall. In the winter, the relationship is present, but comparatively minor.

3.4 Conclusions

I measured F_{O3} and O_3 v_d using the eddy covariance technique with a fast chemiluminescence LOZ-3F O_3 instrument and largely routinized instrument operation. For long-term operation, the instrument required semi-frequent checks on air and liquid flow cycling and recycling of the dye. Use of a slower UV absorption O_3 analyzer is required to calibrate the LOZ-3F analyzer. While instrument down time accounts for both long and short gaps in the F_{O3} and O_3 v_d time series, I present one of few datasets that extends for a 2-year period and the only, to my knowledge, for a natural forest in the Southeast U.S. I applied a correction for high frequency spectral attenuation, ranging from –26.9–29.6%, caused by the closed-path system, long tubing, and physical separation of sensors. I report the total random error, due to instrument noise and the stochastic turbulence, of 30.4% as an uncertainty. These are on par with those of previous field campaigns, with reported systematic errors ranging from 16–22% F_{O3} and random error ranging from 20–22% F_{O3} (Bauer et al., 2000; Keronen et al., 2003; Vermeuel et al., 2021). O_3 mixing ratios are highest at the VFL in the spring, followed by the summer, as conditions promote O_3 production, but O_3 loss remains low. Growing season conditions promote significant O_3 v_d at the VFL, with half-hourly averages

frequently ranging 1–1.5 cm s^{-1}. In the following chapter of this dissertation, I further discuss LO_3 patterns, plant-O_3 uptake pathways, and environmental drivers of deposition.

References

Amiro, B. D.: Comparison of turbulence statistics within three boreal forest canopies, Boundary-Layer Meteorology, 51, 99-121, 1990.

Aubinet, M., Grelle, A., Ibrom, A., Rannik, U., Moncrieff, J., Foken, T., Kowalski, A. S., Martin, P. H., Berbigier, P., Bernhofer, C., Clement, R., Elbers, J., Granier, A., Grunwald, T., Morgenstern, K., Pilegaard, K., Rebmann, C., Snijders, W., Valentini, R., and Vesala, T.: Estimates of the annual net carbon and water exchange of forests: The EUROFLUX methodology, Advances in Ecological Research, 30, 113-175, 2000.

Baldocchi, D. D., Hicks, B. B., and Meyers, T. P.: Measuring biosphere-atmosphere exchanges of biologically related gases with micrometeorological methods, Ecology, 69, 1331-1340, 1988.

Bariteau, L., Helmig, D., Fairall, C. W., Hare, J. E., Hueber, J., and Lang, E. K.: Determination of oceanic ozone deposition by ship-borne eddy covariance flux measurements, Atmospheric Measurement Techniques, 3, 441-455, 2010.

Bauer, M. R., Hultman, N. E., Panek, J. A., and Goldstein, A. H.: Ozone deposition to a ponderosa pine plantation in the Sierra Nevada Mountains (CA): A comparison of two different climatic years, Journal of Geophysical Research, 105, 22123-22136, 2000.

Burba, G.: Eddy Covariance Method for Scientific, Industrial, Agricultural, and Regulatory Applications, LI-COR Bioscience, Lincoln, Nebraska, 2013.

Businger, J. A., Wyngaard, J. C., Izumi, Y., and Bradley, E. F.: Flux-Profile Relationships in the Atmospheric Surface Layer, Journal of the Atmospheric Sciences, 28, 181-189, 1971.

Businger, J. A.: Evaluation of the Accuracy with Which Dry Deposition Can Be Measured with Current Micrometeorological Techniques, Journal of Climate and Applied Meteorology, 25, 1100-1124, 10.1175/1520-0450(1986)025<1100:Eotaww>2.0.Co;2, 1986.

Clifton, O. E., Fiore, A. M., Munger, J. W., Malyshev, S., Horowitz, L. W., Shevliakova, E., Paulot, F., Murray, L. T., and Griffin, K. L.: Interannual variability in ozone removal by a temperate deciduous forest, Geophysical Research Letters, 44, 542-552, 10.1002/2016gl070923, 2017.

Clifton, O. E., Fiore, A. M., Massman, W. J., Baublitz, C. B., Coyle, M., Emberson, L., Fares, S., Farmer, D. K., Gentine, P., Gerosa, G., Guenther, A. B., Helmig, D., Lombardozzi, D. L., Munger, J. W., Patton, E. G., Pusede, S. E., Schwede, D. B., Silva, S. J., Sörgel, M., Steiner, A. L., and Tai, A. P. K.: Dry Deposition of Ozone over Land: Processes, Measurement, and Modeling, Reviews of Geophysics, 58, 10.1029/2019RG000670, 2020.

Coe, H., Gallagher, M. W., Choularton, T. W., and Dore, C.: Canopy scale measurements of stomatal and cuticular O_3 uptake by sitka spruce, Atmospheric Environment, 29, 1413-1423, 1995.

De Linge, A., Heinesch, B., and Aubinet, M.: New transfer functions for correcting turbulent water vapour fluxes, Boundary-Layer Meteorology, 137, 205-221, 10.1007/s10546-010-9525-9, 2010.

Denmead, O. T., and Bradley, E. F.: Flux-gradient relationships in a forest canopy, in: The Forest-Atmosphere Interaction, Springer, Dordrecht, 1985.

Denmead, O. T.: Approaches to measuring fluxes of methane and nitrous oxide between landscapes and the atmosphere, Plant and Soil, 309, 5-24, 10.1007/s11104-008-9599-z, 2008.

Dodeigne, C., Thunus, L., and Lejeune, R.: Chemiluminescence as diagnostic tool. A review, Talanta, 51, 415-439, 10.1016/s0039-9140(99)00294-5, 1999.

Droppo, J. G.: Concurrent measurements of ozone dry deposition using eddy correlation and profile flux methods, Journal of Geophysical Research, 90, 2111-2118, 1985.

Dyer, A. J., and Hicks, B. B.: Flux-gradient relationships in the constant flux layer, Quarterly Journal of the Royal Meteorological Society, 96, 715-+, 10.1002/qj.49709641012, 1970.

Fares, S., Savi, F., Muller, J., Matteucci, G., and Paoletti, E.: Simultaneous measurements of above and below canopy ozone fluxes help partitioning ozone deposition between its various sinks in a Mediterranean Oak Forest, Agricultural and Forest Meteorology, 198-199, 181-191, 10.1016/j.agrformet.2014.08.014, 2014.

Farmer, D. K., Wooldridge, P. J., and Cohen, R. C.: Application of thermal-dissociation laser induced fluorescence (TD-LIF) to measurement of HNO_3, Σalkyl nitrates, Σperoxy nitrates, and NO_2 fluxes using eddy covariance, Atmospheric Chemistry and Physics, 6, 3471-3486, 2006.

Finkelstein, P. L., and Sims, P. F.: Sampling error in eddy correlation flux measurements, Journal of Geophysical Research, 106, 3503-3509, 2001.

Foken, T., and Wichura, B.: Tools for quality assessment of surface-based flux measurements, Agricultural and Forest Meteorology, 78, 1996.

Foken, T.: 50 Years of the Monin–Obukhov Similarity Theory, Boundary-Layer Meteorology, 119, 431-447, 10.1007/s10546-006-9048-6, 2006.

Foken, T., Aubinet, M., and Leuning, R.: The Eddy Covariance Method, in: Eddy Covariance: A Practical Guide to Measurement and Data Analysis, edited by: Aubinet, M., Vesala, T., and Papale, D., Springer, Dordrecht, 1-20, 2012a.

Foken, T., Leuning, R., Oncley, S. R., Mauder, M., and Aubinet, M.: Corrections and Data Quality Control, in: The Eddy Covariance Method, edited by: Aubinet, M., Vesala, T., and Papale, D., Springer, Dordrecht, 85-131, 2012b.

Fowler, D., Pilegaard, K., Sutton, M. A., Ambus, P., Raivonen, M., Duyzer, J., Simpson, D., Fagerli, H., Fuzzi, S., Schjoerring, J. K., Granier, C., Neftel, A., Isaksen, I. S. A., Laj, P., Maione, M., Monks, P. S., Burkhardt, J., Daemmgen, U., Neirynck, J., Personne, E., Wichink-Kruit, R., Butterbach-Bahl, K., Flechard, C., Tuovinen, J. P., Coyle, M., Gerosa, G., Loubet, B., Altimir, N., Gruenhage, L., Ammann, C., Cieslik, S., Paoletti, E., Mikkelsen, T. N., Ro-Poulsen, H., Cellier, P., Cape, J. N., Horváth, L., Loreto, F., Niinemets, Ü., Palmer, P. I., Rinne, J., Misztal, P., Nemitz, E., Nilsson, D., Pryor, S., Gallagher, M. W., Vesala, T., Skiba, U., Brüggemann, N., Zechmeister-Boltenstern, S., Williams, J., O'Dowd, C., Facchini, M. C., de Leeuw, G., Flossman, A., Chaumerliac, N., and Erisman, J. W.: Atmospheric composition change: Ecosystems–Atmosphere interactions, Atmospheric Environment, 43, 5193-5267, 10.1016/j.atmosenv.2009.07.068, 2009.

Fung, P. K.: Ozone deposition over a boreal lake by the eddy covariance method (Masters dissertation), University of Helsinki, Helsinki, Finalnd, 2018.

Garratt, J. R.: Flux profile relations above tall vegetation, Quarterly Journal of the Royal Meteorological Society, 104, 199-211, https://doi.org/10.1002/qj.49710443915, 1978.

Garratt, J. R.: The atmospheric boundary layer, Cambridge University Press, Cambridge, 316 pp., 1992.

Geddes, J. A., and Murphy, J. G.: Observations of reactive nitrogen oxide fluxes by eddy covariance above two midlatitude North American mixed hardwood forests, Atmospheric Chemistry and Physics, 14, 2939-2957, 10.5194/acp-14-2939-2014, 2014.

Goldstein, A. H., Fan, S. M., Goulden, M. L., Munger, J. W., and Wofsy, S. C.: Emissions of ethene, propene, and *1*-butene by a midlatitude forest, Journal of Geophysical Research, 101, 9149-9157, 1996.

Hardacre, C., Wild, O., and Emberson, L.: An evaluation of ozone dry deposition in global scale chemistry climate models, Atmospheric Chemistry and Physics, 15, 6419-6436, 10.5194/acp-15-6419-2015, 2015.

Hogg, A., Uddling, J., Ellsworth, D., Carroll, M. A., Pressley, S., Lamb, B., and Vogel, C.: Stomatal and non-stomatal fluxes of ozone to a northern mixed hardwood forest, Tellus B: Chemical and Physical Meteorology, 59, 514-525, 10.1111/j.1600-0889.2007.00269.x, 2007.

Horvath, L., Koncz, P., Moring, A., Nagy, Z., Pinter, K., and Weidinger, T.: An Attempt to Partition Stomatal and Non-stomatal Ozone Deposition Parts on a Short Grassland, Boundary-Layer Meteorology, 167, 303-326, 10.1007/s10546-017-0310-x, 2018.

Ibrom, A., Dellwik, E., Flyvbjerg, H., Jensen, N. O., and Pilegaard, K.: Strong low-pass filtering effects on water vapour flux measurements with closed-path eddy correlation systems, Agricultural and Forest Meteorology, 147, 140-156, 10.1016/j.agrformet.2007.07.007, 2007.

Jerrett, M., Burnett, R. T., Pope III, C. A., Ito, K., Thurston, G., Krewski, D., Shi, Y., Calle, E., and Thun, M.: Long-Term Ozone Exposure and Mortality, The New England Journal of Medicine, 360, 1085-1095, 2009.

Kaimal, J. C., Wyngaard, J. C., Izumi, Y., and Cote, O. R.: Spectral characteristics of surface-layer turbulence, Quarterly Journal of the Royal Meteorological Society, 98, 563-589, 1972.

Keronen, P., Reissel, A., Rannik, U., Pohja, T., Siivola, E., Hiltunen, V., Hari, P., Kulmala, M., and Vesala, T.: Ozone flux measurements over a Scots pine forest using eddy covariance method: performance evaluation and comparison with flux-profile method, Boreal Environment Research 8, 425-433, 2003.

Kurpius, M. R., and Goldstein, A. H.: Gas-phase chemistry dominates O_3 loss to a forest, implying a source of aerosols and hydroxyl radicals to the atmosphere, Geophysical Research Letters, 30, 10.1029/2002gl016785, 2003.

Lamaud, E., Loubet, B., Irvine, M., Stella, P., Personne, E., and Cellier, P.: Partitioning of ozone deposition over a developed maize crop between stomatal and non-stomatal uptakes, using eddy-covariance flux measurements and modelling, Agricultural and Forest Meteorology, 149, 1385-1396, 10.1016/j.agrformet.2009.03.017, 2009.

Lee, J. E., Berry, J. A., van der Tol, C., Yang, X., Guanter, L., Damm, A., Baker, I., and Frankenberg, C.: Simulations of chlorophyll fluorescence incorporated into the Community Land Model version 4, Glob Chang Biol, 21, 3469-3477, 10.1111/gcb.12948, 2015.

Lenschow, D. H., and Raupach, M. R.: The attenuation of fluctuations in scalar concentrations through sampling tubes, Journal of Geophysical Research, 96, 15259-15268, 1991.

Lenschow, D. H., Wulfmeyer, V., and Senff, C.: Measuring Second- through Fourth-Order Moments in Noisy Data, Journal of Atmospheric and Oceanic Technology, 17, 1330-1347, 2000.

Leuning, R., and King, K. M.: Comparison of eddy-covariance measurements of CO_2 fluxes by open- and closed-path CO_2 analyzers, Boundary-Layer Meteorology, 59, 297-311, 1992.

Li, Q., Gabay, M., Rubin, Y., Fredj, E., and Tas, E.: Measurement-based investigation of ozone deposition to vegetation under the effects of coastal and photochemical air pollution in the Eastern Mediterranean, Sci. Total Environ., 645, 1579-1597, 10.1016/j.scitotenv.2018.07.037, 2018.

Loades, D. C., Yang, M., Bell, T. G., Vaughan, A. R., Pound, R. J., Metzger, S., Lee, J. D., and Carpenter, L. J.: Ozone deposition to a coastal sea: comparison of eddy covariance observations with reactive air–sea exchange models, Atmospheric Measurement Techniques, 13, 6915-6931, https://doi.org/10.5194/amt-13-6915-2020, 2020.

Martin, M. V., Heald, C. L., and Arnold, S. R.: Coupling dry deposition to vegetation phenology in the Community Earth SystemModel: Implications for the simulation of surface O3, Geophysical Research Letters, 41, 2988-2996, 10.1002/2014gl059651, 2014.

Massman, W. J.: Partitioning ozone fluxes to sparse grass and soil and the inferred resistances to dry deposition, Atmospheric Environment, 27A, 167-174, 1993.

Massman, W. J.: Estimating canopy conductance to ozone uptake from observations of evapotranspiration at the canopy scale and at the leaf scale, Global Change Biology, 1, 183-198, 1995.

Mauder, M., Cuntz, M., Drüe, C., Graf, A., Rebmann, C., Schmid, H. P., Schmidt, M., and Steinbrecher, R.: A strategy for quality and uncertainty assessment of long-term eddy-covariance measurements, Agricultural and Forest Meteorology, 169, 122-135, 10.1016/j.agrformet.2012.09.006, 2013.

McMillen, R. T.: An eddy correlation technique with extended applicability to non-simple terrain, Boundary-Layer Meteorology, 43, 231-245, 1988.

Meredith, L. K., Commane, R., Munger, J. W., Dunn, A., Tang, J., Wofsy, S. C., and Prinn, R. G.: Ecosystem fluxes of hydrogen: a comparison of flux-gradient methods, Atmospheric Measurement Techniques, 7, 2787-2805, 10.5194/amt-7-2787-2014, 2014.

Mikkelsen, T. N., Ro-Poulsen, H., Pilegaard, K., Hovmand, M. F., Jensen, N. O., Christensen, C. S., and Hummelshoej, P.: Ozone uptake by an evergreen forest canopy: temporal variation and possible mechanisms, Environmental Pollution, 109, 423-429, 2000.

Muller, J. B. A., Coyle, M., Fowler, D., Gallagher, M. W., Nemitz, E. G., and Percival, C. J.: Comparison of ozone fluxes over grassland by gradient and eddy covariance technique, Atmospheric Science Letters, 10, 164-169, 10.1002/asl.226, 2009.

Neirynck, J., Gielen, B., Janssens, I. A., and Ceulemans, R.: Insights into ozone deposition patterns from decade-long ozone flux measurements over a mixed temperate forest, J Environ Monit, 14, 1684-1695, 10.1039/c2em10937a, 2012.

Oke, T. R.: Boundary Layer Climates, 2nd ed., University Press, Cambridge, 1987.

Padro, J.: Summary of ozone dry deposition velocity measurements and model estimates over vineyard, cotton, grass and deciduous forest in summer, Atmospheric Environment, 30, 2363-2369, 1996.

Peltola, O., Hensen, A., Helfter, C., Belelli Marchesini, L., Bosveld, F. C., van den Bulk, W. C. M., Elbers, J. A., Haapanala, S., Holst, J., Laurila, T., Lindroth, A., Nemitz, E.,

Rockmann, T., Vermeulen, A. T., and Mammarella, I.: Evaluating the performance of commonly used gas analysers for methane eddy covariance flux measurements: the InGOS inter-comparison field experiment, Biogeosciences, 11, 3163-3186, 10.5194/bg-11-3163-2014, 2014.

Plake, D., Stella, P., Moravek, A., Mayer, J. C., Ammann, C., Held, A., and Trebs, I.: Comparison of ozone deposition measured with the dynamic chamber and the eddy covariance method, Agricultural and Forest Meteorology, 206, 97-112, 10.1016/j.agrformet.2015.02.014, 2015.

Rannik, U., Vesala, T., and Keskinen, R.: On the damping of temperature fluctuations in a circular tube relevant to the eddy covariance measurement technique, Journal of Geophysical Research-Atmospheres, 102, 12789-12794, 10.1029/97jd00362, 1997.

Rannik, U., N. Altimir, N., Mammarella, I., Bäck, J., Rinne, J., Ruuskanen, T. M., Hari, P., Vesala, T., and Kulmala, M.: Ozone deposition into a boreal forest over a decade of observations: evaluating deposition partitioning and driving variables, Atmospheric Chemistry and Physics, 12, 12165-12182, 10.5194/acp-12-12165-2012, 2012.

Raupach, M. R., Thom, A. S., and Edwards, I.: A wind-tunnel study of turbulent flow close to regularly arrayed rough surfaces, Boundary-Layer Meteorology, 18, 373-397, 1980.

Raupach, M. R., and Legg, B. J.: The uses and limitations of flux-gradient relationships in micrometeorology, Agricultural Water Management, 8, 119-131, 1984.

Reich, P. B.: Quantifying plant response to ozone: a unifying theory, Tree Physiol, 3, 63-91, 10.1093/treephys/3.1.63, 1987.

Sabbatini, S., Mammarella, I., Arriga, N., Fratini, G., Graf, A., Hörtnagl, L., Ibrom, A., Longdoz, B., Mauder, M., Merbold, L., Metzger, S., Montagnani, L., Pitacco, A., Rebmann, C., Sedlák, P., Šigut, L., Vitale, D., and Papale, D.: Eddy covariance raw data processing for CO_2 and energy fluxes calculation at ICOS ecosystem stations, International Agrophysics, 32, 495-515, 10.1515/intag-2017-0043, 2018.

Simpson, I. J., Thurtell, G. W., Neumann, H. H., Den Hartog, G., and Edwards, G. C.: The Validity of Similarity Theory in the Roughness Sublayer Above Forests, Boundary-Layer Meteorology, 87, 69-99, https://doi.org/10.1023/A:1000809902980, 1998.

Stella, P., Loubet, B., Laville, P., Lamaud, E., Cazaunau, M., Laufs, S., Bernard, F., Grosselin, B., Mascher, N., Kurtenbach, R., Mellouki, A., Kleffmann, J., and Cellier, P.: Comparison of methods for the determination of NO-O_3-NO_2 fluxes and chemical interactions over a bare soil, Atmospheric Measurement Techniques, 5, 1241-1257, 10.5194/amt-5-1241-2012, 2012.

Turnipseed, A. A., Huey, L. G., Nemitz, E., Stickel, R., Higgs, J., Tanner, D. J., Slusher, D. L., Sparks, J. P., Flocke, F., and Guenther, A.: Eddy covariance fluxes of peroxyacetyl nitrates (PANs) and NO_y to a coniferous forest, Journal of Geophysical Research Atmospheres, 111, D09304, 10.1029/2005JD006631, 2006.

Turnipseed, A. A., Burns, S. P., Moore, D. J. P., Hu, J., Guenther, A. B., and Monson, R. K.: Controls over ozone deposition to a high elevation subalpine forest, Agricultural and Forest Meteorology, 149, 1447-1459, 10.1016/j.agrformet.2009.04.001, 2009.

Vermeuel, M. P., Cleary, P. A., Desai, A. R., and Bertram, T. H.: Simultaneous Measurements of O_3 and HCOOH Vertical Fluxes Indicate Rapid In-Canopy Terpene Chemistry Enhances O_3 Removal Over Mixed Temperate Forests, Geophysical Research Letters, 48, 2020GL090996, 10.1029/2020GL090996, 2021.

Webb, E., Pearman, G., and Leuning, R.: Correction of flux measurements for density effects due to heat and water vapour transfer, Quarterly Journal of the Royal Meteorological Society, 106, 85-100, 1980.

Webb, E. K.: Profile relationships: The log-linear range, and extension to strong stability, Quarterly Journal of the Royal Meteorological Society, 96, 67-90, 10.1002/qj.49709640708, 1970.

Wesley, M. L., Eastman, J. A., Cook, D. R., and Hicks, B. B.: Daytime variations of ozone eddy fluxes to maize, Boundary-Layer Meteorology, 15, 361-373, 1978.

Wild, O.: Modelling the global tropospheric ozone budget: exploring the variability in current models, Atmospheric Chemistry and Physics, 7, 2643-2660, 2007.

Wohlfahrt, G., Hortnagl, L., Hammerle, A., Graus, M., and Hansel, A.: Measuring eddy covariance fluxes of ozone with a slow-response analyser, Atmos Environ (1994), 43, 10.1016/j.atmosenv.2009.06.031, 2009.

Wu, Z. Y., Zhang, L., Wang, X. M., and Munger, J. W.: A modified micrometeorological gradient method for estimating O_3 dry depositions over a forest canopy, Atmospheric Chemistry and Physics, 15, 7487-7496, 10.5194/acp-15-7487-2015, 2015.

Young, P. J., Archibald, A. T., Bowman, K. W., Lamarque, J. F., Naik, V., Stevenson, D. S., Tilmes, S., Voulgarakis, A., Wild, O., Bergmann, D., Cameron-Smith, P., Cionni, I., Collins, W. J., Dalsøren, S. B., Doherty, R. M., Eyring, V., Faluvegi, G., Horowitz, L. W., Josse, B., Lee, Y. H., MacKenzie, I. A., Nagashima, T., Plummer, D. A., Righi, M., Rumbold, S. T., Skeie, R. B., Shindell, D. T., Strode, S. A., Sudo, K., Szopa, S., and Zeng, G.: Pre-industrial to end 21st century projections of tropospheric ozone from the Atmospheric Chemistry and Climate Model Intercomparison Project (ACCMIP), Atmospheric Chemistry and Physics, 13, 2063-2090, 10.5194/acp-13-2063-2013, 2013.

Young, P. J., Naik, V., Fiore, A. M., Gaudel, A., Guo, J., Lin, M. Y., Neu, J. L., Parrish, D. D., Rieder, H. E., Schnell, J. L., Tilmes, S., Wild, O., Zhang, L., Ziemke, J., Brandt, J., Delcloo, A., Doherty, R. M., Geels, C., Hegglin, M. I., Hu, L., Im, U., Kumar, R., Luhar, A., Murray, L., Plummer, D., Rodriguez, J., Saiz-Lopez, A., Schultz, M. G., Woodhouse, M. T., and Zeng, G.: Tropospheric Ozone Assessment Report: Assessment of global-scale model performance for global and regional ozone distributions, variability, and trends, Elementa Science of the Anthropocene, 6, 10, 10.1525/journal.elementa.265, 2018.

Zahn, A., Weppner, J., Widmann, H., Schlote-Holubek, K., Burger, B., Kuhner, T., and Franke, H.: A fast and precise chemiluminescence ozone detector for eddy flux
and airborne application, Atmospheric Measurement Techniques, 5, 363-375, 10.5194/amt-5-363-2012, 2012.

Zhu, Z., Zhao, F., Voss, L., Xu, L., Sun, X., Yu, G., and Meixner, F. X.: The effects of different calibration and frequency response correction methods on eddy covariance ozone flux measured with a dry chemiluminescence analyzer, Agricultural and Forest Meteorology, 213, 114-125, 10.1016/j.agrformet.2015.06.016, 2015.

Zhu, Z. L., Tang, X. Z., and Zhao, F. H.: Comparison of Ozone Fluxes over a Maize Field Measured with Gradient Methods and the Eddy Covariance Technique, Advances in Atmospheric Sciences, 37, 586-596, 10.1007/s00376-020-9217-4, 2020.

Zona, D., Gioli, B., Fares, S., De Groote, T., Pilegaard, K., Ibrom, A., and Ceulemans, R.: Environmental controls on ozone fluxes in a poplar plantation in Western Europe, Environmental Pollution, 184, 201-210, 2014.

CHAPTER 4: ON THE TEMPERATURE DEPENDENCE OF OZONE DRY DEPOSITION IN A CENTRAL VIRGINIA FOREST

4.1 Introduction

Tropospheric O_3 is an air pollutant, greenhouse gas, and secondary organic aerosol precursor (Szopa, 2021) that impairs plant and ecosystem productivity and human health (Jerrett et al., 2009; Reich, 1987). Models and observations suggest O_3 sources and sinks will vary with rising temperatures, increasing O_3 air pollution (Nolte et al., 2018). O_3 is photochemically produced via reactions of nitrogen oxides ($NO_x \equiv NO + NO_2$) and volatile organic compounds (VOCs) and lost from the troposphere via chemical loss and dry deposition (Ainsworth et al., 2012; Fowler et al., 2009). Climate change-driven increases in temperature-dependent O_3 production (PO_3) are well known (Nolte et al., 2018; Pusede et al., 2015); however, how O_3 loss (LO_3) via dry deposition will scale with climate change is more uncertain, even though dry deposition may control a large portion of the O_3 mixing ratio variability (Andersson and Engardt, 2010; Fowler et al., 2009; Garland and Derwent, 1979; Kavassalis and Murphy, 2017). Presently, the small number of direct observations of LO_3-temperature relationships, over few land cover types, limit evaluations of how rising temperatures will alter LO_3.

Temperature's influence on LO_3 depends on whether deposition occurs via the plant stomata, leaf cuticle, ground surface, or whether O_3 is lost through within-canopy chemistry, therefore LO_3-temperature relationships presented in the literature are pathway-specific. Observations suggest stomatal LO_3 both decreases (Coyle et al., 2009; Fares et al., 2012; Fares et al., 2014; Turnipseed

et al., 2009; Wong et al., 2022) and increases (Fares et al., 2010; Liu et al., 2021) with temperature, varying seasonally and with land cover type. A primary LO_3 pathway in many ecosystems is plant stomatal uptake, which is a function of the stomatal conductance (g_s), defined as CO_2 diffusivity through the intercellular airspace (Ball et al., 1987). Literature estimates of stomatal deposition range from 10–90% of total LO_3 in the troposphere during the daytime (Clifton et al., 2020). O_3 stomatal uptake can reduce g_s, plant productivity, plant transpiration, and the land-carbon sink, which indirectly contributes to climate forcing (Arnold et al., 2018; Fares et al., 2013; Lombardozzi et al., 2013; Sadiq et al., 2017; Sitch et al., 2007). Greenhouse gas-driven environmental change will affect tropospheric LO_3, with increasing CO_2, air temperature, and drought frequency and severity, each depressing g_s (Ainsworth and Rogers, 2007; Zapletal et al., 2012). Leaves have an optimal temperature, below which g_s increases and above which it decreases (Jarvis, 1976); however, Urban et al. (2017) observed no such decrease at a constant vapor pressure deficit (VPD). Decreased turgor pressure in guard cells reduces stomatal aperture, and subsequently g_s, to maintain transpiration rates (Mott and Parkhurst, 1991), typically occurring under high VPD condition to minimize water loss (Grossiord et al., 2020; Jarvis, 1976). Entwined temperature, VPD, and g_s relationships (Buckley and Mott, 2013; Grossiord et al., 2020), make isolating their effects on O_3 deposition difficult (Tuovinen et al., 2009). Despite their importance in the O_3 loss budget (Clifton et al., 2020) and the potential to affect O_3 air quality (Emberson et al., 2013; Gong, 2021; Huang et al., 2016; Lin et al., 2019; Lin et al., 2020), observations of stomatal LO_3-temperature relationships are infrequently described in the literature.

Climate change effects on nonstomatal O_3 deposition are also uncertain. Nonstomatal LO_3 pathways include cuticular and soil uptake and loss to within-canopy chemistry, all of which vary with temperature and moisture (Altimir et al., 2006; Fowler et al., 2001; Hogg et al., 2007; Kurpius

and Goldstein, 2003; Lamaud et al., 2002; Wong et al., 2022; Zhang et al., 2002). Temperautre may enhance cuticular uptake via thermal decomposition on leaf cuticles (Cape et al., 2009; Coyle et al., 2009). In addition, within-canopy chemical loss occurs via reactions of O_3 with temperature-dependent biogenic VOCs (BVOCs) (Fares et al., 2010; Goldstein et al., 2004; Holzinger et al., 2005; Kurpius and Goldstein, 2003; Vermeuel et al., 2021; Wolfe et al., 2011). Few predictions regard how climate change will affect nonstomatal O_3 deposition; however, emissions of O_3-reactive monoterpenes may increase as temperatures and/or ambient O_3 increases (Feng et al., 2019). Recent work suggests that while increasingly warm temperatures and high VPD conditions may suppress O_3 deposition by limiting g_s (Ficklin and Novick, 2017; Grossiord et al., 2020; Way and Oren, 2010), increased nonstomatal deposition on high-temperature, high-VPD days can compensate for the reduction (Wong et al., 2022).

The Southeast U.S. contains 27% of all forested area in the U.S. (Carter, 2018) and climate change is warming the region (Hayhoe et al., 2018). In the Southeast, models predict future hotter, drier summers and warmer winters (Carter, 2018), which may lengthen both the O_3 season, when PO_3 is typically high, and the growing season, when LO_3 becomes a more important term in O_3 mass balance. Because the magnitude of LO_3 and the dominant uptake pathway vary seasonally (Clifton et al., 2020; Kurpius and Goldstein, 2003; Rannik et al., 2012), capturing the full spectrum of temperature conditions requires seasonally resolved measurements. High O_3 deposition to forests (Hardacre et al., 2015) makes the Southeast an important region in which to meausure LO_3. The literature contains few measurements of O_3 deposition in the Southeast and none to a non-plantation forest (Finkelstein et al., 2000; Meyers et al., 1998; Pleim et al., 1997; Wu et al., 2003; Zhang et al., 2002).

Here, I explore O_3 deposition velocity (v_d) and O_3-temperature relationships in a Central Virginia forest using two years of eddy covariance O_3 v_d, O_3 mixing ratio, temperature, VPD, solar-induced fluorescence (SIF), and BVOC measurements. I demonstrate that O_3 v_d is the largest control over O_3 mixing ratio locally. Using a resistance framework, I separate O_3 v_d into its stomatal and nonstomatal components and identify within-canopy BVOC reactions as the driving nonstomatal loss process. I describe each loss pathway's relative importance, seasonally and with time of day, and evaluate how each pathway varies with temperature. I use stomatal and nonstomatal O_3 v_d-temperature relationships to explain when and why O_3 varies with temperature and I discuss the implications for O_3 pollution as the region warms.

4.2 Methods

4.2.1 Instrumentation

4.2.1.1 Ozone

I observed O_3 mixing ratios, O_3 eddy-covariance flux (F_{O3}), and O_3 v_d in a mixed deciduous and coniferous forest at the Virginia Forest Laboratory (VFL), located in the Piedmont region of Central Virginia (37.9229°N, 78.2739°W) from July 2019–July 2021. I measured eddy covariance F_{O3} and O_3 v_d atop a 40-m scaffolding tower above a forest canopy 24 m in height. Inlets at 40 m, 30 m, 20 m, 9 m, and 1 m captured the O_3 mixing ratio. At the base of the tower, a climate-controlled laboratory housed all instrumentation.

A precise and fast (10^{-1} s) wet chemiluminescence O_3 instrument (LOZ-3F, Drummond Technology) and 3D sonic anemometer (WindMaster, Gill) measured F_{O3} and O_3 v_d. A dry scroll

pump (nXDS20i, Edwards) delivered air from the 40-m sampling inlet to a reaction chamber where ambient O_3 reacted with Eosin-Y dye. A valved flow meter (EW 32460-50, Cole-Parmer) controlled the flow rate, maintaining turbulent flow through the line. A photomultiplier tube measured photons emitted as a product of this reaction. An internal instrument zero corrected for baseline drift. A slower response (2–60 s) UV absorption-based analyzer co-sampled with the LOZ-3F for the first 20 minutes of each hour, providing an accurate standard for the flux precision. I calculated O_3 v_d according to Eqs. 1 and 2, where w is the vertical wind velocity and x is the scalar, O_3, for half-hourly averaging periods.

$$F_x = \frac{1}{n}\sum_{i=1}^{n}(w_i - \overline{w})(x_i - \overline{x}) = \overline{w'x'} \quad (1)$$

$$O_3\ v_d = -F_{O_3}/[O_3] \quad (2)$$

The slower response UV absorption-based analyzer (July–December 2019, T400, Teledyne API; December 2019–January 2020, 202, 2B Technologies; and January 2020–July 2021: 205, 2B Technologies) measured the vertical gradient of the O_3 mixing ratio at five heights within and above the canopy. Sampling cycled through each inlet once per hour using a manifold of solenoid valves. An O_3 generator (146i, ThermoFisher) and zero air generator (T701, Teledyne API) calibrated the UV absorption-based analyzers daily at 2 am local time (LT). A detailed description of the O_3 instrumentation, calibration, and data processing procedures can be found in Chapter 3.

4.2.1.2 Water flux

An open-path infrared absorption sensor (Li7500, LICOR) measured fast water vapor (10 s^{-1}) and a 3D sonic anemometer (CSAT3, Campbell Scientific) measured vertical winds (10 s^{-1}) at 32 m.

Data pre-processing included discarding 30-minute measurement periods if sampling occurred for less than 75% of the 30-minute period or if nighttime incoming shortwave radiation was <10 W m^{-2}, despiking the mixing ratio and vertical winds, and rotating wind axes. The EddyPro software (LICOR, Lincoln, NE) calculated the H_2O flux according to Eq. 1 and applied corrections to the flux, including a Webb-Pearman-Leuning correction (Tatham, 2021).

4.2.1.3 Air temperature and relative humidity

Temperature and humidity probes (HMP45, Vaisala) measured air temperature and relative humidity at 32 m.

4.2.1.4 Solar-induced fluorescence (SIF)

SIF is a measure of the fluorescence of excited-state chlorophyll molecules. Shown to be proportional to the electron transport rate to the photosystem during daylight hours (Porcar-Castell et al., 2014), SIF correlates with photosynthesis at the canopy scale (Yang et al., 2015). A high temporal resolution FluoSpec 2 system (Yang et al., 2018) measured SIF at 40 m on the research tower. The FluoSpec 2 has a spectral resolution of ~0.13 nm over 680–775 nm (QEpro, OceanOptics, Inc.), providing a high signal-to-noise ratio. An inline fiber optic shutter (FOS-2 *x* 2-TTL, OceanOptics, Inc.) directs spectrometer viewing from either of two fiber optics, one pointed toward the canopy and a second fitted with a cosine corrector and angled skyward to collect incident light at 180° from the field of view. Viewing alternated between the canopy and reference (sky) every 5 s to produce a complete measurement once per 5 min. Spectral fitting methods are used to extract SIF by using the 760 nm oxygen absorption (O_2-A) band or the Fraunhofer lines

between 730 nm and 760 nm. The SIF field of view is limited to two trees, a Southern Red Oak and a White Oak.

4.2.1.5 Biogenic volatile organic compounds (BVOCs)

A gas chromatograph-flame ionization detector (GC-FID) measured speciated BVOC mixing ratios from an inlet located 20 m above the ground at the level of the mid-canopy. In brief, the GC-FID sampled with an insulated and waterproof tube held at 45 ºC. A sodium-thiosulfate-infused quartz fiber filter scrubbed the air of O_3 and a multibed adsorbent trap concentrated a subsample. Thermal desorption under a helium backflash transferred analytes to the head of a GC column in a GC oven. Analytes were separated in the column and detected with an FID. Hydrogen gas served as FID fuel. A custom LabVIEW program automated sample collection, running for 54.5 minutes of each hour. A complete description of the instrument, setup, and operation can be found in McGlynn et al. (2021).

4.2.2 Stomatal and nonstomatal O_3 v_d

I determined drivers of the O_3 v_d-temperature relationship using a resistance framework to separate O_3 v_d into stomatal and nonstomatal components. Here, v_d is the inverse of the total resistance, which is the sum of the aerodynamic (r_a), quasi-laminar (r_b) for O_3, and canopy (r_c) resistances:

$$v_d = [r_a + r_b + r_c]^{-1} \quad (3)$$

Turbulent exchange drives r_a in the surface boundary layer, varying with atmospheric stability (Hicks et al., 1987), where r_a depends on k, the von Kármán constant, u_*, the friction velocity, z,

the measurement height, d, the zero plane displacement height, z_m, the roughness length, ψ_H, the stability correction function, and L, the Obukhov length (Clifton et al., 2017):

$$r_a = \frac{1}{k u_*}\left[\ln\left(\frac{z-d}{z_m}\right) - \psi_H\left(\frac{z-d}{L}\right)\right] \tag{4}$$

where Clifton et al. (2017) defines ψ_H as:

$$\psi_H = 2\ln\left(\frac{1+\left(0.95\left(1-11.6\frac{z-d}{L}\right)^{0.5}\right)}{2}\right), \qquad -2 < \frac{z-d}{L} < 0$$
$$\psi_H = -7.8\frac{z-d}{L}, \qquad 0 < \frac{z-d}{L} < 1 \tag{5}$$

to account for neutral, stable, or unstable conditions. Molecular diffusion in the boundary layer around individual surfaces drives r_b (Hicks et al., 1987), calculated following Wesely and Hicks (1977):

$$r_b = \frac{2}{\kappa u_*}\left(\frac{\kappa}{D}\right)^{2/3} \tag{6}$$

where κ is the thermal diffusivity of air (κ = 0.2 cm^2 s^{-1}), and D is the diffusivity of the gas (D_{O3} = 0.13 cm^2 s^{-1}). Eq. 7 separates r_c into stomatal (r_s) and nonstomatal (r_{ns}) resistances.

$$r_c = \left[\frac{1}{r_s} + \frac{1}{r_{ns}}\right]^{-1} \tag{7}$$

The sum of resistance to the stomata (r_{sto}) and mesophyll (r_m) equal r_s:

$$r_s = r_{sto} + r_m \tag{8}$$

where, r_m is a function of H*, Henry's law constant and a f_0, reactivity factor for O_3 (Vermeuel et al., 2021; Wesely, 1989; Wolfe and Thornton, 2011):

$$r_m = \left(\frac{H^*}{3000\ \text{M atm}^{-1}} + 100 f_0\right)^{-1} \tag{9}$$

I calculated r_{sto} according to the frequently used evaporation-resistance approach (e.g., Fares et al., 2010; Fares et al., 2012; Fares et al., 2013; Gerosa et al., 2005; Kurpius and Goldstein, 2003; Monteith and Unsworth, 1990; Turnipseed et al., 2009):

$$r_{sto} = \frac{\rho c_p (e_s - e)}{\gamma LE} - r_a - r_{b,\,w} \tag{10}$$

Here, ρ is the air density, c_p is the air heat capacity, e_s is the water vapor pressure at the leaf surface, e is the water vapor pressure at the measurement height, γ is the psychometric constant (γ = 67 Pa K^{-1}), LE is the latent heat flux, r_a is as described above, and $r_{b,\,w}$ is the quasi-laminar resistance calculated for water vapor according to Eq. 6 (D_{H2O} = 0.21 $cm^2\ s^{-1}$). It is commonly assumed that the sub-stomatal cavity is at saturation vapor pressure (Gerosa et al., 2005), which I do here, thus the vapor pressure is equal to the saturation vapor pressure and e_s is calculated according to Tetens' equation:

$$e_s = 611 \exp\left(\frac{17.269 T_l}{T_l + 237.3}\right) \tag{11}$$

where T_l is the leaf temperature, estimated as:

$$T_l = \frac{H}{\rho c_p}\left(r_a + r_{b,\,w}\right) + T \tag{12}$$

a function of H, the sensible heat flux, T, the air temperature, ρ, c_p, r_a, and $r_{b,\,w}$. The ratio of the diffusivity of H_2O to O_3 ($D_{H2O}/D_{O3} = 1.6$) scaled stomatal conductance ($g_s = r_s^{-1}$) for O_3 (Wesely, 1989):

$$g_{O3} = g_s \frac{D_{O3}}{D_{H2O}} \tag{13}$$

I calculated the nonstomatal conductance, ($g_{ns} = r_{ns}^{-1}$) two ways. First, using Eqs. 3 and 7 and second, as the difference between O_3 v_d and g_{O3}. Following Zhang et al. (2003) and Vermeuel et al. (2021), to estimate nonstomatal deposition to leaf cuticles and ground surfaces, I parameterized cuticular and ground resistances using Eqs. 14 and 15. Resistance to cuticular deposition (r_{cut}), which I treated as dry (Vermeuel et al., 2021), depends on relative humidity and leaf area index:

$$r_{cut} = \frac{r_{cutd0}}{e^{0.03RH}LAI^{0.25}u_*} \tag{14}$$

where r_{cutd0} is a reference value (Zhang et al., 2003), RH is relative humidity, and LAI is the leaf area index. I obtained LAI from the yearly four-day composite (MCD15A3H) Version 6 Moderate Resolution Imaging Spectroradiometer (MODIS) Level 4 using a combination of Aqua and Terra products (Myneni et al., 2021), downloaded from search.earthdata.nasa.gov. I linearly interpolated four-day LAI onto the half-hourly O_3 v_d time interval. The summation of the in-canopy aerodynamic resistance (r_{ac}) and soil resistance (r_{soil}) is equal to the total ground resistance. LAI, u_*, and a reference value determine r_{ac} (Zhang et al., 2003):

$$r_{ac} = \frac{r_{ac0}\mathrm{LAI}^{0.25}}{u_*^2} \quad (15)$$

where r_{ac0} depends on land cover type. Soil moisture determines r_{soil}. Following Vermeuel et al. (2021), r_{soil} is 300 s m^{-1} if the soil is wet and 200 s m^{-1} if the soil is dry. I defined wet soil as RH >60% following Fares et al. (2012). While these approximations improve upon big-leaf models where specific nonstomatal resistances are not resolved, they contain numerous limitations, including variations in surface wetness and aqueous chemistry, geographical location (references values are for broad land cover types), and not capturing environmental transitions (e.g., wet to dry conditions) or canopy structure, which varies between forest canopies and seasonally (Zhang et al., 2002, 2003). I discuss uncertainties in these estimates in the Results.

4.3 Results and Discussion

At the VFL, the highest O_3 v_d occur May–September, corresponding with the growing season (Figure 4.1). Daytime O_3 v_d, defined as 10 am–3 pm LT means, are consistently higher than nighttime O_3 v_d, defined as 11 pm–5 am LT means. Monthly mean daytime O_3 v_d June–August ranges from 0.75 ± 0.24 cm s^{-1} to 0.86 ± 0.23 cm s^{-1}, corresponding with nighttime O_3 v_d ranging from 0.36 ± 0.28 cm s^{-1} to 0.40 ± 0.26 cm s^{-1}, where the variability is one standard deviation. In the spring, daytime O_3 v_d rise sharply from April to June, while in the fall, the seasonal decline occurs more slowly, stretching from August through November. During the shoulder months, May and September, daytime O_3 v_d are similar, 0.57 ± 0.34 cm s^{-1} and 0.61 ± 0.22 cm s^{-1}, respectively, while nighttime O_3 v_d is 60% greater in September (0.32 ± 0.13 cm s^{-1}) than in May (0.20 ± 0.12 cm s^{-1}). Both daytime and nighttime O_3 v_d are minimal in the winter months.

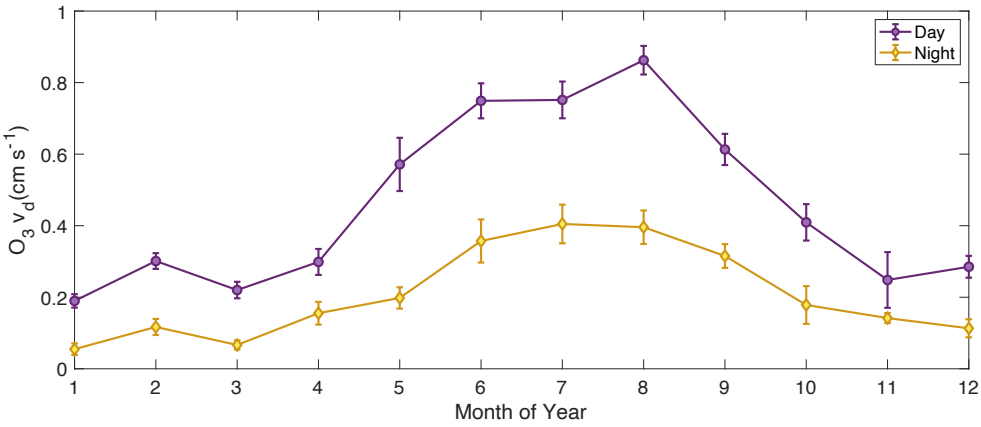

Figure 4.1. Daytime (purple circles) and nighttime (yellow diamonds) monthly average O_3 v_d (cm s^{-1}). Daytime is defined as 10 am–3 pm LT and nighttime is defined as 11 pm–5 am LT. Error bars represent standard error of the mean.

I separate O_3 v_d into its stomatal and nonstomatal components to demonstrate, seasonally and by time of day, when stomatal and nonstomatal deposition are important at the VFL. Stomatal deposition is nearly all of daytime O_3 v_d year-round and nonstomatal deposition is an important nighttime loss process spring through fall (Figure 4.2; Table 4.1). O_3 v_d in the winter (December–February) are low; however, daytime g_{O3} equal to the magnitude of O_3 v_d, suggests stomatal uptake occurs in the winter, presumably via evergreen species. In the spring (March–May), as daylight hours increase and the trees begin to leaf out, O_3 v_d increase and I observe concurrent increases in g_{O3}. In the summer (June–August), the stomatal fraction of deposition remains the dominant daytime pathway, but overnight O_3 v_d significantly (p-value < 0.05) exceeds g_{O3} (82% of nighttime deposition is nonstomatal). Fall (September–November) trends mimic those of summer, with g_{O3} equal in magnitude to O_3 v_d during the day and O_3 v_d significantly (p-value < 0.05) exceeding g_{O3} overnight and in the early morning (59% of nighttime deposition is nonstomatal). Separate measurement systems allow for times when measured g_{O3} exceeds O_3 v_d, however these differences were not statistically significant (p-value > 0.05). I assume at times of measurement mismatch that

all O_3 deposition is stomatal. A longer growing season, driven by warming temperatures (Carter, 2018; Hayhoe et al., 2018), will alter the seasonality of O_3 v_d with opportunity for more g_{O3} in the early spring and late fall.

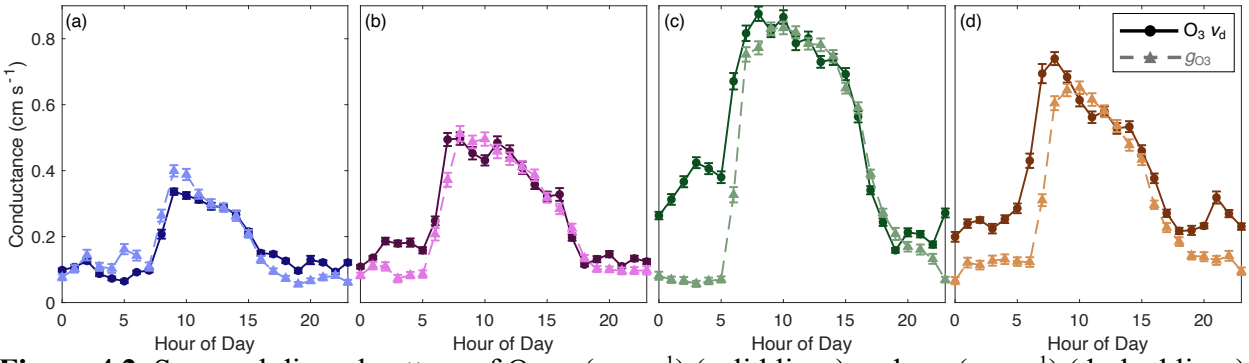

Figure 4.2. Seasonal diurnal pattern of O_3 v_d (cm s^{-1}) (solid lines) and g_{O3} (cm s^{-1}) (dashed lines) in the winter (a), spring (b), summer (c), and fall (d).

Table 4.1. Seasonal mean O_3 v_d (cm s^{-1}) and g_{O3} (cm s^{-1}) daytime (10 am–3 pm) and nighttime (11 pm–5 am). Variability as 1 standard deviation is represented parenthetically.

	O_3 v_d (cm s^{-1})		**g_{O3} (cm s^{-1})**	
	Day	**Night**	**Day**	**Night**
Winter	0.27 (0.12)	0.10 (0.08)	0.31 (0.21)	0.11 (0.16)
Spring	0.37 (0.28)	0.15 (0.12)	0.45 (0.33)	0.09 (0.15)
Summer	0.79 (0.27)	0.39 (0.25)	0.80 (0.31)	0.07 (0.12)
Fall	0.53 (0.23)	0.26 (0.14)	0.56 (0.28)	0.11 (0.16)

4.3.1 Impact of LO_3 on O_3 variability

Nonexistent or weak O_3 mixing ratio relationships with temperature and strong relationships with VPD (Figure 4.3) demonstrate plant-O_3 uptake controls daytime O_3 variability at the VFL. Due to low O_3 v_d, I do not present winter correlations. Kavassalis and Murphy (2017) demonstrated in vegetated environments where O_3 dry deposition drives O_3 variability, VPD better predicts O_3 than temperature, as reduced stomatal aperture under high VPD conditions allows VPD to act as a proxy for g_{O3} (Grossiord et al., 2020; Kavassalis and Murphy, 2017; Monks et al., 2015). Similarly, at the VFL, O_3 mixing ratios and temperature do not correlate in the spring or summer and positively

correlate in the fall, though weakly ($r_{O3\text{-}T}$ = 0.33); however, O_3 mixing ratios correlate with VPD, moderately to strongly, spring through fall. The summer O_3-VPD correlation is the weakest (though still moderately strong, $r_{O3\text{-}VPD}$ = 0.45), likely due to higher PO_3 in the summer daytime also influencing the O_3 mixing ratio. At the VFL, the lack of, or weak, O_3-temperature correlations and strong O_3-VPD correlations are consistent with LO_3, not PO_3, controlling O_3 variability.

4.3.2 Daytime O_3 v_d- and g_{O3}-temperature and SIF relationships

I observe seasonal variations in O_3 v_d- and g_{O3}-temperature relationships (Figure 4.3). O_3 v_d positively vary with temperature in the spring and fall and the correlations are moderately strong ($r_{vd\text{-}T}$ = 0.40 and $r_{vd\text{-}T}$ = 0.56, respectively). O_3 v_d in May, when daytime average temperatures have risen for the growing season, drive the positive spring correlation. Similarly, O_3 v_d in September, when growing season temperatures remain warm, drive the fall correlation. However, in the summer, O_3 v_d and temperature are uncorrelated, due to a decrease in O_3 v_d on the hottest days. Similarly, warm days in May drive the positive g_{O3}-temperature correlations in the spring, however the correlation is relatively weak ($r_{gO3\text{-}T}$ = 0.23) as the forest does not fully leaf out until mid- to late-spring. In the summer, the inverse correlation between g_{O3} and temperature is moderately strong ($r_{gO3\text{-}T}$ = –0.51). While the fall shows no significant correlation, the hottest days (occurring in September) mimic the summer trend, while the cooler days mimic the spring trend.

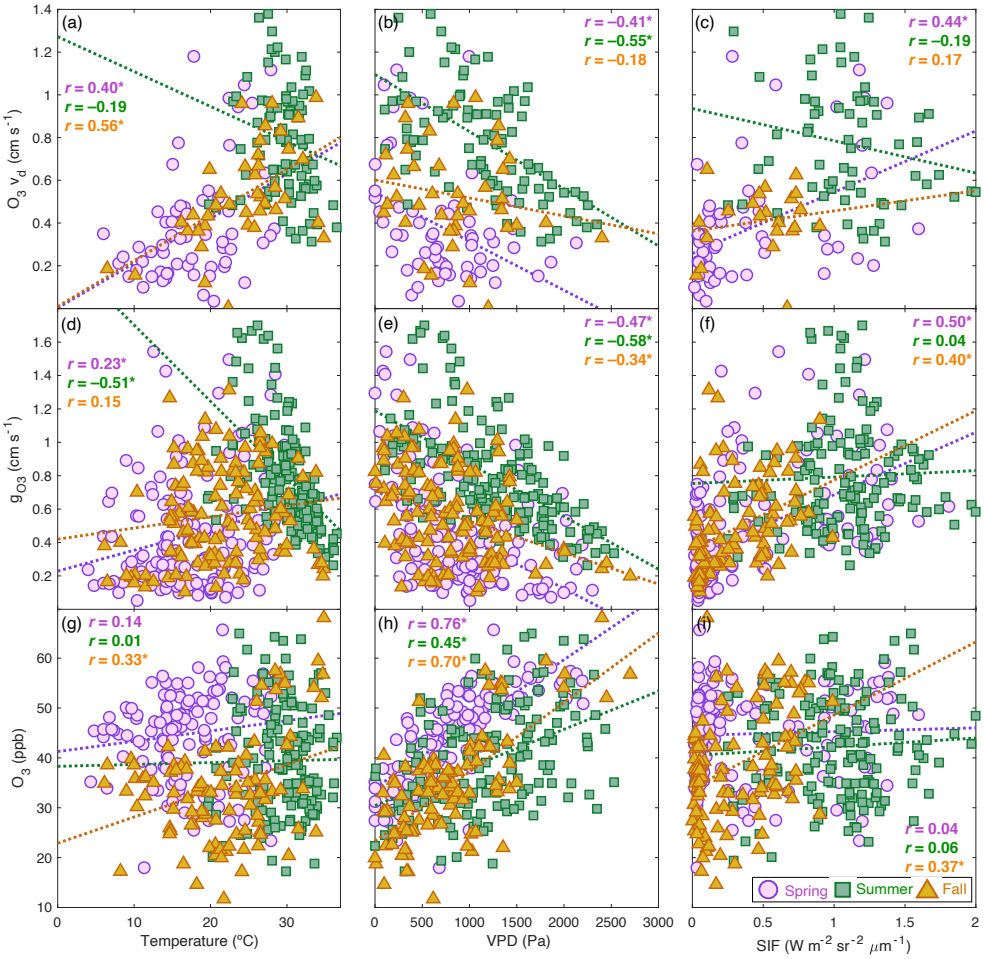

Figure 4.3. Correlations between daytime average (10 am–3 pm LT) O_3 v_d (cm s^{-1}) (a–c), g_{O3} (cm s^{-1}) (d–f), and O_3 mixing ratio (ppb) (g–i) with temperature (ºC) (a, d, g), vapor pressure deficit (Pa) (b, e, h), and SIF (W m^{-2} sr^{-2} μm^{-1}) (c, f, i) in the spring (purple circles), summer (green squares), and fall (orange triangles). Dashed lines are lines of best fit. Seasonal Pearson correlation coefficients (*r*) are indicated on each panel. Significant correlations (p-value < 0.05) are indicated with an *.

I use temperature trends across the growing season, capturing all high temperature days, to demonstrate how the O_3 v_d-temperature relationship impacts the O_3 mixing ratio (Figure 4.4). Both O_3 v_d and O_3 mixing ratio increase with temperature until 24ºC, are relatively stable from 24–32ºC, and above 32ºC, O_3 v_d decreases while O_3 mixing ratios increase. Above 32ºC, average O_3 v_d decreases 49% while average O_3 increases by 19%, or by 7.4 ppb, from their respective 24–32ºC means. Because g_{O3} decreases with temperature in the summer, and all daytime O_3 v_d is stomatal,

I infer that a reduction in stomatal aperture on hot days drives the O_3 v_d decrease. While PO_3 likely also increases on these days due to its well-established temperature dependence, the importance of LO_3 controlling O_3 variability suggests that diminished stomatal O_3 uptake increases O_3 mixing ratios.

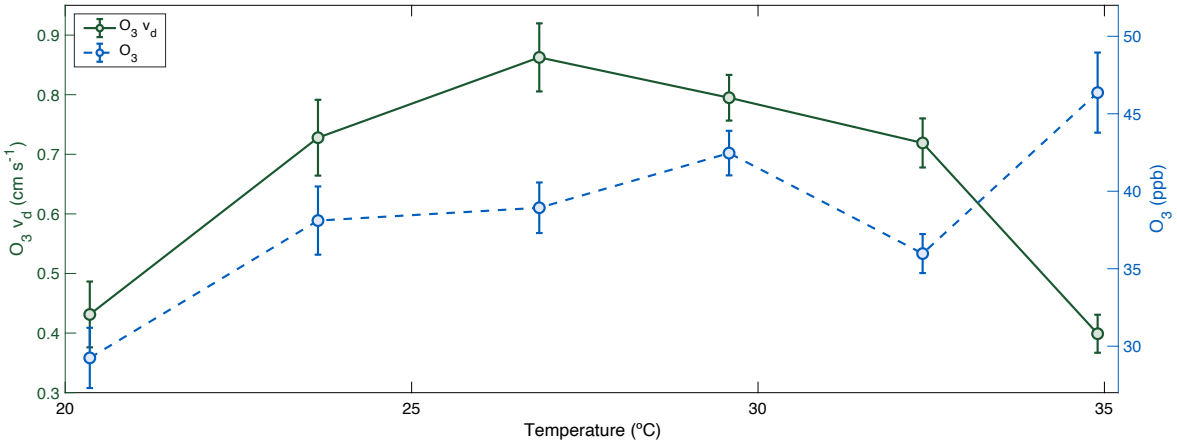

Figure 4.4. May–September daytime (10 am–3 pm LT) O_3 v_d (cm s^{-1}) (green, solid line) and O_3 mixing ratio (ppb) (blue, dashed line) binned by temperature (ºC). Error bars represent standard error of the mean.

Physical plant damage caused by O_3 stomatal uptake limits carbon uptake, impacting plant health, and can have cascading effects on biogeochemical cycling (Fares et al., 2013; Sadiq et al., 2017; Wittig et al., 2007; Wittig et al., 2009). At the VFL, I observe no canopy-scale correlation between SIF and O_3 v_d, g_{O3}, or O_3 mixing ratio in the summer (Figure 4.3). O_3 v_d positively varies with SIF in the spring ($r_{vd\text{-}SIF}$ = 0.44), and g_{O3} positively varies with SIF in both the spring and fall ($r_{gO3\text{-}SIF}$ = 0.50 and $r_{gO3\text{-}SIF}$ = 0.40, respectively). As with temperature, O_3 mixing ratio and SIF only significantly correlate in the fall ($r_{O3\text{-}SIF}$ = 0.37). At the leaf-level, stomata can close and SIF and photosynthesis may no longer be correlated (Marrs et al., 2020), potentially explaining the lack of relationships between O_3 v_d and g_{O3} with SIF in the summer, as the stomata are closing in the hottest and driest conditions, however this result was not upscaled to the canopy, thus its

application here is limited. Using SIF as a proxy for gross primary productivity, I find no evidence of reduced carbon assimilation on high O_3 days at the VFL, however, high O_3 at the VFL is relatively low compared to other study sites (e.g., Fares et al., 2013). The differing footprints of the O_3 v_d, g_{O3}, and SIF measurements limit these observations. The canopy-scale SIF only measures select trees within the canopy, thereby measurements exclude large parts of the forest captured in O_3 v_d and g_{O3}.

4.3.3 Nighttime O_3 v_d-, nonstomatal conductance (g_{ns}), and O_3-temperature relationships

Nonstomatal deposition, while a minor component of O_3 v_d during the day, is important overnight spring through fall (Figure 4.2; Table 4.1). In the spring and fall, 15% of total daily O_3 v_d occurs from 11 pm–5 am LT, and this increases to 18% in the summer months. Nonstomatal deposition patterns from spring through fall are consistent; thus, I discuss nonstomatal conductance (g_{ns}) across the entire growing season rather than by individual season. In order to maximize the number daily g_{ns} observations, because different instrument systems measured g_{O3} and O_3 v_d and calculations following Eq. 7 require simultaneous half-hourly measurements, I calculate nighttime mean g_{ns} as the difference between nighttime means of O_3 v_d and g_{O3}. Trends using both g_{ns} methods are the same. By subtracting the stomatal fraction, 12% of all growing season O_3 deposition at the VFL occurs at night via nonstomatal pathways.

Calculated cuticle (g_{cut}) and ground (g_{ground}) conductance, via the Zhang et al. (2003) parameterization, account for up to 75% of the nighttime nonstomatal fraction of O_3 v_d, however, nighttime average g_{ns} exhibits a temperature dependence not observed for g_{cut} nor g_{ground}. Estimates of g_{cut} and g_{ground} require broad land use category reference values, assumptions regarding surface wetness, soil moisture, and use coarse-resolution satellite LAI, all of which affect their precision,

accuracy, and variance with temperature. While I use these estimates to broadly observe g_{cut} and g_{ground} follow similar diurnal patterns to that of O_3 v_d, here, these estimates summed with g_{O3} are, on average, 56% higher than measured O_3 v_d, thus I assume they are overestimates. Other g_{ns} pathways include reactions with nitric oxide (NO) emitted from soils, however, previous work suggests that O_3 loss to soil NO is minimal (Clifton et al., 2020; Wong et al., 2022). Soil NO emissions are temperature dependent, but more significantly regulated by soil moisture (Homyak and Sickman, 2014; Pilegaard, 2013).

I observe similar diurnal patterns for g_{ns} and O_3-α-pinene reactivity and exponential relationships with temperature, suggesting that nighttime deposition occurs via in-canopy reactions with BVOCs (Figures 4.5–4.6). At the VFL, significant light-independent emissions of BVOCs occur at night, with the majority of O_3-BVOC reactions occurring with α-pinene, followed by limonene (McGlynn et al., 2023). Similarly, Kurpius and Goldstein (2003) used exponential relationships between g_{ns} and monoterpene flux with temperature to demonstrate the role of chemical loss in a forest canopy and reactive monoterpenes and sesquiterpenes emitted from the soil and understory have been previously reported to contribute to LO_3 not only above, but within forest canopies (Barreira et al., 2017; Bourtsoukidis et al., 2018; Gray et al., 2014). This temperature-dependent nighttime deposition decreases O_3 mixing ratios, as I observe nighttime O_3 inversely correlates with temperature ($r_{O3\text{-}T}$ = –0.29). In the Southeast, the number of nights with temperatures exceeding 24ºC is expected to increase (Carter, 2018), thus I compare O_3 mixing ratios on nights with mean temperatures below and above this value. On nights where the mean temperature <24ºC, mean O_3 is 26.7 ± 10.8 ppb, while on nights where the mean temperature ≥24ºC, O_3 is significantly lower (p-value < 0.05), with a mean of 19.9 ± 8.2 ppb, where the variability is one standard

deviation. Temperature trends suggest warming will further promote g_{ns} as BVOC emissions increases, resulting in lower nighttime O_3.

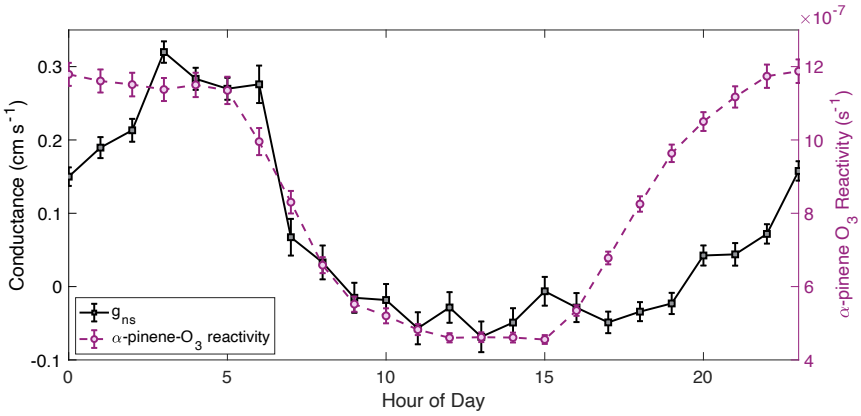

Figure 4.5. May–September diurnal patterns of g_{ns} (cm s^{-1}) (black squares, solid line) and the O_3 reactivity to α-pinene (s^{-1}) (pink circles, dashed line). Error bars represent standard error of the mean.

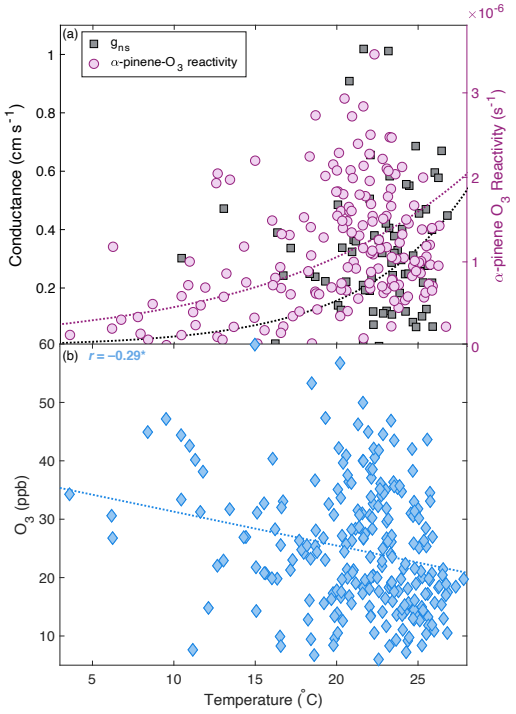

Figure 4.6. May–September nighttime average (11 pm–5 am LT) temperature (ºC) dependence of estimated g_{ns} (cm s^{-1}) (black squares) and α-pinene O_3 reactivity (s^{-1}) (pink circles) (a) and O_3 (ppb) (b).

4.3.4 LO_3 and rising temperatures

Temperatures in the Southeast U.S. will continue rising, leading to warmer winters, hotter summers, and more frequent heatwaves (Carter, 2018; Hayhoe et al., 2018), worsening O_3 pollution and threatening human and environmental health (Nolte et al., 2018). The O_3 climate penalty ($m_{O3\text{-}T}$), a measure of the increase in O_3 mixing ratio per degree, has declined due to precursor emissions reductions (e.g., Bloomer et al., 2009), however, rising temperatures require continued emissions reductions in order to sustain current pollution levels. In vegetated regions where stomatal uptake is the dominant loss pathway, such as the VFL, LO_3 is large enough to control O_3 variability rather than PO_3. An increase in the number of high temperature days will lower daytime O_3 v_d, increasing O_3 mixing ratio and $m_{O3\text{-}T}$.

Here, I frame $m_{O3\text{-}T}$ as increases O_3 due to temperature-driven reductions in stomatal O_3 deposition. I find that on the hottest growing season days, an increase in nighttime g_{ns} offsets the impact of decreased daytime g_{O3} on the O_3 mixing ratio, similar to observations reported by Wong et al. (2022). While growing season $m_{O3\text{-}T}$ is small (0.26 ± 0.14 ppb $^oC^{-1}$), days with mean daytime temperature above 32ºC, a threshold temperature over which O_3 v_d decreases and the O_3 mixing ratio increases, $m_{O3\text{-}T}$ = 2.12 ± 1.14 ppb $^oC^{-1}$, where the uncertainty is mean slope error. In Figure 4.7, I compare all growing season days with daytime mean temperature ≥32ºC, grouped by high (≥24ºC) and low (<24ºC) nighttime mean temperature. No daytime mean temperatures in May equaled or exceeded 32ºC. Across all hot days, following low temperature nights, daytime mean O_3 is 46.8 ± 10.3 ppb, while the high temperature nights significantly lower (p-value < 0.05) daytime mean O_3 to 36.4 ± 8.9 ppb, where the variability is one standard deviation. If climate change increases BVOC emissions (Kulmala et al., 2004; Penuelas and Staudt, 2010), an

increasing number of reactions between O_3 and monoterpenes may help offset reductions in g_{O3}; though, reactions between O_3 and monoterpenes produce secondary organic aerosols (Cao et al., 2022; Griffin et al., 1999; Kristensen et al., 2014), another harmful pollutant and climate forcer. However, only 23% of nights preceding the hottest days had mean temperatures ≥24ºC. In this forest, where stomatal LO_3 is the dominant growing season control over O_3 variability, I expect, as temperatures (and VPD) rise $m_{O3\text{-}T}$ will increase as a result of decreasing g_{O3}.

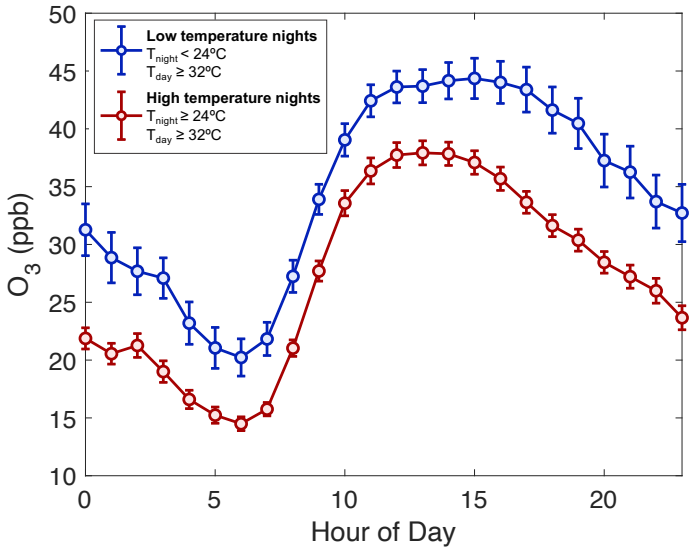

Figure 4.7. June–September O_3 (ppb) diurnal pattern on high temperature days (10 am–3 pm LT mean temperature ≥32ºC). Low temperature nights (11 pm–5 am LT mean temperature <24ºC) are shown in blue and high temperature nights (11 pm–5 am LT mean temperature ≥24ºC) are shown in red. Error bars represent standard error of the mean.

4.4 Conclusions

At the VFL, where LO_3 dominates the O_3 mass balance, high temperatures reduce O_3 v_d and increase O_3 mixing ratios. Using two years of O_3 v_d measurements, I observe the highest deposition in the summer. The lack of and weak O_3-temperature relationships, yet strong correlations with VPD, a proxy for g_{O3}, demonstrate that plant-O_3 uptake controls variability in daily O_3. SIF, a

proxy for photosynthesis, poorly predicts daytime O_3 v_d, g_{O3}, and O_3 mixing ratio at this site. Stomatal deposition controls all daytime deposition, increasing with temperature up to 32ºC, after which high temperatures and VPD facilitate stomatal closure, decreasing g_{O3} and consequently O_3 v_d. On hot days (10 am–3 pm LT mean temperature ≥32ºC), I observe a 49% decrease in O_3 v_d corresponds with a 19% increase in O_3 mixing ratio. Nonstomatal deposition, while a small fraction of overall O_3 v_d is important overnight. Throughout the growing season, this nighttime g_{ns} accounts for 12% of the 24-h cumulative O_3 v_d. I observe exponential relationships between nighttime g_{ns} and O_3 reactivity to α-pinene with temperature, indicating loss to in-canopy reactions with α-pinene and other monoterpenes is the dominant g_{ns} pathway. The temperature-driven increase in LO_3 decreases nighttime O_3 mixing ratios. High g_{ns} on warm nights counteracts reduced g_{O3} on hot days, lowering the daytime mean O_3 mixing ratio by 22%. I speculate, increasing temperatures and VPD, both predicted in the Southeast U.S., will reduce daytime LO_3 at the VFL, thus increasing $m_{O3\text{-}T}$ and ambient O_3.

References

Ainsworth, E. A., and Rogers, A.: The response of photosynthesis and stomatal conductance to rising CO_2: mechanisms and environmental interactions, Plant Cell and Environment, 30, 258-270, 10.1111/j.1365-3040.2007.01641.x, 2007.

Ainsworth, E. A., Yendrek, C. R., Sitch, S., Collins, W. J., and Emberson, L. D.: The effects of tropospheric ozone on net primary productivity and implications for climate change, Annu Rev Plant Biol, 63, 637-661, 10.1146/annurev-arplant-042110-103829, 2012.

Altimir, N., Kolari, P., Touovinen, J.-P., Vesala, T., Bäck, J., Suni, T., Kulmala, M., and Hari, P.: Foliage surface ozone deposition: a role for surface moisture?, Biogeosciences, 3, 209-228, 2006.

Andersson, C., and Engardt, M.: European ozone in a future climate: Importance of changes in dry deposition and isoprene emissions, Journal of Geophysical Research-Atmospheres, 115, 10.1029/2008jd011690, 2010.

Arnold, S. R., Lombardozzi, D., Lamarque, J. F., Richardson, T., Emmons, L. K., Tilmes, S., Sitch, S. A., Folberth, G., Hollaway, M. J., and Martin, M. V.: Simulated Global Climate Response to Tropospheric Ozone-Induced Changes in Plant Transpiration, Geophysical Research Letters, 45, 13070-13079, 10.1029/2018gl079938, 2018.

Ball, J. T., Woodrow, I. E., and Berry, J. A.: A Model Predicting Stomatal Conductance and Its Contribution to the Control of Photosynthesis Under Different Environmental Conditions, in: Progress in Photosynthesis Research, edited by: Biggins, J., Nijhoff, Dordrecht, The Netherlands, 221-224, 1987.

Barreira, L. M. F., Duporte, G., Parshintsev, J., Hartonen, K., Jussila, M., Aalto, J., Back, J., Kulmala, M., and Riekkola, M. L.: Emissions of biogenic volatile organic compounds from the boreal forest floor and understory: a study by solid-phase microextraction and portable gas chromatography-mass spectrometry, Boreal Environment Research, 22, 393-413, 2017.

Bloomer, B. J., Stehr, J. W., Piety, C. A., Salawitch, R. J., and Dickerson, R. R.: Observed relationships of ozone air pollution with temperature and emissions, Geophysical Research Letters, 36, L09803, doi:10.1029/2009GL037308, 2009.

Bourtsoukidis, E., Behrendt, T., Yanez-Serrano, A. M., Hellen, H., Diamantopoulos, E., Catao, E., Ashworth, K., Pozzer, A., Quesada, C. A., Martins, D. L., Sa, M., Araujo, A., Brito, J., Artaxo, P., Kesselmeier, J., Lelieveld, J., and Williams, J.: Strong sesquiterpene emissions from Amazonian soils, Nature Communications, 9, 10.1038/s41467-018-04658-y, 2018.

Buckley, T. N., and Mott, K. A.: Modelling stomatal conductance in response to environmental factors, Plant Cell and Environment, 36, 1691-1699, 10.1111/pce.12140, 2013.

Cao, J., Situ, S., Hao, Y. F., Xie, S. D., and Li, L. Y.: Enhanced summertime ozone and SOA from biogenic volatile organic compound (BVOC) emissions due to vegetation biomass variability during 1981-2018 in China, Atmospheric Chemistry and Physics, 22, 2351-2364, 10.5194/acp-22-2351-2022, 2022.

Cape, J. N., Hamilton, R., and Heal, M. R.: Reactive uptake of ozone at simulated leaf surfaces: Implications for 'non-stomatal' ozone flux, Atmospheric Environment, 43, 1116-1123, 10.1016/j.atmosenv.2008.11.007, 2009.

Carter, L., A. Terando, K. Dow, K. Hiers, K.E. Kunkel, A. Lascurain, D. Marcy, M. Osland, and P. Schramm: Southeast, Impacts, Risks, and Adaptation in the United States: Fourth National Climate Assessment, Volume II, U.S. Global Change Research Program, Washington, D.C., 743-808, 2018.

Clifton, O. E., Fiore, A. M., Munger, J. W., Malyshev, S., Horowitz, L. W., Shevliakova, E., Paulot, F., Murray, L. T., and Griffin, K. L.: Interannual variability in ozone removal by a temperate deciduous forest, Geophysical Research Letters, 44, 542-552, 10.1002/2016gl070923, 2017.

Clifton, O. E., Fiore, A. M., Massman, W. J., Baublitz, C. B., Coyle, M., Emberson, L., Fares, S., Farmer, D. K., Gentine, P., Gerosa, G., Guenther, A. B., Helmig, D., Lombardozzi, D. L., Munger, J. W., Patton, E. G., Pusede, S. E., Schwede, D. B., Silva, S. J., Sörgel, M., Steiner, A. L., and Tai, A. P. K.: Dry Deposition of Ozone over Land: Processes, Measurement, and Modeling, Reviews of Geophysics, 58, 10.1029/2019RG000670, 2020.

Coyle, M., Nemitz, E., Storeton-West, R., Fowler, D., and Cape, J. N.: Measurements of ozone deposition to a potato canopy, Agricultural and Forest Meteorology, 149, 655-666, 10.1016/j.agrformet.2008.10.020, 2009.

Emberson, L. D., Kitwiroon, N., Beevers, S., Buker, P., and Cinderby, S.: Scorched Earth: how will changes in the strength of the vegetation sink to ozone deposition affect human health and ecosystems?, Atmospheric Chemistry and Physics, 13, 6741-6755, https://doi.org/10.5194/acp-13-6741-2013, 2013.

Fares, S., McKay, M., Holzinger, R., and Goldstein, A. H.: Ozone fluxes in a Pinus ponderosa ecosystem are dominated by non-stomatal processes: Evidence from long-term continuous measurements, Agricultural and Forest Meteorology, 150, 420-431, 10.1016/j.agrformet.2010.01.007, 2010.

Fares, S., Weber, R., Park, J. H., Gentner, D., Karlik, J., and Goldstein, A. H.: Ozone deposition to an orange orchard: Partitioning between stomatal and non-stomatal sinks, Environ Pollut, 169, 258-266, 10.1016/j.envpol.2012.01.030, 2012.

Fares, S., Vargas, R., Detto, M., Goldstein, A. H., Karlik, J., Paoletti, E., and Vitale, M.: Tropospheric ozone reduces carbon assimilation in trees: estimates from analysis of continuous flux measurements, Global Change Biology, 19, 2427-2443, 10.1111/gcb.12222, 2013.

Fares, S., Savi, F., Muller, J., Matteucci, G., and Paoletti, E.: Simultaneous measurements of above and below canopy ozone fluxes help partitioning ozone deposition between its various sinks in a Mediterranean Oak Forest, Agricultural and Forest Meteorology, 198-199, 181-191, 10.1016/j.agrformet.2014.08.014, 2014.

Feng, Z. Z., Yuan, X. Y., Fares, S., Loreto, F., Li, P., Hoshika, Y., and Paoletti, E.: Isoprene is more affected by climate drivers than monoterpenes: A meta-analytic review on plant isoprenoid emissions, Plant Cell and Environment, 42, 1939-1949, 10.1111/pce.13535, 2019.

Ficklin, D. L., and Novick, K. A.: Historic and projected changes in vapor pressure deficit suggest a continental-scale drying of the United States atmosphere, Journal of Geophysical Research-Atmospheres, 122, 2061-2079, 10.1002/2016jd025855, 2017.

Finkelstein, P. L., Ellestad, T. G., Clarke, J. F., Meyers, T. P., Schwede, D. B., Hebert, E. O., and Neal, J. A.: Ozone and sulfur dioxide dry deposition to forests: Observations and model evaluation, Journal of Geophysical Research-Atmospheres, 105, 15365-15377, 10.1029/2000jd900185, 2000.

Fowler, D., Flechard, C., Cape, J. N., Storeton-West, R., and Coyle, M.: Measurements of ozone deposition to vegetation quantifying the flux, the stomatal and non-stomatal components, Water, Air and Soil Pollution, 130, 63-74, 2001.

Fowler, D., Pilegaard, K., Sutton, M. A., Ambus, P., Raivonen, M., Duyzer, J., Simpson, D., Fagerli, H., Fuzzi, S., Schjoerring, J. K., Granier, C., Neftel, A., Isaksen, I. S. A., Laj, P., Maione, M., Monks, P. S., Burkhardt, J., Daemmgen, U., Neirynck, J., Personne, E., Wichink-Kruit, R., Butterbach-Bahl, K., Flechard, C., Tuovinen, J. P., Coyle, M., Gerosa, G., Loubet, B., Altimir, N., Gruenhage, L., Ammann, C., Cieslik, S., Paoletti, E., Mikkelsen, T. N., Ro-Poulsen, H., Cellier, P., Cape, J. N., Horváth, L., Loreto, F., Niinemets, Ü., Palmer, P. I., Rinne, J., Misztal, P., Nemitz, E., Nilsson, D., Pryor, S., Gallagher, M. W., Vesala, T., Skiba, U., Brüggemann, N., Zechmeister-Boltenstern, S., Williams, J., O'Dowd, C., Facchini, M. C., de Leeuw, G., Flossman, A., Chaumerliac, N., and Erisman, J. W.: Atmospheric composition change: Ecosystems–Atmosphere interactions, Atmospheric Environment, 43, 5193-5267, 10.1016/j.atmosenv.2009.07.068, 2009.

Garland, J. A., and Derwent, R. G.: Destruction at the ground and the diurnal cycle of concentration of ozone and other gases, Quarterly Journal of the Royal Meteorological Society, 105, 169-183, 10.1002/qj.49710544311, 1979.

Gerosa, G., Vitale, M., Finco, A., Manes, F., Denti, A. B., and Cieslik, S.: Ozone uptake by an evergreen Mediterranean Forest (*Quercus ilex*) in Italy. Part I: Micrometeorological flux measurements and flux partitioning, Atmospheric Environment, 39, 3255-3266, 10.1016/j.atmosenv.2005.01.056, 2005.

Goldstein, A. H., McKay, M., Kurpius, M. R., Schade, W., Lee, A., Holzinger, R., and Rasmussen, R. A.: Forest thinning experiment confirms ozone deposition to forest

canopy is dominated by reaction with biogenic VOCs, Geophysical Research Letters, 31, L22106, 10.1029/2004GL021259, 2004.

Gong, C., Liao, H., Yue, X., Ma, Y., Lei, Y: Impacts of ozonevegetation interactions on ozone pollution episodes in North China and the Yangtze River Delta, Geophysical Research Letters, 48, e2021GL093814, https://doi.org/10.1029/2021GL093814, 2021.

Gray, C. M., Monson, R. K., and Fierer, N.: Biotic and abiotic controls on biogenic volatile organic compound fluxes from a subalpine forest floor, Journal of Geophysical Research-Biogeosciences, 119, 547-556, 10.1002/2013jg002575, 2014.

Griffin, R. J., Cocker, D. R., Seinfeld, J. H., and Dabdub, D.: Estimate of global atmospheric organic aerosol from oxidation of biogenic hydrocarbons, Geophysical Research Letters, 26, 2721-2724, 10.1029/1999gl900476, 1999.

Grossiord, C., Buckley, T. N., Cernusak, L. A., Novick, K. A., Poulter, B., Siegwolf, R. T. W., Sperry, J. S., and McDowell, N. G.: Plant responses to rising vapor pressure deficit, New Phytologist, 226, 1550-1566, 2020.

Hardacre, C., Wild, O., and Emberson, L.: An evaluation of ozone dry deposition in global scale chemistry climate models, Atmospheric Chemistry and Physics, 15, 6419-6436, 10.5194/acp-15-6419-2015, 2015.

Hayhoe, K., Wuebbles, D. J., Easterling, D. R., Fahey, D. W., Doherty, S., Kossin, J., Sweet, W., Vose, R., and Wehner, M.: Our Changing Climate, Impacts, Risks, and Adaptation in the United States: Fourth National Climate Assessment, Volume II, U.S. Global Change Research Program, Washington, D.C., 72-144, 2018.

Hicks, B. B., Baldocchi, D. D., Meyers, T. P., Hosker Jr., R. P., and Matt, D. R.: A preliminary multiple resistance routine for deriving dry deposition velocities from measured quantities, Water, Air, and Soil Pollution, 36, 311-330, 1987.

Hogg, A., Uddling, J., Ellsworth, D., Carroll, M. A., Pressley, S., Lamb, B., and Vogel, C.: Stomatal and non-stomatal fluxes of ozone to a northern mixed hardwood forest, Tellus B: Chemical and Physical Meteorology, 59, 514-525, 10.1111/j.1600-0889.2007.00269.x, 2007.

Holzinger, R., Lee, A., Paw, K. T., and Goldstein, A. H.: Observations of oxidation products above a forest imply biogenic emissions of very reactive compounds, Atmospheric Chemistry and Physics, 5, 67-75, https://doi.org/10.5194/acp-5-67-2005, 2005.

Homyak, P. M., and Sickman, J. O.: Influence of soil moisture on the seasonality of nitric oxide emissions from chaparral soils, Sierra Nevada, California, USA, Journal of Arid Environments, 103, 46-52, 10.1016/j.jaridenv.2013.12.008, 2014.

Huang, L., McDonald-Buller, E. C., McGaughey, G., Kimura, Y., and Allen, D. T.: The impact of drought on ozone dry deposition over eastern Texas, Atmospheric Environment, 127, 176-186, http://dx.doi.org/10.1016/j.atmosenv.2015.12.022, 2016.

Jarvis, P. G.: Interpretation of variation in leaf water potential and stomatal conductance found in canopies in field, Philosophical Transactions of the Royal Society of London Series B-Biological Sciences, 273, 593-610, 10.1098/rstb.1976.0035, 1976.

Jerrett, M., Burnett, R. T., Pope III, C. A., Ito, K., Thurston, G., Krewski, D., Shi, Y., Calle, E., and Thun, M.: Long-Term Ozone Exposure and Mortality, The New England Journal of Medicine, 360, 1085-1095, 2009.

Kavassalis, S. C., and Murphy, J. G.: Understanding ozone-meteorology correlations: A role for dry deposition, Geophysical Research Letters, 44, 2922-2931, 10.1002/2016gl071791, 2017.

Kristensen, K., Cui, T., Zhang, H., Gold, A., Glasius, M., and Surratt, J. D.: Dimers in alpha-pinene secondary organic aerosol: effect of hydroxyl radical, ozone, relative humidity and aerosol acidity, Atmospheric Chemistry and Physics, 14, 4201-4218, 10.5194/acp-14-4201-2014, 2014.

Kulmala, M., Suni, T., Lehtinen, K. E. J., Dal Maso, M., Boy, M., Reissell, A., Rannik, U., Aalto, P., Keronen, P., Hakola, H., Back, J. B., Hoffmann, T., Vesala, T., and Hari, P.: A new feedback mechanism linking forests, aerosols, and climate, Atmospheric Chemistry and Physics, 4, 557-562, 10.5194/acp-4-557-2004, 2004.

Kurpius, M. R., and Goldstein, A. H.: Gas-phase chemistry dominates O_3 loss to a forest, implying a source of aerosols and hydroxyl radicals to the atmosphere, Geophysical Research Letters, 30, 10.1029/2002gl016785, 2003.

Lamaud, E., Carrara, A., Brunet, Y., Lopez, A., and Druilhet, A.: Ozone fluxes above and within a pine forest canopy in dry and wet conditions, Atmospheric Environment, 36, 77-88, 2002.

Lin, M., Malyshev, S., Shevliakova, E., Paulot, F., Horowitz, L. W., Fares, S., Mikkelsen, T. N., and Zhang, L.: Sensitivity of ozone dry deposition to ecosystem-atmosphere interactions: A critical appraisal of observations and simulations, Global Biogeochemical Cycles, 33, 1264-1288, https://doi.org/10.1029/2018GB006157, 2019.

Lin, M., Horowitz, L. W., Xie, Y., Paulot, F., Malyshev, S., Shevliakova, E., Finco, A., Gerosa, G., Kubistin, D., and Pilegaard, K.: Vegetation feedbacks during drought exacerbate ozone air pollution extremes in Europe, Nature Climate Change, 10, 444-451, https://doi.org/10.1038/s41558-020-0743-y, 2020.

Liu, Z., Pan, Y. P., Song, T., Hu, B., Wang, L. L., and Wang, Y. S.: Eddy covariance measurements of ozone flux above and below a southern subtropical forest canopy, Sci. Total Environ., 791, 10.1016/j.scitotenv.2021.148338, 2021.

Lombardozzi, D., Sparks, J. P., and Bonan, G.: Integrating O_3 influences on terrestrial processes: photosynthetic and stomatal response data available for regional and global modeling, Biogeosciences, 10, 6815-6831, 10.5194/bg-10-6815-2013, 2013.

Marrs, J. K., Reblin, J. S., Logan, B. A., Allen, D. W., Reinmann, A. B., Bombard, D. M., Tabachnik, D., and Hutyra, L. R.: Solar-Induced Fluorescence Does Not Track Photosynthetic Carbon Assimilation Following Induced Stomatal Closure, Geophysical Research Letters, 47, 10.1029/2020gl087956, 2020.

McGlynn, D. F., Barry, L. E. R., Lerdau, M. T., Pusede, S. E., and Isaacman-VanWertz, G.: Measurement report: Variability in the composition of biogenic volatile organic compounds in a Southeastern US forest and their role in atmospheric reactivity, Atmospheric Chemistry and Physics, 21, 15755-15770, https://doi.org/10.5194/acp-21-15755-2021, 2021.

McGlynn, D. F., Frazier, G., Barry, L. E. R., Lerdau, M. T., Pusede, S. E., and Isaacman-VanWertz, G.: Minor contributions of daytime monoterpenes are major contributors to atmospheric reactivity, Biogeosciences, 20, 45-55, 10.5194/bg-20-45-2023, 2023.

Meyers, T. P., Finkelstein, P., Clarke, J., Ellestad, T. G., and Sims, P. F.: A multilayer model for inferring dry deposition using standard meteorological measurements, Journal of Geophysical Research-Atmospheres, 103, 22645-22661, 10.1029/98jd01564, 1998.

Monks, P. S., Archibald, A. T., Colette, A., Cooper, O., Coyle, M., Derwent, R., Fowler, D., Granier, C., Law, K. S., Mills, G. E., Stevenson, D. S., Tarasova, O., Thouret, V., von Schneidemesser, E., Sommariva, R., Wild, O., and Williams, M. L.: Tropospheric ozone and its precursors from the urban to the global scale from air quality to short-lived climate forcer, Atmospheric Chemistry and Physics, 15, 8889-8973, 10.5194/acp-15-8889-2015, 2015.

Monteith, J. L., and Unsworth, M. H.: Principles of Environmental Physics, Edward Arnold, London, 1990.

Mott, K. A., and Parkhurst, D. F.: Stomatal responses to humidity in air and helox, Plant, Cell and Environment, 14, 509-515, https://doi.org/10.1111/j.1365-3040.1991.tb01521.x, 1991.

Nolte, C. G., Dolwick, P. D., Fann, N., Horowitz, L. W., Naik, V., Pinder, R. W., Spero, T. L., Winner, D. A., and Zisk, L. H.: Air Quality, Impacts, Risks, and Adaptation in the United States: Fourth National Climate Assessment, Volume II, U.S. Global Change Research Program, Washington, D.C., 512-538, 2018.

Penuelas, J., and Staudt, M.: BVOCs and global change, Trends in Plant Science, 15, 133-144, 10.1016/j.tplants.2009.12.005, 2010.

Pilegaard, K.: Processes regulating nitric oxide emissions from soils, Philosophical Transactions of the Royal Society B-Biological Sciences, 368, 10.1098/rstb.2013.0126, 2013.

Pleim, J. E., Xiu, A. J., Finkelstein, P. L., Clarke, J. F., and Ams: Evaluation of a coupled land-surface and dry deposition model through comparison to field measurements of surface heat, moisture, and ozone fluxes, 12th Symposium on Boundary Layers and Turbulence, Vancouver, Canada, 1997, WOS:000075999700242, 478-479, 1997.

Porcar-Castell, A., Tyystjarvi, E., Atherton, J., van der Tol, C., Flexas, J., Pfundel, E. E., Moreno, J., Frankenberg, C., and Berry, J. A.: Linking chlorophyll a fluorescence to photosynthesis for remote sensing applications: mechanisms and challenges, J Exp Bot, 65, 4065-4095, 10.1093/jxb/eru191, 2014.

Pusede, S. E., Steiner, A. L., and Cohen, R. C.: Temperature and recent trends in the chemistry of continental surface ozone, Chem Rev, 115, 3898-3918, 10.1021/cr5006815, 2015.

Rannik, U., N. Altimir, N., Mammarella, I., Bäck, J., Rinne, J., Ruuskanen, T. M., Hari, P., Vesala, T., and Kulmala, M.: Ozone deposition into a boreal forest over a decade of observations: evaluating deposition partitioning and driving variables, Atmospheric Chemistry and Physics, 12, 12165-12182, 10.5194/acp-12-12165-2012, 2012.

Reich, P. B.: Quantifying plant response to ozone: a unifying theory, Tree Physiol, 3, 63-91, 10.1093/treephys/3.1.63, 1987.

Sadiq, M., Tai, A. P. K., Lombardozzi, D., and Val Martin, M.: Effects of ozone–vegetation coupling on surface ozone air quality via biogeochemical and meteorological feedbacks, Atmospheric Chemistry and Physics, 17, 3055-3066, 10.5194/acp-17-3055-2017, 2017.

Sitch, S., Cox, P. M., Collins, W. J., and Huntingford, C.: Indirect radiative forcing of climate change through ozone effects on the land-carbon sink, Nature, 448, 791-U794, 10.1038/nature06059, 2007.

Szopa, S., V. Naik, B. Adhikary, P. Artaxo, T. Berntsen, W.D. Collins, S. Fuzzi, L. Gallardo, A. Kiendler-Scharr, Z. Klimont, H. Liao, N. Unger, and P. Zanis: Short-Lived Climate Forcers in Climate Change 2021: The Physical Science Basis. Contribution of Working Group I to the Sixth Assessment Report of the Intergovernmental Panel on Climate Change, Intergovernmental Panel on Climate Change, Cambridge, United Kingdom and New York, NY, USA, 817–922, 2021.

Tatham, E. A.: Controls on Light Inhibition of Leaf Respiration and Water Use Efficiency in a Temperate Broadleaf Deciduous Forest, Master of Science, Environmental Sciences, University of Virginia, Charlottesville, VA, 62 pp., 2021.

Tuovinen, J. P., Emberson, L., and Simpson, D.: Modelling ozone fluxes to forests for risk assessment: status and prospects, Annals of Forest Science, 66, 10.1051/forest/2009024, 2009.

Turnipseed, A. A., Burns, S. P., Moore, D. J. P., Hu, J., Guenther, A. B., and Monson, R. K.: Controls over ozone deposition to a high elevation subalpine forest, Agricultural and Forest Meteorology, 149, 1447-1459, 10.1016/j.agrformet.2009.04.001, 2009.

Urban, J., Ingwers, M., McGuire, M. A., and Teskey, R. O.: Stomatal conductance increases with rising temperature, Plant Signal Behav, 12, e1356534, 10.1080/15592324.2017.1356534, 2017.

Vermeuel, M. P., Cleary, P. A., Desai, A. R., and Bertram, T. H.: Simultaneous Measurements of O_3 and HCOOH Vertical Fluxes Indicate Rapid In-Canopy Terpene Chemistry Enhances O_3 Removal Over Mixed Temperate Forests, Geophysical Research Letters, 48, 2020GL090996, 10.1029/2020GL090996, 2021.

Way, D. A., and Oren, R.: Differential responses to changes in growth temperature between trees from different functional groups and biomes: a review and synthesis of data, Tree Physiology, 30, 669-688, 10.1093/treephys/tpq015, 2010.

Wesely, M. L., and Hicks, B. B.: Some Factors that Affect the Deposition Rates of Sulfur Dioxide and Similar Gases on Vegetation, Journal of the Air Pollution Control Association, 27, 1110-1116, 10.1080/00022470.1977.10470534, 1977.

Wesely, M. L.: Parameterization of surfance resistances to gaseous dry deposition in regional-scale numerical models, Atmospheric Environment, 23, 1293-1304, 1989.

Wittig, V. E., Ainsworth, E. A., and Long, S. P.: To what extent do current and projected increases in surface ozone affect photosynthesis and stomatal conductance of trees? A meta-analytic review of the last 3 decades of experiments, Plant Cell Environ, 30, 1150-1162, 10.1111/j.1365-3040.2007.01717.x, 2007.

Wittig, V. E., Ainsworth, E. A., Naidu, S. L., Karnosky, D. F., and Long, S. P.: Quantifying the impact of current and future tropospheric ozone on tree biomass, growth, physiology and biochemistry: a quantitative meta-analysis, Global Change Biology, 15, 396-424, 10.1111/j.1365-2486.2008.01774.x, 2009.

Wolfe, G. M., and Thornton, J. A.: The Chemistry of Atmosphere-Forest Exchange (CAFE) Model – Part 1: Model description and characterization, Atmospheric Chemistry and Physics, 11, 77-101, 10.5194/acp-11-77-2011, 2011.

Wolfe, G. M., Thornton, J. A., McKay, M., and Goldstein, A. H.: Forest-atmosphere exchange of ozone: sensitivity to very reactive biogenic VOC emissions and implications for in-canopy photochemistry, Atmospheric Chemistry and Physics, 11, 7875-7891, 10.5194/acp-11-7875-2011, 2011.

Wong, A. Y. H., Geddes, J. A., Ducker, J. A., Holmes, C. D., Fares, S., Goldstein, A. H., Mammarella, I., and Munger, J. W.: New Evidence for the Importance of Non-Stomatal Pathways in Ozone Deposition During Extreme Heat and Dry Anomalies, Geophysical Research Letters, 49, 10.1029/2021gl095717, 2022.

Wu, Y. H., Brashers, B., Finkelstein, P. L., and Pleim, J. E.: A multilayer biochemical dry deposition model - 2. Model evaluation, Journal of Geophysical Research-Atmospheres, 108, 10.1029/2002jd002306, 2003.

Yang, X., Tang, J., Mustard, J. F., Lee, J.-E., Rossini, M., Joiner, J., Munger, J. W., Kornfeld, A., and Richardson, A. D.: Solar-induced chlorophyll fluorescence that correlates with canopy photosynthesis on diurnal and seasonal scales in a temperate deciduous forest, Geophysical Research Letters, 42, 2977-2987, 10.1002/2015gl063201, 2015.

Yang, X., Shi, H., Stovall, A., Guan, K., Miao, G., Zhang, Y., Zhang, Y., Xiao, X., Ryu, Y., and Lee, J.-E.: FluoSpec 2—An Automated Field Spectroscopy System to Monitor Canopy Solar-Induced Fluorescence, Sensors, 18, 2063, https://doi.org/10.3390/s18072063, 2018.

Zapletal, M., Pretel, J., Chroust, P., Cudlin, P., Edwards-Jonasova, M., Urban, O., Pokorny, R., Czerny, R., and Hunova, I.: The influence of climate change on stomatal ozone flux to a mountain Norway spruce forest, Environmental Pollution, 169, 267-273, 10.1016/j.envpol.2012.05.008, 2012.

Zhang, L., Brook, J. R., and Vet, R.: On ozone dry deposition—with emphasis on non-stomatal uptake and wet canopies, Atmosperic Environment, 36, 4787-4799, https://doi.org/10.1016/S1352-2310(02)00567-8, 2002.

Zhang, L., Brook, J. R., and Vet, R.: A revised parameterization for gaseous dry deposition in air-quality models, Atmospheric Chemistry and Physics, 3, 2067-2082, 2003.

CHAPTER 5: SUMMARY

This dissertation contributes knowledge regarding how O_3, via O_3 production (PO_3) and O_3 loss (LO_3) will respond to climate change-driven warming temperatures. With respect to PO_3, I highlight the need for continued emissions reductions, particularly in polluted cities and with respect to LO_3, I highlight the need for multi-year eddy-covariance O_3 flux measurements. Climate change has, is, and will alter the ways in which O_3 varies with temperature. Depending on the strength of precursor emissions reductions, by the end of the 21st century, O_3 could increase up to 9 ppb in the eastern U.S. (Fiore et al., 2015). The O_3 season is predicted to lengthen and wintertime O_3 is predicted to increase; however, if warming is slowed, precursor emissions reductions may outpace temperature increases and could decrease summertime O_3 (Fiore et al., 2015; Nolte et al., 2008; Racherla and Adams, 2008). Predictions of outcomes due to climate change-driven O_3 increases include adverse human health impacts (Bell et al., 2007) and up to a 10% decrease in global crop yield, threating food security (Tai et al., 2014). In this dissertation, I discussed how both PO_3 and LO_3 may scale with rising temperatures.

In Chapter 2, I assessed how O_3 climate penalties ($m_{O3\text{-}T}$) changed with reduced precursor emissions reductions from 1999–2019 and their NO_2 dependence across the contiguous U.S. The Northeast, Southeast, and Ohio Valley underwent the largest reductions in $m_{O3\text{-}T}$ (≥1 ppb $^{o}C^{-1}$), followed by the South, Upper Midwest, and West. U.S.-wide reductions in NO_x decreased the O_3-temperature correlation. I demonstrate that temperature-dependent PO_3 controls $m_{O3\text{-}T}$ and the maximum daily average 8-h (MDA8) O_3 in seven of the nine NOAA climate regions. In these regions, $m_{O3\text{-}T}$ and MDA8 O_3 vary with NO_2 following predictions from an analytical chemical model. This work demonstrates the success of precursor emissions reductions for O_3 air pollution

and climate adaptation independently based on the difference in NO_x regime turnover point for $m_{O3\text{-}T}$ and MDA8 O_3. Thus, NO_x emissions reductions are a climate adaptation strategy for improving O_3 air quality. Several regions and metropolitan statistical areas (MSAs) (e.g., the West and Los Angeles) still exhibit NO_x-suppressed chemistry.

The work in Chapter 2 provides an example of where regional trends can mask urban ones, as not all metropolitan statistical areas (MSAs) follow regional patterns. With recent improvements to satellite spatial resolution, understanding local NO_2 distributions is feasible without a dense surface monitoring network. Particularly in MSAs with extensive O_3 monitoring networks, combined, these two datasets demonstrate local chemical production regimes, necessary for identifying effective pollutant mitigation strategies and predicting responses to emissions reductions. This work is most policy-relevant at the local level.

Presently, per Clean Air Act requirements, many U.S. O_3 monitoring sites only operate during the O_3 season (May–September or April–October). As the O_3 season gets longer (e.g., Racherla and Adams, 2008), a year-round operation of these sites would add valuable data in tandem with the continuation of long-term measurements. An assessment of long-term seasonal trends in $m_{O3\text{-}T}$ will aid in monitoring the O_3 response to a changing climate. As temperatures rise, $m_{O3\text{-}T}$ will need to be assessed earlier in the spring and later into the fall.

In Chapters 3 and 4, I measured O_3 loss (LO_3) via dry deposition to a Central Virginia forest and described the temperature dependence of O_3 mixing ratios and O_3 v_d. I used a wet chemiluminescence-based analyzer measuring O_3 (10 s^{-1}) and a 3D sonic anemometer to measure vertical wind velocities (10 s^{-1}) to calculate the O_3 flux and O_3 deposition velocity (v_d) using the eddy covariance technique at 40-m on a research tower. I used a slower (2–60 s) UV absorption-

based O_3 analyzer to measure the O_3 mixing ratio at five heights within and above the forest canopy. While minimally dependent on temperature, O_3 mixing ratios strongly depended on vapor pressure deficit, indicating LO_3 controls daily O_3 variability. Stomatal O_3 uptake drove daytime O_3 v_d and reactions with monoterpenes within the forest canopy drove nighttime O_3 v_d. Reduced stomatal aperture on days with a mean daytime temperature ≥32ºC decreased daytime mean O_3 v_d by 49%, increasing mean O_3 mixing ratio by 19%. Yet, when mean daytime temperature ≥32ºC and the preceding nighttime mean temperature was ≥24ºC, the increase in O_3-BVOC reactions lowered O_3 mixing ratios overnight such that they offset the increase in O_3 during the day. While I observe that stomatal O_3 uptake controls O_3 v_d during the day, thus the majority of deposition at this site, significant variability in nonstomatal uptake has been shown to control O_3 v_d interannual variability (Clifton et al., 2017; Rannik et al., 2012). A long-term dataset is needed for the analysis of interannual variability at the Virginia Forest Laboratory.

In the O_3 deposition community, there is a need, and frequent calls, for measurements of O_3 deposition in new locations and long-term monitoring (Clifton et al., 2020). In a review of O_3 dry deposition, Clifton et al. (2020) reports only 11 sites globally measured O_3 v_d for >5 years. While the preferred method, instruments capable of satisfying analytical requirements of eddy covariance are not commercially available off-the-shelf and require significant time and personnel investments to maintain and operate. The most beneficial outcome of this work will be the continued operation of this site for years to come. O_3 uptake reduces carbon assimilation (e.g., Fares et al., 2013), can have cascading effects on biogeochemical cycles (Sadiq et al., 2017), and can indirectly increase radiative forcing (Sitch et al., 2007). By maintaining the current site, collocated with CO_2 and water fluxes and solar-induced fluorescence (SIF), a proxy for photosynthesis, future analyses may include how and on what timescale O_3 v_d varies with

photosynthesis, interannual variability in total, stomatal, and nonstomatal O_3 v_d, and how O_3 v_d changes with heatwaves and droughts. Measurements of NO_x and NO_y fluxes, soon to be added at the site, will aide in further understanding O_3 and O_3 v_d. Frequently, O_3 v_d studies employ short (weeks to months long) field campaigns. While this literature provides valuable research, a lengthening O_3 season requires multi-season measurements. Long-term, year-round measurements of O_3 and O_3 deposition will provide insight into if and how the O_3 seasoning is lengthening and plant response to increased uptake.

Finally, I echo previous calls for more O_3 deposition measurements in new locations and for longer periods. The fraction of deposition that occurs via the stomatal versus the nonstomatal pathway is highly variable from site to site. To accurately model how O_3 dry deposition and O_3 mixing ratios will respond to climate change, the deposition pathway, and thus driving variables, need to be better represented in models. Not only is correctly depicting O_3 loss important to improving O_3 modeling, the myriad of ways in which O_3 detrimentally affects the environment demonstrates how reducing precursor emissions, thus reducing PO_3, will not only benefit human health, but limit plant-O_3 uptake.

References

Bell, M. L., Goldberg, R., Hogrefe, C., Kinney, P. L., Knowlton, K., Lynn, B., Rosenthal, J., Rosenzweig, C., and Patz, J. A.: Climate change, ambient ozone, and health in 50 US cities, Climatic Change, 82, 61-76, 10.1007/s10584-006-9166-7, 2007.

Clifton, O. E., Fiore, A. M., Munger, J. W., Malyshev, S., Horowitz, L. W., Shevliakova, E., Paulot, F., Murray, L. T., and Griffin, K. L.: Interannual variability in ozone removal by a temperate deciduous forest, Geophysical Research Letters, 44, 542-552, 10.1002/2016gl070923, 2017.

Clifton, O. E., Fiore, A. M., Massman, W. J., Baublitz, C. B., Coyle, M., Emberson, L., Fares, S., Farmer, D. K., Gentine, P., Gerosa, G., Guenther, A. B., Helmig, D., Lombardozzi, D. L., Munger, J. W., Patton, E. G., Pusede, S. E., Schwede, D. B., Silva, S. J., Sörgel, M., Steiner, A. L., and Tai, A. P. K.: Dry Deposition of Ozone over Land: Processes, Measurement, and Modeling, Reviews of Geophysics, 58, 10.1029/2019RG000670, 2020.

Fares, S., Vargas, R., Detto, M., Goldstein, A. H., Karlik, J., Paoletti, E., and Vitale, M.: Tropospheric ozone reduces carbon assimilation in trees: estimates from analysis of continuous flux measurements, Global Change Biology, 19, 2427-2443, 10.1111/gcb.12222, 2013.

Fiore, A. M., Naik, V., and Leibensperger, E. M.: Air Quality and Climate Connections, Journal of the Air & Waste Management Association, 65, 645-685, 10.1080/10962247.2015.1040526, 2015.

Nolte, C. G., Gilliland, A. B., Hogrefe, C., and Mickley, L. J.: Linking global to regional models to assess future climate impacts on surface ozone levels in the United States, Journal of Geophysical Research-Atmospheres, 113, 10.1029/2007jd008497, 2008.

Racherla, P. N., and Adams, P. J.: The response of surface ozone to climate change over the Eastern United States, Atmospheric Chemistry and Physics, 8, 871-885, 2008.

Rannik, U., N. Altimir, N., Mammarella, I., Bäck, J., Rinne, J., Ruuskanen, T. M., Hari, P., Vesala, T., and Kulmala, M.: Ozone deposition into a boreal forest over a decade of observations: evaluating deposition partitioning and driving variables, Atmospheric Chemistry and Physics, 12, 12165-12182, 10.5194/acp-12-12165-2012, 2012.

Sadiq, M., Tai, A. P. K., Lombardozzi, D., and Val Martin, M.: Effects of ozone–vegetation coupling on surface ozone air quality via biogeochemical and meteorological feedbacks, Atmospheric Chemistry and Physics, 17, 3055-3066, 10.5194/acp-17-3055-2017, 2017.

Sitch, S., Cox, P. M., Collins, W. J., and Huntingford, C.: Indirect radiative forcing of climate change through ozone effects on the land-carbon sink, Nature, 448, 791-794, 10.1038/nature06059, 2007.

Tai, A. P. K., Martin, M. V., and Heald, C. L.: Threat to future global food security from climate change and ozone air pollution, Nature Climate Change, 4, 817-821, 10.1038/nclimate2317, 2014.